Springer Theses
Recognizing Outstanding Ph.D. Research

Darshana Chandrakant Patel

A Study of the Isoscalar Giant Monopole Resonance

The Role of Symmetry Energy in Nuclear Incompressibility in the Open-Shell Nuclei

Springer

Springer Theses

Recognizing Outstanding Ph.D. Research

More information about this series at http://www.springer.com/series/8790

Aims and Scope

The series "Springer Theses" brings together a selection of the very best Ph.D. theses from around the world and across the physical sciences. Nominated and endorsed by two recognized specialists, each published volume has been selected for its scientific excellence and the high impact of its contents for the pertinent field of research. For greater accessibility to non-specialists, the published versions include an extended introduction, as well as a foreword by the student's supervisor explaining the special relevance of the work for the field. As a whole, the series will provide a valuable resource both for newcomers to the research fields described, and for other scientists seeking detailed background information on special questions. Finally, it provides an accredited documentation of the valuable contributions made by today's younger generation of scientists.

Theses are accepted into the series by invited nomination only and must fulfill all of the following criteria

- They must be written in good English.
- The topic should fall within the confines of Chemistry, Physics, Earth Sciences, Engineering and related interdisciplinary fields such as Materials, Nanoscience, Chemical Engineering, Complex Systems and Biophysics.
- The work reported in the thesis must represent a significant scientific advance.
- If the thesis includes previously published material, permission to reproduce this must be gained from the respective copyright holder.
- They must have been examined and passed during the 12 months prior to nomination.
- Each thesis should include a foreword by the supervisor outlining the significance of its content.
- The theses should have a clearly defined structure including an introduction accessible to scientists not expert in that particular field.

Darshana Chandrakant Patel

A Study of the Isoscalar Giant Monopole Resonance

The Role of Symmetry Energy in Nuclear Incompressibility in the Open-Shell Nuclei

Springer

Darshana Chandrakant Patel
University of Notre Dame
Notre Dame, IN, USA

ISSN 2190-5053 ISSN 2190-5061 (electronic)
Springer Theses
ISBN 978-3-319-22206-6 ISBN 978-3-319-22207-3 (eBook)
DOI 10.1007/978-3-319-22207-3

Library of Congress Control Number: 2015959353

Springer Cham Heidelberg New York Dordrecht London

Printed on acid-free paper

Springer International Publishing AG Switzerland is part of Springer Science+Business Media (www.springer.com)

Abstract
by
Darshana Chandrakant Patel

The objective of this thesis work is to investigate the "softness" in nuclear incompressibility observed in the open-shell nuclei and the role of symmetry energy in the nuclear incompressibility. The first experiment was performed to study the isoscalar giant monopole resonance (ISGMR) strength distribution in the Cd isotopes. Accurate and extremely forward angle (including 0°) alpha inelastic scattering measurements were made on a series of $^{106,110-116}$Cd isotopes. The "softness" in the nuclear incompressibility, as observed in the Sn isotopes, was seen in the Cd isotopes as well. The relativistic and nonrelativistic calculations, which successfully reproduce the ISGMR strength distributions in ^{208}Pb and ^{90}Zr, overestimate the ISGMR centroid energies in the Sn and the Cd isotopes. Inclusion of the various types of pairing effects in the calculation cannot account for the observed discrepancy. The second experiment was performed to test an intriguing idea of mutually enhanced magicity (MEM) effect playing a role in the nuclear incompressibility in order to account for the observed "softness." Systematic and extremely accurate alpha inelastic scattering measurements were made on ^{204,206,208}Pb isotopes. The ISGMR centroid energies measured in the series of Pb isotopes indicated a standard $A^{-1/3}$ dependence in stark contrast to a sharp increase of 0.6 MeV in the ISGMR centroid energy of ^{208}Pb when compared to the centroid energy of ^{204}Pb that was predicted as resulting from MEM effect. These results clearly established that the MEM effect does not play a measurable role in the energy of the ISGMR, thereby leaving the question of experimentally observed "softness" in the Sn and Cd unanswered still.

Paving a path for the future experiments, in order to answer the haunting question of experimentally observed "softness" in nuclear incompressibility, the third experiment was performed to test the feasibility of using deuteron as a probe to measure ISGMR in radioactive isotopes using inverse kinematics. Accurate and extremely forward angle inelastic scattering measurements were made using high-energy (100 MeV/u) deuteron beam. For the first time, the multipole decomposition analysis was successfully employed to delineate different multipole contributions reliably. This experiment established the feasibility of using deuteron probe to study giant resonances in the radioactive nuclei and thus explore the density dependence of symmetry energy in further detail.

To Ila and Chandrakant Patel, my parents
and
To Kalpesh Patel, my brother

Supervisor's Foreword

Giant resonances are highly collective oscillations of the atomic nucleus in which a large fraction of the nucleons (neutrons and protons) of the nucleus move together. Indeed, the motion is so collective that it is appropriate to think of these modes of excitation in hydrodynamic terms as the oscillations of a liquid drop. The collectivity of these modes can be measured via cross sections of their excitation in direct nuclear reactions such as inelastic scattering. The isoscalar giant monopole resonance (ISGMR) is a compression mode of collective oscillation that corresponds to the compression and expansion of the nuclear volume, with concomitant oscillations of the nuclear density, about its equilibrium value and, hence, is termed the "breathing mode." Investigations of ISGMR are very important because the frequency (energy) of this oscillation provides a direct means to experimentally determine the nuclear incompressibility, a quantity of fundamental importance in defining the equation of state (EOS) for nuclear matter. The latter describes a number of interesting phenomena from collective excitations of nuclei to supernova explosions and radii of neutron stars. In particular, for the investigations related to the EOS of very dense nuclear matter, such as that encountered in neutron stars, the asymmetry term of the nuclear incompressibility is expected to play a very important role, making its experimental determination a topic of strong current interest and focus, both experimentally and theoretically. (The "asymmetry" here refers to the difference of the numbers of neutrons (N) and protons (Z) in a system and is defined as ((N−Z)/(N+Z)).)

Experimental identification of the ISGMR requires inelastic scattering of an isoscalar particle (such as the α-particle, the nucleus of the ^{4}He atom) at extremely forward angles, including 0°, where the cross section for exciting the ISGMR is maximal. Such measurements have improved considerably over the years, and it is now possible to obtain inelastic spectra even at 0°, virtually free of all instrumental background. The ISGMR strength distributions can then be extracted from a multipole-decomposition analysis of such "background-free" inelastic-scattering spectra.

In this dissertation, Dr. Darshana Patel has presented results of her investigations on ISGMR related to the asymmetry term of nuclear incompressibility and also explored a very intriguing phenomenon observed a few years ago of the "softness" of open-shell nuclei: measurements on a series of Sn isotopes had revealed that the energies of the ISGMR in these nuclei were significantly lower than what would be expected from the value of nuclear incompressibility determined from the closed-shell nuclei. From her measurements on a series of Cd isotopes, Dr. Patel confirmed the value of the asymmetry term of nuclear incompressibility previously obtained from the Sn measurements and that the Cd isotopes also exhibit the "softness" observed in the Sn isotopes. There have been several theoretical attempts to understand and describe this observed "softness," none too successful, and this question remains an open problem in nuclear structure physics.

An intriguing hypothesis forwarded to explain this phenomenon was that this could be the effect of the so-called "mutual enhancement magicity" (MEM) effect first noted for nuclear masses. It turns out that theoretical expressions for nuclear masses always miss out in the cases for nuclei with doubly closed shells, i.e., where both the protons and neutrons fill in shells in a nucleus completely with a wide gap to the next higher shell (akin to noble gases in atoms), pointing to an added stability associated with the closed shells. The suggestion then was that a similar effect might occur in case of nuclear incompressibility and any calculations using nuclear incompressibility derived from the closed-shell nuclei would always overestimate the ISGMR in open-shell nuclei. Dr. Patel set about to test this hypothesis and measured, in the same experiment to minimize any systematic effects in the final results, the ISGMR in three isotopes of Pb with masses 204, 206, and 208. The nucleus ^{208}Pb is the quintessential "doubly closed shell" nucleus, and, indeed, the extraction of nuclear incompressibility from ISGMR relies primarily on this nucleus. On the other hand, the other two nuclei measured in this work, ^{204}Pb and ^{206}Pb, are "open shell," and, per the aforementioned hypothesis, the ISGMR energies in ^{204,206}Pb would have been significantly lower than that in ^{208}Pb. Dr. Patel's careful measurements showed that this was not the case and that the ISGMR energies were nearly identical in the three nuclei, contradicting the MEM-effect hypothesis.

The advent of radioactive ion beams has opened up the prospect of extending ISGMR measurements to nuclei away from the stability line, thus extending the range of isotopes over which to measure this resonance and to extract the asymmetry term in nuclear incompressibility to a higher precision. These measurements have to be performed in "inverse kinematics," with beams of the nuclei of interest impinging on an isoscalar target. For various practical reasons, the α-particle, used successfully in normal kinematics ISGMR measurements, does not render itself to be an ideal system for inverse kinematic measurements, and another isoscalar particle, the deuteron (nucleus of deuterium, an isotope of hydrogen), appears to be a more appropriate choice as the target material instead. However, practically no measurements had been made to demonstrate that it was possible to correctly extract the ISGMR strengths from inelastic deuteron scattering spectra. The third part of Dr. Patel's dissertation reports her measurements of elastic and inelastic

scattering of deuterons off several targets. She was able to extract the ISGMR strength distributions in these nuclei, with results that were fully consistent with those obtained with α-particles, thus clearly establishing the deuteron as an effective probe for such investigations.

Small-angle inelastic scattering measurements are rather difficult to execute, and the analysis of the data requires particular attention to a number of details (not to mention tremendous patience). In her efforts, she was ably supported by the machine staff of the Research Center for Nuclear Physics, Osaka University, Japan, where the experiments were performed, and her many collaborators. The work still remains essentially her own, however, and it is to her credit that she has obtained so many important results in a single dissertation. My expectation is that these results will remain of importance and relevance to researchers in this field for quite some time to come, and I am delighted that her dissertation has been selected for publication in the Springer Theses series.

Notre Dame, France Umesh Garg
September, 2015

Acknowledgments

My thesis work would not have been possible without the guidance, help, and patience of many individuals whom I wish to thank.

First and foremost, I would like to thank, with deepest gratitude, my research adviser, Prof. Umesh Garg, for his unfailing and continuous guidance. I would like to express my great appreciation for his patience through the development of this research work. I shall remain indebted to him for instilling in me an independent researcher's attitude which has proved to be extremely useful for my career as a physicist. I am also very grateful to him for his constant push toward perfection. I would further like to thank him for his extremely useful critiques and editorial comments throughout my publication phase and during the preparation of this thesis.

I would like to thank my committee members Prof. P. Collon, Prof. J. Furdyna, and Prof. G. Mathews for their constant support and interest in my work. I would like to express my appreciation for their time and comments at every annual review meeting. I thank them also for their time and editorial comments toward making this thesis more complete.

I would like to express my special thanks to Prof. M. Harakeh, Prof. M. Itoh, Dr. G.P.A. Berg, and Dr. M. Fujiwara for their significant pieces of advice and help in preparing manuscripts of my publications. I cannot thank them enough for being patient with me through all the discussions and giving in their time despite their extremely busy schedule. I thank them all for giving me personal attention whenever i needed it throughout my research work. I would further like to express my gratitude toward Prof. M. Itoh for helping me with his expertise through the planning and the execution phases of my experiments.

I thank all my collaborators who gave in their time and comments throughout all the experiments. Many thanks to the staff of the Research Center for Nuclear Physics (RCNP), Osaka University, for providing clean and stable beams. I also thank them for their patience and exuberance even during the tough times with the accelerator. Without them, none of this work would have been possible.

I would also like to thank my senior colleagues for all the useful discussions and help that have expanded my knowledge and improved my skills. My special thanks to Dr. M. Couder, Dr. R. deBoer, and Prof. J. Kolata for their advices and

suggestions during my data analysis phase. Amongst my other colleagues, I would like to thank X. Fang, A. Long, F. Luo, D. Ray, K. Smith, M. Varga, and L. Wenting for the useful discussions and fun times together. I would also like to sincerely thank my close friends A. Paul and J. Matta for their readiness in helping me with computational problems.

During my stay at Notre Dame, with the highs and the lows, many individuals have played an important role in making my stay pleasant and comfortable. I thank them all from the bottom of my heart. My special thanks to A. Ayangeakaa, A. Best, J. Matta, and M. Smith for keeping up with my craziness. All the discussions with them have added to my knowledge. I thank them for the quality time we spent together. I would like to thank many other friends of mine who made Notre Dame home away from home. Krishanan, Sunil, Maiya, and Rashi, thank you for being part of my fantastic-five team. I thank them all for being there when I needed them the most. I would also like to extend my thanks to several other friends – Jindal, Utsaw, Punit, Astha, Ramya, Vel, Sachi, Suu, the Chetwanis, the Chandrahases, Seemit, Vaibhav, Shailaja, Sajid, Amit, Chogee, and Ashish – for all the fun social times that I have had.

Above all, many thanks to my dad Chandrakant, my mom Ila, and my brother Kalpesh, to whom I dedicate this thesis work, for they have played a very important role in shaping my life. I would also like to express my heartfelt gratitude to my dear husband Nisarg and his family for their unfailing support, confidence, patience, and love. Words cannot express how much I owe Nisarg for holding up with me through my difficult days while I stayed miles away from him. Most importantly, I thank the Almighty for giving me the strength and vision to complete this research work.

This work has been supported in part by the National Science Foundation (Grant Nos. PHY07-58100, PHY-1068192, and PHY-0822648) and by the Department of Energy under contract no. DE -FD05-92ER40750.

Contents

List of Figures

List of Tables

Chapter 1
Introduction

Our understanding of the ground state and excited state properties of the atomic nuclei remains unsatisfactory even decades after establishing the existence of the nuclear force. The evolution of shell structure in heavy nuclei, the phases of strongly interacting nuclear matter, the nature of exotic excitations in nuclei at the frontier of stability and its role in stellar processes, the nature of neutron stars and dense nuclear matter, the origin of elements in the universe, the exact nature of nuclear reactions and the stellar environments leading to explosions are few of the many phenomena which still have not been understood completely and satisfactorily. A lot of theoretical effort has been made over the past many years to explain the experimental observations and, at the same time, consistent effort has been put forward to push the experimental frontiers. The field has advanced in the last few decades, not the least because of the advent of better computational resources and state of the art experimental facilities worldwide.

On the theoretical front, computationally intensive ab-initio methods using the bare nucleon-nucleon (NN) interaction, and advanced methods like Green's Function Monte Carlo (GFMC) have been used with great success in light nuclei, typically with A $\lesssim$15. Things get more complex in the heavier systems. One way out is to deal with these systems in a nuclear matter framework [8]. The study of nuclear matter is a powerful tool from the point of view of improving our understanding of the nuclear many-body problem. Nuclear matter is a theoretical construct of an infinite number of nucleons with a fixed neutron to proton ratio. The nuclear matter equation of state (EOS) essentially describes the binding energy per nucleon as a function of nuclear density, as shown in Fig. 1.1. The EOS is essentially a constitutive equation which provides a mathematical relationship between two or more state functions associated with a given system, such as its temperature, pressure, internal energy, density or particle number. The nuclear matter EOS is important for understanding many interesting phenomena such as the collective behavior of nucleons in nuclei, the massive stellar collapse leading to a supernova

D.C. Patel, *A Study of the Isoscalar Giant Monopole Resonance*, Springer Theses,
DOI 10.1007/978-3-319-22207-3_1

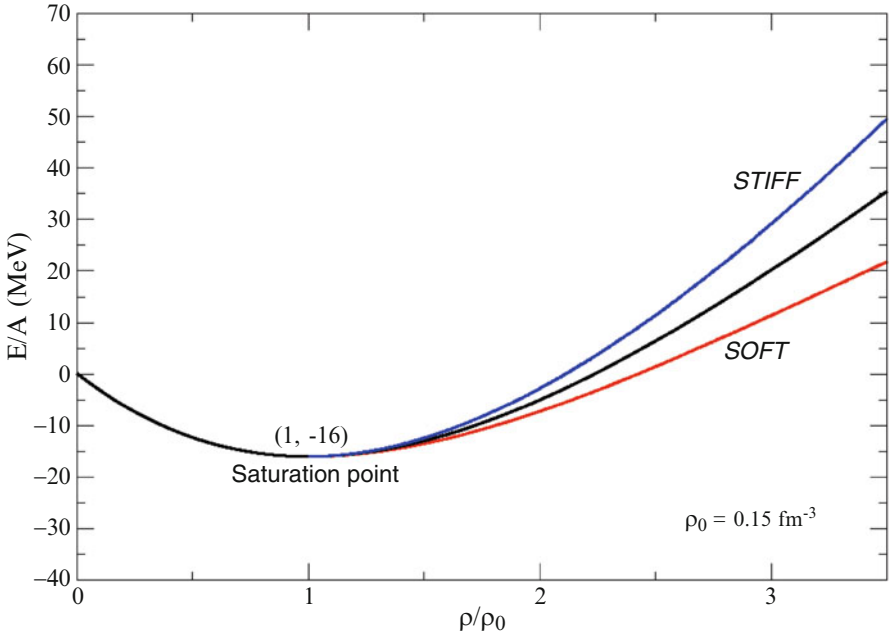

Fig. 1.1 Graphical depiction of the EOS corresponding to different K_∞ values. The curve with lower K_∞ value results in softer EOS as against that with higher K_∞ which corresponds to the stiff EOS. The soft and stiff EOS are with respect to the accepted value of $K_\infty = 240 \pm 20$ MeV (*Black curve*)

explosion, the radii of neutron stars, and nuclear properties such as the neutron-skin thickness of heavy nuclei. It thus becomes important to know the EOS for nuclear matter accurately.

The EOS of nuclear matter is mainly characterized by three quantities, viz. the saturation density (ρ_0), the binding energy per nucleon at the saturation density ($E/A|_{\rho_0}$), and the nuclear incompressibility (K_∞). Of these, the first two have been accurately determined from the previous experiments; $\rho_0 = 0.148\,\text{fm}^{-3}$ and $E/A(\rho_0) \approx -16$ MeV for symmetric nuclear matter [9]. Nuclear incompressibility, the third parameter plays a key role in controlling the behavior of the EOS at high nuclear densities, as seen in astrophysical scenarios like neutron stars and supernova explosions [10, 11], and has not been determined very precisely so far.

The nuclear equation of state (EOS) dictates how the energy per nucleon changes as a function of both the density (ρ) and the neutron-proton asymmetry ($\alpha = (N-Z)/A$). The total energy per particle $\varepsilon(\rho, \alpha)$ can be expanded as a power series in α^2 as [12],

$$\varepsilon(\rho, \alpha) = \varepsilon_{SNM}(\rho) + \alpha^2 S(\rho) + \mathcal{O}(\alpha^4) \tag{1.1}$$

The first term in the expansion corresponds to the energy of symmetric nuclear matter and the first-order correction term is identified as the symmetry energy which is essentially the energy cost incurred in converting symmetric nuclear matter into pure neutron matter. The coefficient α for some of the very neutron rich stable nuclei is, however, a very small number. This makes it difficult to obtain an accurate value of the symmetry energy. The masses of stable nuclei can only provide a meaningful constrains on $S(\rho \approx \rho_0)$; its density dependence remains largely undetermined. In order to probe the density dependence of the EOS one must study the response of the nucleus to external perturbations. The isoscalar giant monopole resonance is one such compression mode of oscillation where protons and neutrons oscillate in phase with each other around the equilibrium density. Thus the ISGMR measures the response of the nucleus to density fluctuations. The ISGMR centroid energy is directly related to the incompressibility of finite nuclei which in turn constrains the incompressibility of the infinite nuclear matter, as described in detail in Sect. 1.3.

The role of ISGMR measurements in constraining the value of nuclear matter incompressibility can be understood through the following discussion. The energy per particle of symmetric nuclear matter and the symmetry energy can be expanded around the equilibrium density as,

$$\varepsilon_{SNM}(\rho) = \epsilon_0 + \frac{1}{2}K_\infty x^2 + \frac{1}{6}Q_\infty x^3 + \ldots$$
$$S(\rho) = J + Lx + \frac{1}{2}K^\infty_{sym} x^2 + \frac{1}{6}Q^\infty_{sym} x^3 + \ldots$$

Here $x = (\rho - \rho_0)/3\rho_0$, K_∞ and Q_∞ are the incompressibility coefficient and skewness parameter of symmetric nuclear matter, and K^∞_{sym} and Q^∞_{sym} are the corresponding quantities for the symmetry energy. By substituting the above expansions into Eq. 1.1 the energy per particle of the asymmetric nuclear matter can be rewritten as,

$$\varepsilon(\rho,\alpha) = (\epsilon_0 + J\alpha^2) + L\alpha^2 x + \frac{1}{2}(K_\infty + \alpha^2 K^\infty_{sym})x^2 + \frac{1}{6}(Q_\infty + \alpha^2 Q^\infty_{sym})x^3 + \ldots \tag{1.2}$$

For the symmetry energy expansion, the density pressure L does not vanish and, as a result, the saturation point in asymmetric matter shifts from $x_0 = 0$ to $\overline{x}_0$, where the latter is defined as the solution to the equation $\partial\varepsilon/\partial x = 0$ [12, 13]. This results in,

$$\overline{x}_0 = -\frac{L}{K_\infty}\alpha^2 \rightarrow \frac{\overline{\rho}_0}{\rho_0} = 1 + 3\overline{x}_0 = 1 - 3\frac{L}{K_\infty}\alpha^2 \tag{1.3}$$

Introducing $\overline{x} = (\rho - \overline{\rho}_0)/3\overline{\rho}_0$ to quantify deviations from the new equilibrium density we obtain,

$$\varepsilon(\rho,\alpha) = (\epsilon_0 + J\alpha^2) + \frac{1}{2}K_\infty(\alpha)\overline{x}^2 + \ldots \tag{1.4}$$

where the incompressibility of the neutron-rich matter is given by,

$$K_\infty(\alpha) = K_\infty + K_\tau^\infty \alpha^2 \equiv K_\infty + \left(K_{sym}^\infty - 6L - \frac{Q_\infty}{K_\infty} L\right)\alpha^2 \tag{1.5}$$

The above equation clearly identifies the importance of ISGMR studies in a series of isotopes. The nuclear incompressibility of the asymmetric nuclear matter is sensitive to the density dependence of the symmetry energy. Therefore, a study of ISGMR centroid energies in a series of isotopes with large variation in asymmetry parameter, α, can provide stringent constraints on the value of K_τ^∞. The asymmetry coefficient of the finite nucleus incompressibility, K_τ, does not include contributions merely from the second derivative of the symmetry energy and hence cannot be identified as K_τ^∞ [7]. However, K_τ is strongly correlated with K_τ^∞ and hence constrains the density dependence of the symmetry energy. Also, the ISGMR centroid energies in a near symmetric nuclei can constrain the value of incompressibility coefficient of symmetric matter, K_∞.

Experimentally constraining the value of nuclear incompressibility of asymmetric nuclear matter, and hence the nuclear symmetry energy, is the main focus of this thesis work.

1.1 Nuclear Matter Incompressibility

Nuclear matter incompressibility is a measure of the curvature of the EOS of nuclear matter at the saturation density, and thus corresponds to the nuclear stiffness [14]. Using a second order Taylor expansion of the EOS around the saturation density leads to,

$$\frac{E}{A}(\rho) = \frac{E}{A}(\rho_0) + \left.\frac{d(\frac{E}{A})}{d\rho}\right|_{\rho_0} (\rho - \rho_0) + \frac{1}{2}\left.\frac{d^2(\frac{E}{A})}{d\rho^2}\right|_{\rho_0} (\rho - \rho_0)^2 \tag{1.6}$$

The second term is zero at the saturation density ρ_0. The coefficient of the third term in the expansion is identified as the nuclear matter incompressibility according to the following definition,

$$K_\infty = 9\rho_0^2 \left.\frac{d^2(\frac{E}{A})}{d\rho^2}\right|_{\rho_0} = k_F^2 \left.\frac{d^2(\frac{E}{A})}{dk_F^2}\right|_{k_{F_0}} \tag{1.7}$$

Here k_F is the Fermi momentum when momentum is used as an independent variable in calculations. K_∞, however cannot directly be determined from experiments. A distinct correlation between K_∞ and an experimental observable is necessary. Among such correlated observables are the nuclear masses, nuclear radii, momentum transfer in high energy nuclear collisions, and some astrophysical observables

such as neutron star masses and radii [15]. However, all of these experimental efforts cannot provide a constraint better than 50–100 MeV on the value of K_∞ which has been calculated to be in the range 200–300 MeV [8]. Much effort has since been put into the study of the compression mode of nuclear oscillations viz. giant resonances (GR). A clear correlation can be developed within mean field calculations between K_∞ and the energies of the compression modes of oscillations observed in nuclei which can be studied in the laboratory. This will be further discussed in detail in Sect. 1.3. Inspite of considerable success, some theoretical concerns still remain within this approach. This thesis work experimentally addresses some of these concerns by providing extensive and important data and paves the way towards future work in this field with radioactive nuclei.

1.2 Giant Resonances

Giant resonances are the high-frequency, damped, (nearly) harmonic density/shape vibrations around the equilibrium density/shape of the nuclear system. These modes correspond to the collective motion of nuclei. Quantum mechanically they are observed as resonances corresponding to transitions between the ground state and the collective states. The strength of these resonances, like for any resonance, is governed by the transition amplitude which in turn depends on the ground state properties of the nuclei, like the size of the system or the number of participating nuclei. Total transition strength is, thus, limited by a *sum rule* which depends on the ground state properties of the nucleus. If a given resonance exhausts more than 50 % of the corresponding sum rule (total transition strength) then it is called a Giant Resonance (GR) [1, 16].

1.2.1 Macroscopic Picture

Macroscopically, GRs are collective nuclear vibrations and there are several modes of such vibrations. Different modes of GRs can be classified based on three important features as described in Fig. 1.2. The two main classes of GRs are the electric and magnetic GRs. The main difference between electric and magnetic resonance comes about based on spin identity. Electric resonances make no distinction between individual spin states of the nucleons. Further classification of GRs is based on multipolarity L, spin S, and isospin T [1]. The differences between isoscalar ($\Delta T = 0$) and isovector ($\Delta T = 1$) comes from the distinction made based on the charge state of the nucleon. In the case of isoscalar electric resonances, protons and neutrons oscillate in phase with each other. Electric isovector resonances result in protons oscillating out of phase with neutrons. Higher order multipolarities correspond to oscillations that differ in geometry.

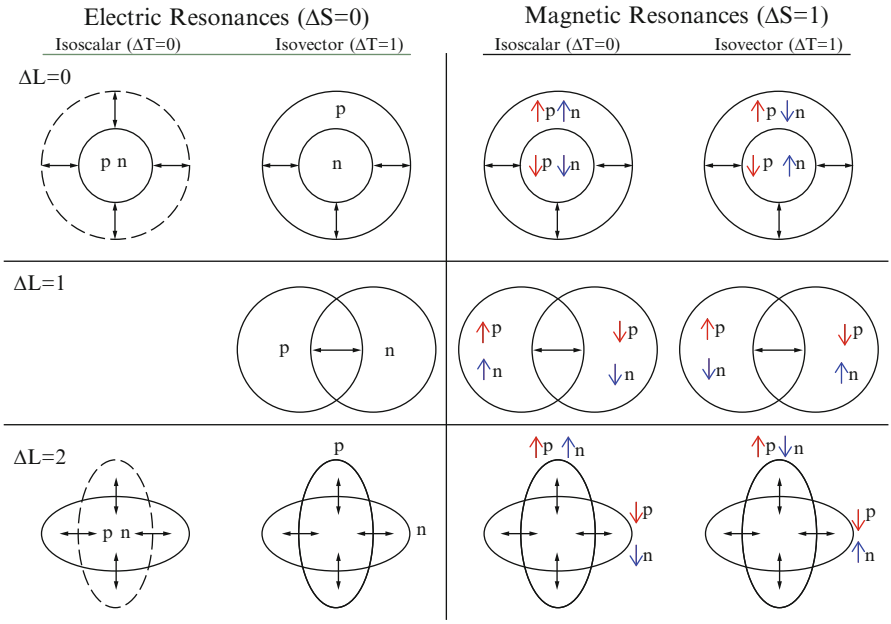

Fig. 1.2 Schematic representation of various collective mode oscillations

1.2.2 Microscopic Picture

In the microscopic picture, GRs can be described as a coherent superposition of particle-hole excitations. In the shell model picture, the single-particle wave functions of subsequent states carry opposite parity and the operator giving rise to GR allows, to first order, only for transitions with $\Delta N \leq L$, where N is the principal quantum number of a given state and L is the multipolarity [17]. Further the parity conservation allows only for $\Delta N = 0,2,4\ldots$ for the even L transitions and $\Delta N = 1,3,5\ldots$ for the odd L transitions. This is summarized in Table 1.1. The lowest excitations, $0\hbar\omega$, corresponds to the rearrangements and transitions within the highest unoccupied major shell, and hence are possible only in open-shell nuclei [1, 16].

In this model, the residual particle-hole (p-h) interaction gives rise to one strong collective state which is a coherent superposition of all possible particle-hole interactions of a given multipolarity and parity. It must be noted that both ISGMR and ISGDR are second-order effects; to first order, the transition operator for ISGMR is a constant which cannot induce any transitions from the ground state to excited states, and that for the ISGDR it corresponds to spurious center-of-mass motion. Further, the p-h residual interaction is positive for the isoscalar transitions and repulsive for isovector excitations. As a result, various resonances overlap in excitation energy; Fig. 1.3 depicts this situation. Further, these resonances have

Table 1.1 Multipole excitations as particle-hole excitations across major shells

	Multipolarity	ΔE		Multipolarity	ΔE
ISGMR	L = 0	$(0\hbar\omega)$,$2\hbar\omega$	ISGQR	L = 2	$(0\hbar\omega)$, $2\hbar\omega$
ISGDR	L = 1	$(1\hbar\omega)$, $3\hbar\omega$	ISGOR	L = 3	$1\hbar\omega$, $3\hbar\omega$
IVGDR	L = 1	$1\hbar\omega$	ISGHR	L = 4	$(0\hbar\omega)$, $2\hbar\omega$, $4\hbar\omega$

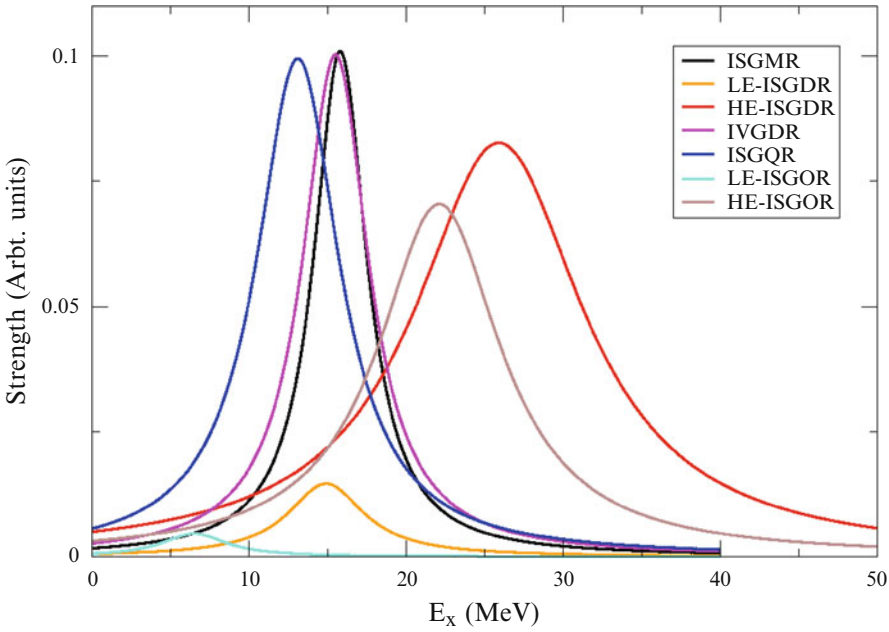

Fig. 1.3 Hypothetical strength distributions for various electric isoscalar giant resonances of ^{116}Sn, indicative of their centroid energies

large widths arising from the mixing of the simple collective 1p-1h state with more complicated 2p-2h states of the same spin and parity [16]. In order to study a specific mode of vibration it thus becomes extremely important to choose the appropriate probe in order to achieve selectivity in exciting the mode of interest. This is discussed in detail in Sect. 1.4. Also, a careful analysis technique becomes crucial in disentangling various multipoles. The theoretical basis of this analysis technique is discussed in the next chapter and its implementation is discussed in Sect. 4.4.

1.2.3 Width of GR

Giant resonances have characteristic widths of the order of 2.5–5 MeV. Its theoretical understanding require a complicated description as stated in Ref. [16]. A brief description of it is presented in this section.

The total width observed experimentally has three different contributions:

$$\Gamma_{total} = \Gamma_{inh} + \Gamma^{\uparrow} + \Gamma^{\downarrow} \tag{1.8}$$

Γ_{inh} is the inherent width or the Landau damping. This width is a result of the spread in excitation energy of the initial 1p-1h strength function. It can be described as the effect of the coupling of the correlated particle-hole excitation with uncorrelated particle-hole configurations in the same excitation-energy range causing a fragmentation of the correlated wave function.

$\Gamma^{\uparrow}$ is the escape width. It corresponds to the direct decay of the collective 1p-1h state in the nucleus A by particle emission. It can be described as resulting from the coupling of the correlated 1p-1h state to the continuum.

$\Gamma^{\downarrow}$ is the spreading width. GRs are located at high excitation energies where a high density of 2p-2h configurations of the same spin and parity as the 1p-1h configuration occurs. This component of the width is associated with the mixing of these more complex and numerous 2p-2h configurations with the correlated 1p-1h state.

1.3 Compressional Mode GRs and Nuclear Incompressibility

A nucleus when set into vibrations can exhibit surface as well as normal modes of oscillations. The normal modes involving compression of nuclear density are called the compressional modes. The two compressional modes of oscillations observed in nuclei correspond to L = 0 (ISGMR) and L = 1 (ISGDR). In the ISGMR mode, the protons and neutrons oscillate in phase with each other and it is often referred to as a "*breathing mode*". The ISGDR mode corresponds to a compression wave moving back and forth keeping the volume of the nucleus constant; such a mode is referred to as a "*squeezing mode*" of oscillation. Nuclear incompressibility of a finite nucleus is directly related to the centroid energy of these two resonances. The E_{ISGMR} and E_{ISGDR} are related to the nuclear compressibility of finite nuclei, in the scaling model, as [18, 19],

$$E_{ISGMR} = \hbar \sqrt{\frac{K_A}{m < r^2 >_0}} \tag{1.9}$$

$$E_{ISGDR} = \hbar \sqrt{\frac{7}{3} \frac{K_A + \frac{27}{25}\epsilon_F}{m < r^2 >_0}} \tag{1.10}$$

Here $< r^2 >_0$ is the ground-state mean-square radius of the nucleus, K_A is its incompressibility, m is the nucleon mass (938.86 MeV/c^2) and ϵ_F is the Fermi energy. It must be further noted that the ISGMR in light nuclei (A $<$ 90) is not a suitable observable to extract K_∞ for the ISGMR strength distribution in light nuclei is highly fragmented [8, 16]. Also, of the ISGMR and ISGDR, the former is often observed as a single well-defined peak while the latter is associated with more complex structure. The ISGDR in most nuclei displays a low-lying, fragmented part which lies below the giant resonance[8]. Different theoretical calculations agree that the low-lying strength is not collective. However, due to these ambiguities the ISGMR is agreed upon as the optimal tool for the study of nuclear incompressibility. Further, one needs to relate K_A to K_∞ in a meaningful and reliable way. This can be achieved using different approaches as discussed in the following subsections.

1.3.1 Macroscopic Approach to K_∞

In the macroscopic liquid drop approach, K_A is expanded in a form similar to the semi-empirical mass formula [19–21] and is written as:

$$K_A = K_{vol} + K_{surf}A^{-1/3} + K_\tau \left(\frac{N-Z}{A}\right)^2 + K_{coul}\frac{Z^2}{A^{4/3}} + K_{ss}\left(\frac{N-Z}{A}\right)^2 A^{-1/3} + K_{cv}A^{-2/3} \tag{1.11}$$

Here N and Z are the number of neutrons and protons and A = N + Z. The contributions from surface-symmetry term (K_{ss}) and the curvature term (K_{cv}) are of higher order and can be neglected [22]. K_τ is the asymmetry term in the nuclear incompressibility. The determination of the various parameters is done by fitting the empirical data. K_∞ is then identified with the volume term K_{vol} as,

$$K_\infty = \lim_{A\to\infty} K_A = K_{vol} \tag{1.12}$$

However, this approach suffers from several ambiguities [8]. First and foremost, the expansion as in Eq. 1.11 is valid only for small amplitude vibration which is true only in heavy nuclei. Further, Eq. 1.12 holds only if the ISGMR is well described by scaling model. The scaling does not work equally well for light as well as heavy nuclei leaving the above assumption rather uncertain. Also, in lighter nuclei, the breathing mode is rather anharmonic and hence the interpretation of various terms in the expansion is more complicated. Aside from these difficulties, there is also a practical difficulty of determining the parameters in Eq. 1.11 from fits to the limited set of data points. It has been shown that equally good fits can be obtained with the volume term taking arbitrary values in a wide range; $100 \leq K_{vol} \leq 400$ MeV [20, 23]. These difficulties have been reconciled by Treiner et al. [19]. They have shown that in order to get meaningful results, one has to take into account, within a specific model, the known correlations between various parameters, reducing the parameter set to one. This leads to a value of K_∞ that is compatible with the microscopic calculations.

1.3.2 Microscopic Approach to K_∞

In the microscopic picture, the basic idea consists of using energy functionals, $E(\rho)$, which allow for calculating nuclear matter and finite nuclei on the same footing [24]. In both non-relativistic and relativistic cases, the second derivative of the energy functional can be calculated analytically for uniform nuclear matter and the value of K_∞ associated with a given pameterization is obtained. In the case of finite nuclei, one calculates the monopole excitation using self-consistent linear response theory. Using a set of different parametrizations (within a given class of energy functionals) characterized by different values of K_∞, self-consistent RPA calculations of the ISGMR are performed in a given nucleus. For a single well defined monopole peak, Eqs. 1.11 and 1.12 suggest a relation of the type, $E_{ISGMR} \sim a\sqrt{K_\infty} + b$ [8]. The experimental value of E_{ISGMR} is then used to extract the value of K_∞. However, the use of different interactions within the self-consistent RPA formalism results in varied values of K_∞. Initially, nonrelativistic calculations that reproduce isoscalar monopole strength distribution in ^{208}Pb resulted in $K_\infty = 210$–230 MeV, while relativistic models point toward $K_\infty \simeq 270$ MeV.

The solution to this puzzle came from an important realization that the ISGMR in ^{208}Pb does not constrain the compression modulus of *symmetric* nuclear matter but rather the one of *neutron-rich* matter [9, 25, 26]. This explained how models with significantly different K_∞ values may still reproduce monopole strength in ^{208}Pb. Accurately-calibrated theoretical models were built to reproduce simultaneously the distribution of isoscalar monopole strength in nuclei with significantly different nucleon asymmetries; viz. ^{90}Zr and ^{208}Pb. With this treatment, the relativistic and non relativistic models have reached a consensus for the value of the incompressibility of symmetric nuclear matter at $K_\infty = 240 \pm 20$ MeV [26].

1.4 Experimental Tools to Study ISGMR

As discussed at the end of Sect. 1.2.2, the choice of the experimental tool used to study the GRs is very important. The various tools available to study GRs are summarized in Fig. 1.4. In the inelastic scattering of charged hadrons, i.e. protons, α-particles and heavy ions, both nuclear and electromagnetic interactions contribute, but for lighter nuclei the nuclear interaction dominates. Isovector resonances, as shown in Fig. 1.2, discriminate between protons and neutrons. These modes are, therefore, not important from the point of view of extracting nuclear incompressibility which is a bulk property of nuclei. These modes can be studied using electromagnetic probes or using charge-exchange reactions. The isovector giant monopole resonance is often studied by pion charge exchange reactions. Further isovector giant dipole resonances (IVGDR) has been extensively studied in photo-absorption experiments. Inelastic electron scattering can be used to excite isoscalar as well as isovector resonances. However both modes are equally excited and hence the interpretation of such experiments is not straightforward.

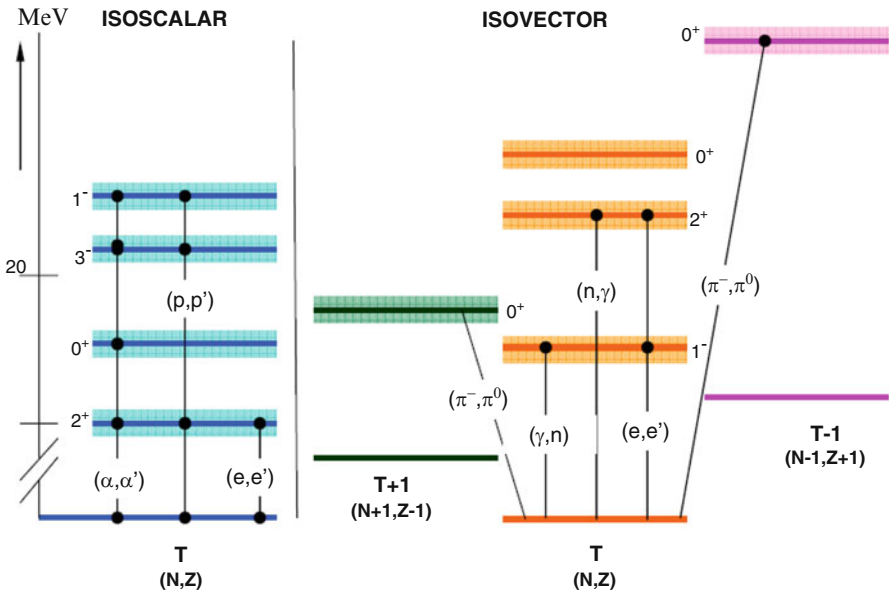

Fig. 1.4 The most commonly used tools to study GRs in nuclei [1, 2]

1.4.1 The Selectivity of α and Deuteron Probes

In the study of ISGMR, inelastic α-scattering has an advantage that to first order it only excites isoscalar electric modes ($\Delta S = 0$) since it carries no spin ($S = 0$) and cannot *magnetically* couple to the target nucleus. For proton-even neutron-even target nuclei this implies that the spin and parity of the excited state can be given by ΔL and $(-1)^{\Delta L}$. Coulomb excitation and isospin mixing in the ground-state can result in small contributions from isovector modes. Of these, only Coulomb excitation is important for small-angle scattering in which case it results predominantly in excitation of the IVGDR. The effect of Coulomb excitation is rather small but it is included in the analysis of the experimental data. Isospin mixing in the ground-state of nuclei results from the difference in radii of neutron and proton distributions in nuclei. It gives rise to a small isovector cross-section and is mostly ignored. Indeed, α-scattering remains the best probe for the investigation of isoscalar electric giant resonances [1, 16]. Deuteron has an isospin of zero ($T = 0$) and hence is also mainly an isoscalar probe. Spin-flip excitations are also possible with the use of deuteron inelastic scattering since it carries a spin of 1 unit in its ground state. However, the corresponding cross-sections are strongly reduced as compared to those for non-spin-flip excitations [27, 28]. Clearly, establishing the feasibility of using deuterons as a probe to study the ISGMR is one of the goals of this work.

1.5 Motivation

Current work constitutes three different experiments each of which were performed at the Research Center for Nuclear Physics (RCNP), Osaka university, Japan. The experimental details are given in Chap. 3. This section describes the motivation for the three experiments undertaken as a part of this work.

1.5.1 E-309

This experiment was carried out with the aim of measuring ISGMR in a series of Cd isotopes. As mentioned earlier, it was realized that the ISGMR properties of ^{208}Pb constrain the nuclear incompressibility of neutron rich matter at the particular value of the neutron excess, that corresponding to ^{208}Pb [9, 25, 26]. Also the ISGMR in ^{208}Pb was found to be sensitive to the density dependence of the symmetry energy. Symmetry energy is, to an excellent approximation, equal to the difference between the energy of pure neutron matter and that of symmetric nuclear matter. As the infinite nuclear system becomes neutron rich, the saturation density lowers, the binding energy weakens and the nuclear incompressibility *softens*. Thus, K_∞ of a neutron rich system having the same neutron excess as ^{208}Pb is *lower* than the K_∞ of symmetric nuclear matter. The important realization that the ISGMR strength distributions in heavy nuclei are sensitive to the density dependence of the symmetry energy motivated experimental measurements of GRs in a series of isotopes.

The first such experiment was performed on a series of Sn isotopes. Experimental results of this experiment revealed interesting features as shown in Fig. 1.5 [24, 29]. As can be seen, the accurately-calibrated models that reproduce the ISGMR in ^{90}Zr, ^{144}Sm and ^{208}Pb overestimate the distribution of the ISGMR in the Tin isotopes. An attempted solution to the observed discrepancies in the Sn isotopes (as described above) was that of the inclusion of the pairing interactions in the calculations. However that reduced the discrepancy by only about 150 keV in the case of Sn isotopes [4, 30–32] and despite concerted theoretical effort in recent years the challenge still remains to simultaneously describe the ISGMR in open-shell nuclei as well as in the doubly magic ^{208}Pb and ^{90}Zr nuclei [12, 31–34]. This was identified as one of the"open" problems in nuclear structure in a recent major compilation [35].

However, the results of this experiment were the only ones available on a series of isotopes until then. It was thus imperative to make measurements on another series of isotopes in a similar mass region. The ideal choice for such an experiment was the study of the ISGMR in the even-even $^{106,110-116}$Cd isotopes. A systematic study of the ISGMR in Cd isotopes forms a part of this thesis work.

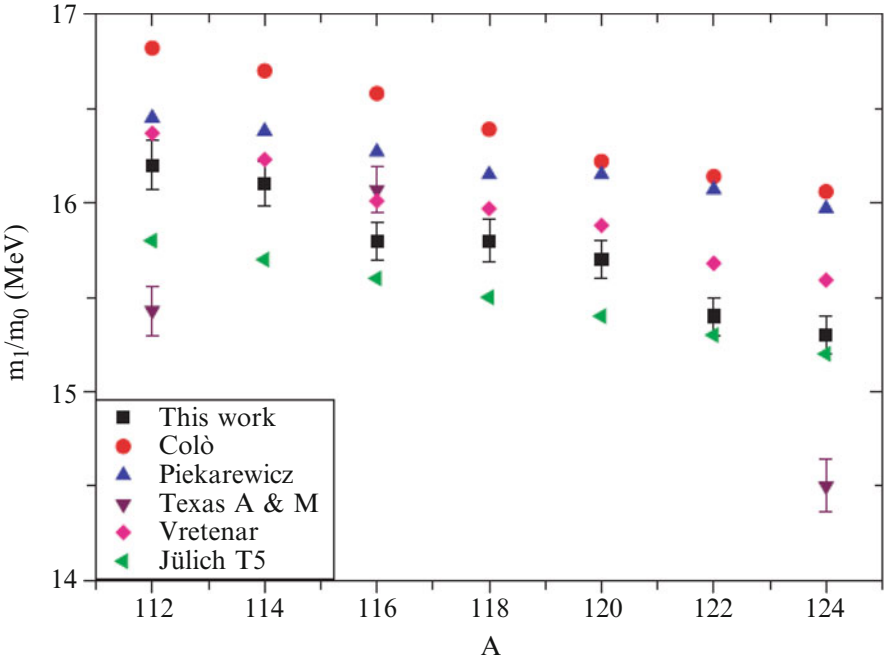

Fig. 1.5 Comparison between the ISGMR centroid energies (m_1/m_0) in all neutron-even $^{112-124}$Sn isotopes. The experimental results (*filled squares*) are compared with results from nonrelativistic RPA calculations (without pairing) by Colò et al. (*filled circles*), relativistic calculations of Piekarewicz (*triangles*), RMF calculations from Vretenar et al. (*diamonds*), and QTBA calculations from the Jülich (*triangles*) group (*sideways triangles*). Results for ^{112}Sn, ^{116}Sn and ^{124}Sn reported by the TAMU group are also shown (*inverted triangles*)

1.5.2 E-340

Amidst various efforts of resolving the discrepancy, it was argued that ^{208}Pb, being a doubly-magic nucleus, is "stiffer" than the open-shell nuclei and the incompressibility obtained from doubly-magic nuclei would invariably lead to an overestimation of the ISGMR energies in the open-shell nuclei [36]. This was included in the form of the mutually enhanced magicity (MEM) effect in the calculations of the ISGMR centroid energies in the constrained Hartree-Fock-Bogoliubov (CHFB) framework [32]. An important prediction of the inclusion of the MEM effect in the calculations of the ISGMR centroid energies was that the ISGMR centroid energy in ^{208}Pb would be higher than the corresponding values in the ^{204,206}Pb isotopes by $\sim$600 keV as shown in Fig. 1.6. E-340 was performed to explore the role of MEM in the nuclear incompressibility and to verify the theoretical prediction of the ISGMR centroid energies in the Pb isotopes.

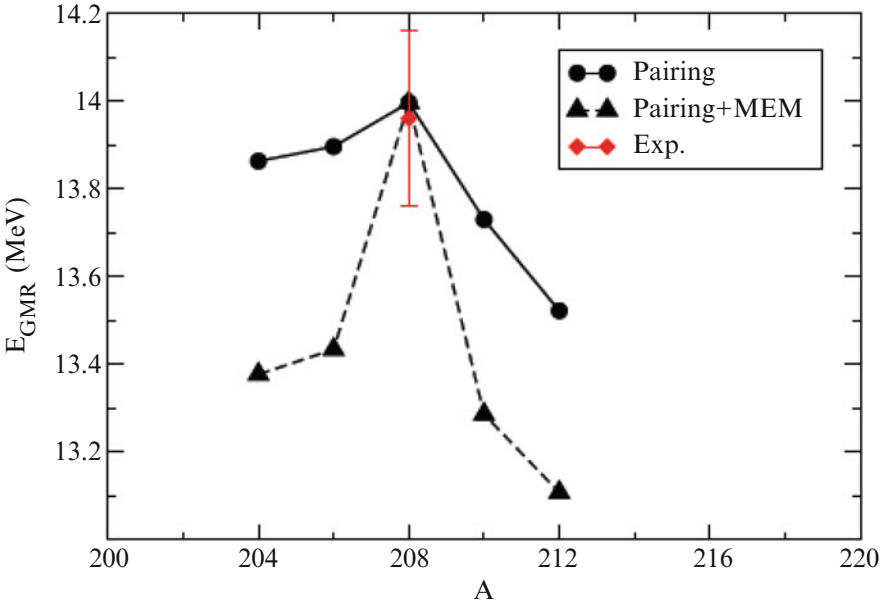

Fig. 1.6 Excitation energies of the ISGMR in $^{204-212}$Pb isotopes calculated with constrained HFB method, taking into account the MEM effect [3]

1.5.3 E-318

In the future one needs to explore the nuclear incompressibility in the neutron-rich nuclei, far from valley of stability, with an aim to shed more light on the role of the symmetry energy. Further interest in the ISGMR strengths in nuclei far from stability, especially on the neutron-rich side, stems from the possible investigation of many important, and intriguing, nuclear structure effects, such as the theoretically predicted appearance of monopole strength below the particle threshold: the "pygmy" ISGMR [37–39], akin to the "pygmy" dipole resonances reported in several neutron-rich nuclei (see, for example, Ref. [40]). The advent of new radioactive-ion beam facilities makes these investigations feasible. Inverse-kinematics measurements can be made using an active target system (such as MAYA [41] at GANIL or IKAR [42] at GSI, for example) wherein the detector gas also acts as the target. In the first such measurement, using MAYA, an enhancement of the giant resonance (GR) strength was observed on top of the underlying continuum in the ^{56}Ni nucleus and it was demonstrated that this "bump" could be construed as corresponding to a combination of the ISGMR and the isoscalar giant quadrupole resonance (ISGQR) [43, 44]. This measurement used deuterium as the active target/detector gas. Indeed, as documented in Ref. [44], it proved impossible to operate the counter with pure He gas, hence ruling out α particles as the probe of choice for ISGMR investigations in radioactive nuclei.

As an isoscalar particle, the deuteron (d) is ideally suited for investigation of the ISGMR and some experimental work with this projectile was carried out in the 1970s [45, 46]. Specifically, Willis et al. [46] performed a (d,d') measurement at 54 MeV/A, where inelastic cross-sections for giant resonances are rather low. Moreover, the GR strength distributions for various multipoles were extracted using peak fitting, a method deemed less reliable than the multipole decomposition analysis (MDA) technique currently in use. This lack of prior knowledge of GR excitation using a deuteron probe rendered the analysis difficult in the aforementioned ^{56}Ni investigation as it was not possible to clearly delineate the ISGMR and ISGQR strengths. The experiment reported here was performed to investigate the GR with the deuteron probe at a beam energy of 100 MeV/u, amenable to reasonable cross sections for excitations of the GR.

Chapter 2
Theory of Collective Motion

2.1 Introduction

GRs are collective phenomenon. They can be viewed as a coherent superposition of one-particle one-hole (1p-1h) interactions. The nucleon in the target nucleus can be excited into bound or quasi-bound states which gives rise to the 1p-1h state of the target nucleus. The excitation strength tends to be concentrated, by constructive superposition of 1p-1h excitations, into one or few of the levels in each shell. Thus, mathematically if the observed resonance exhausts a large fraction of the corresponding transition strength (sum rule) it is identified as a giant resonance.

As discussed in the previous chapter, GRs corresponding to different multipolarities overlap in excitation energy and specifically with their large widths it becomes rather difficult to disentangle different modes of GR excitations. In order to achieve this disentanglement, we adopt a method of multipole decomposition analysis (MDA); its implementation is discussed in detail Sect. 4.4. The theoretical ingredients required to perform this analysis are discussed in this chapter.

2.2 Distorted-Wave Born Approximation (DWBA)

Inelastic scattering direct reaction, is known to preferentially excite the collective states of the vibrational and rotational type [47]. In order to extract the strength distribution of the giant resonance it is necessary to evaluate the differential cross-section for inelastic scattering which in turns requires the use of the DWBA formalism. The detailed description of the DWBA formalism can be found in Ref. [47]; only salient details are provided in this section.

Consider a two-body scattering system, a+A $\rightarrow$ b+B. Let the entrance channel be denoted by α and the exit channel by β. The total Hamiltonian, H, of the system

D.C. Patel, *A Study of the Isoscalar Giant Monopole Resonance*, Springer Theses,
DOI 10.1007/978-3-319-22207-3_2

is the sum of the internal Hamiltonian for nucleus a and A, H_α, the kinetic energy of their relative motion K_α, and the mutual interaction potential V_α. The total wavefunction ψ contains incoming plane waves only in the ground-state α channel but will have outgoing spherical waves in all the channels which are open at the given incident energy. It is denoted as $\Psi_\alpha^{(+)}(\vec{k_\alpha})$, where $(+)$ indicates that we are choosing an outgoing wave and α means it arises from an incident wave in the α channel. This wavefunction can be expanded in terms of a complete set of internal states in channel β as,

$$\Psi_\alpha^{(+)} = \sum_\beta \zeta_\beta(\vec{r_\beta})\psi_\beta(x_\beta) \tag{2.1}$$

For the appropriate boundary conditions, ζ_β takes the form,

$$\zeta_\beta(\vec{r_\beta}) \rightarrow e^{i\vec{k}_\alpha \cdot \vec{r}_\alpha}\delta_{\alpha\beta} + f_{\beta\alpha}(\vec{\hat{r}}_\beta, \vec{k}_\alpha)\frac{1}{\vec{r}_\beta}e^{ik_\beta r_\beta} \tag{2.2}$$

where, $f_{\beta\alpha}(\vec{\hat{r}}_\beta, \vec{k}_\alpha)$ is the transition amplitude. Asymptotically, the relative momentum $\vec{k}_\beta$ has the same direction as $\vec{r}_\beta$, hence $f_{\alpha\beta}$=$f_{\beta\alpha}$. If the β and α partitions are the same, $f_{\beta\alpha}$, refers to elastic ($f_{\alpha\alpha}$) or inelastic ($f_{\alpha\alpha'}$) scattering. The differential cross-section for the transition from channel α to channel β is defined as the ratio of the outgoing flux per unit time going into the small area subtending a solid angle $d\Omega$ in channel β, $|J_0^\beta|r_\beta^2 d\Omega$, to the incident flux per unit time and unit area in channel α, $|J_i^\alpha|$,

$$\frac{d\sigma_{\beta\alpha}}{d\Omega}d\Omega = \frac{|J_0^\beta|r_\beta^2 d\Omega}{|J_i^\alpha|}$$

$$\frac{d\sigma_{\beta\alpha}}{d\Omega} = \frac{\mu_\alpha k_\beta}{\mu_\beta k_\alpha}|f_{\beta\alpha}(\vec{k}_\beta, \vec{k}_\alpha)|^2 \tag{2.3}$$

Here, $\mu_\alpha = m_a M_A/(m_a + M_A)$ and $\mu_\beta = m_b M_B/(m_b + M_B)$. Thus, in order to obtain the differential cross-section for inelastic scattering, the transition amplitudes, $f_{\beta\alpha}(\vec{k}_\beta, \vec{k}_\alpha)$, need to be evaluated. The evaluation of the transition amplitude requires knowledge of the interaction potential and the wavefunction. The exact expression for the normalized transition amplitude can be obtained by solving the Schroginger's equation using the appropriate form of the Hamiltonian,

$$(H - E)\Psi_\alpha^+ = (H_\beta + K_\beta + V_\beta - E)\Psi_\alpha^+ = 0$$

$$T_{\beta\alpha}(\vec{k}_\beta, \vec{k}_\alpha) = < e^{i\vec{k}_\beta \cdot \vec{r}_\beta}\psi_\beta|V_\beta|\Psi_\alpha^{(+)}(\vec{k}_\alpha) > \tag{2.4}$$

Here, $\Psi_\alpha^{(+)}$ is the wavefunction corresponding to the physical situation wherein it contains incoming plane waves only in the ground state α channel but will

have outgoing spherical waves in α and all other channels which are open at the given energy. The procedure to estimate $\Psi_{\alpha}^{(+)}$ is called the distorted wave Born approximation (DWBA).

One of the possible ways to determine $\Psi_{\alpha}^{(+)}$ is to introduce an auxiliary potential $U_{\beta}(r_{\beta})$ such that, $V_{\beta}(\chi_{\beta},\vec{r}_{\beta}) = U_{\beta}(r_{\beta}) - W_{\beta}$. Although the auxiliary potential U_{β} is arbitrary in principle, the motivation for introducing it is to include a large part of the average effects of the interaction V_{β} so that the effects of the inhomogeneous term may be minimized. Then the remaining or the residual interaction, W_{β}, can be treated as a perturbation. The formal solution on the following modified equation,

$$[E_{\beta} - K_{\beta} - U_{\beta}(r_{\beta})]\zeta_{\beta}(\vec{r}_{\beta}) =< \psi_{\beta}|W_{\beta}|\Psi_{\alpha}^{(+)} > \tag{2.5}$$

may be expressed in terms of the solutions of the homogeneous equation,

$$[E_{\beta} - K_{\beta} - U_{\beta}(r_{\beta})]\chi_{\beta}^{(+)}(\vec{k}_{\beta}, \vec{r}_{\beta}) = 0 \tag{2.6}$$

These $\chi_{\beta}^{(+)}$ are known as the distorted waves and describe the (elastic) scattering of b on B due to the potential U_{β} by itself. Asymptotically they have the form of an incident plane wave plus outgoing (scattered) spherical waves [hence the (+) superscript],

$$\chi_{\beta}^{(+)}(\vec{k}_{\beta}, r_{\beta}) \rightarrow e^{i\vec{k}_{\beta}\cdot\vec{r}_{\beta}} + f_{\beta}^{(0)}(\theta)\frac{1}{r_{\beta}}e^{ik_{\beta}r_{\beta}} \tag{2.7}$$

where $f_{\beta}^{(0)}(\theta)$ is the scattering amplitude due to U_{β} alone. One can measure the elastic scattering cross-section experimentally and fit it to get the appropriate U_{β}. The U_{β} we get represents the average of V_{β} over the internal ground state of a channel. Usually, the distorted waves are generated in a complex optical potential which is empirically obtained by requiring a good fit to the elastic scattering data. The optical model is discussed in detail in Sect. 4.2.

Further the study of the GR via inelastic scattering requires a transition potential for the calculation of the differential cross-section of inelastic scattering within this DWBA framework. This in turn requires a construct of transition densities which can be calculated based on the appropriate sum rules. These theoretical constructs, necessary for calculations of the GR cross-sections, are discussed in the remainder of this chapter.

2.3 Sum Rules

GRs can be described as the response of the nucleus to a weak external field, such that a linear approximation can be applied. This field can be decomposed into various multipoles and the response can thus be viewed as the sum of the

various contributions of the multipole GRs. GRs exhaust a large fraction of the transition strengths (sum rules) connected with the multipole transition operators of the external fields responsible for their excitation. In the analysis of GR spectra, it is very useful to make use of sum rules which can be derived from the algebraic relations between the transition operators and the Hamiltonian or powers thereof. Most interesting for the isoscalar electric modes are the so-called energy weighted sum rules (EWSR) because they can be determined model independently and depend only on the ground-state properties of the nucleus. The linear EWSR can be expressed as an expectation value of a one-body operator and is therefore relatively insensitive to the detailed correlations in the initial state [14]. EWSR is often used as a measure of the strength of the giant resonance. It is defined as a sum of the transition probabilities from ground state to excited states for a certain multipolarity, multiplied respectively by the excitation energy,

$$S(O_\lambda \mu) \equiv \sum_n (E_n - E_0)| < n|O^{\lambda\mu}|0 > |^2 \tag{2.8}$$

where n labels the complete set of excited states that can be reached by operating with $O^{\lambda\mu}$ on the initial state $|0>$. λ and μ refer to the multipolarity and isospin structure of the resonance. For the multipole field operator,

$$O^{\lambda\mu} = \sum_{i=1}^{A} f(r_i) Y_L^M(\Omega_i) \tag{2.9}$$

EWSR can be evaluated as,

$$S(O^{\lambda\mu}) = \frac{2\lambda+1}{4\pi}\frac{\hbar^2}{2m}A\left\langle \left(\frac{df}{dr}\right)^2 + \lambda(\lambda+1)\left(\frac{f}{r}\right)^2 \right\rangle \tag{2.10}$$

Here A is the particle number of the system. Using the appropriate operator definition and following the recipe provided in Refs. [16, 48] one obtains the expressions for the EWSR corresponding to multipoles.
For the ISGMR ($\lambda = 0$), corresponding to the second order field operator,

$$O^{00} = \sum_{i=1}^{A} r_i^2 Y_0^0$$

$$S_{00} = \frac{2\hbar A}{m} < r^2 > \tag{2.11}$$

For the ISGDR ($\lambda = 1$), corresponding to the second order field operator,

$$O^{10} = \frac{1}{2}\sum_{i=1}^{A} r_i^3 Y_1^0(\Omega_i)$$

$$S_{1,0} = \frac{3\hbar^2 A}{32m\pi}[11 < r^4 > -(25/3) < r^2 >^2 -10\epsilon < r^2 >] \tag{2.12}$$

with,

$$\epsilon = \frac{\hbar^2}{3mA}\left(\frac{4}{E_{ISGDR}} + \frac{5}{E_{ISGQR}}\right) \tag{2.13}$$

For higher multipoles ($\lambda \geq 2$) corresponding to the multipole field operator defined by Eq. 2.9,

$$S_{\lambda,0} = \frac{\hbar^2 A}{8\pi m}\lambda(2\lambda+1)^2 < r^{2\lambda-2} > \tag{2.14}$$

Here, A is the mass of the nucleus, m is the nucleon mass (938.86 MeV/c^2) and $< r^2 >$ is the mean square radius of the nuclear density. Also $E_{ISGQR} = 65A^{-1/3}$ MeV and $E_{ISGMR} = 80A^{-1/3}$ MeV are the excitation energies of the ISGQR and ISGMR. $< r^n >$ are the radial moments of the ground state densities and can be calculated using a Fermi-mass distribution with parameters deduced from electron scattering, for instance. The second and third terms in Eq. 2.12 correspond to the center-of-mass corrections. All the above expressions for the EWSR hold for a specific form of operator $O^{\lambda\mu}$ which hold for light probes like α-particles and deuterons.
NOTE: Eq. 2.11 is normalized with respect to $Y_0^0 = (4\pi)^{-1/2}$ as described in Ref. [49]. Most DWBA and coupled-channel codes follow this convention. Also the EWSR definition for ISGDR, Eq. 2.12, incorporates the three magnetic sub-states of the L = 1 multipole; m = −1, 0, 1.

2.4 Transition Densities and Transition Potentials

Two important ingredients for describing the collective motion are transition densities and the transition potentials. The construction of these is discussed in this section.

2.4.1 Transition Densities

The basic idea to obtain the transition density is to take a spherically symmetric density distribution ρ(r) and introduce certain multipole deformation parameters. These parameters are the dynamical variables of the model [47].
For multipolarities, $\lambda \geq 2$:
The deformation in the nucleus can be introduced using different prescriptions giving rise to different models for the construction of transition densities. The most commonly used prescriptions are the Tassie model and the Bohr-Mottelson(BM) collective model. Of these, as has been noted in Ref. [49], the BM model is frequently used for the low-lying collective states. On the other hand, it has been noted in Ref. [50], that the systematic errors associated with the model dependence of the transition densities is typically 5 %, except for higher excitation energies $E_x \geq 27$ MeV where the difference is about 20 %. Hence the BM model has been chosen for the construction of the transition densities for the low lying discrete states as well as the giant resonances with multipolarities $\lambda \geq 2$.

Assuming an incompressible nucleus with a density distribution ρ(r) = constant in the interior and a sharp edge r = R_0, the deformation is the introduced by making the edge position angular dependent,

$$R_0 \rightarrow R(\theta, \phi) = R_0[1 + \sum_{\lambda \geq 2, \mu} \alpha_{\lambda\mu} Y^{\mu}_{\lambda}(\theta, \phi)^*] = R_0 + \delta R(\theta, \phi) \tag{2.15}$$

This prescription for deformation can be easily transferred to a nuclear density distribution and following the standard macroscopic description given in Ref. [49], one obtains the expression for the transition density for $\lambda \geq 2$,

$$\delta\rho_{\lambda}(r) = -\delta_{\lambda} \frac{d}{dr} \rho_{gs}(r) \tag{2.16}$$

where ρ_{gs} is the ground state density, and the deformation length, δ_{λ}, is given by,

$$\delta^2_{\lambda} = \frac{2\pi\hbar^2}{AmE_x} \frac{\lambda(2\lambda+1)^2}{(L+2)^2} \frac{< r^{2\lambda-2} >}{< r^{\lambda-1} >^2} \tag{2.17}$$

For multipolarity λ=0:
The ISGMR is a mode of oscillation in which the central density of the nuclear matter oscillates about its equilibrium value with high frequency. This mode may be generated by simple radial scaling [47],

$$r \rightarrow r' = r(1 - \alpha_0) \tag{2.18}$$

of the equilibrium density ρ(r),

$$\rho(r) \rightarrow N\rho(r') = \rho(r) + \delta\rho(r) \tag{2.19}$$

where N is the renormalization factor required to conserve the number of particles, viz. $\int \delta\rho(r) r^2 dr$=0. Combining Eqs. 2.18 and 2.19 one obtains,

$$N\rho(r') = N\rho(r - r\alpha_0) \sim N\rho(r) - Nr\alpha_0 \frac{d\rho(r)}{dr} = \rho(r) + \delta\rho(r) \tag{2.20}$$

The transition density can then be expressed as,

$$\delta\rho(r) = (N-1)\rho(r) - Nr\alpha_0 \frac{d\rho(r)}{dr} \tag{2.21}$$

The particle conservation condition applied on the above equation in addition to the assumption that $\alpha_0 \ll 1$, results in the transition density expression,

$$\delta\rho_0(r) \sim -\alpha_0 \left[3 + r\frac{d}{dr}\right] \rho_{gs}(r) \tag{2.22}$$

where the dimensionless amplitude, α_0, is given by,

$$\alpha_0^2 = \frac{2\pi\hbar^2}{AmE_x < r^2 >} \tag{2.23}$$

For multipolarity $\lambda = 1$:
The collective formalism to describe the ISGDR mode of excitations in electron scattering was first proposed by Deal et al. [51], and later extended to those excited with hadron scattering by Harakeh and Dieperink [48]. Further, the ISGDR operator to first order, $O^{10} = \sum_{i=1}^{A} r_i Y_1^0$, can only result in a translation of the center of mass (cm). The effects of the spurious cm motion induced by this first-order transition operator should be taken care of exactly, even if the second-order transition operator, $O^{10} = \frac{1}{2}\sum_{i=1}^{A} r_i^3 Y_1^0$, which corresponds to the intrinsic dipole oscillation, is used. Using the prescription described in Ref. [16], the transition density for the ISGDR is expressed as,

$$\delta\rho_1(r) = -\frac{\beta_1}{\sqrt{3}c}\left[3r^2\frac{d}{dr} + 10r - \frac{5}{3} < r^2 > \frac{d}{dr} + \epsilon\left(r\frac{d^2}{dr^2} + 4\frac{d}{dr}\right)\right]\rho_{gs}(r) \tag{2.24}$$

with the deformation parameter, β_1, is given by,

$$\beta_1^2 = \frac{6\pi\hbar^2}{mAE_x} \quad \frac{c^2}{11 < r^4 > -\frac{25}{3} < r^2 >^2 -10\epsilon < r^2 >} \tag{2.25}$$

Here, c is the half radius of the Fermi mass distribution and ϵ is as defined in Eq. 2.13. The second and third terms in the denominator of Eq. 2.25 are due to center-of-mass corrections. The second term is large in all nuclei, whereas the third term is proportional to A^{-1} and negligible for $A \geq 40$ nuclei.
Note: The transition density for the ISGDR, Eq. 2.24, corresponds to one out of three magnetic substates for L = 1, as derived in Ref. [48]. The correction to this equation can be made by multiplying the transition density by a factor of $\sqrt{3}$ as

discussed in Ref. [52] or equivalently by using the correct expression for the EWSR [16]. Often these different approaches are discussed in the literature [52, 53] and a consistent treatment is necessary. We have adopted the method of incorporating the three magnetic substate contributions into our expression for the EWSR, Eq. 2.12.

2.4.2 Transition Potentials

A transition potential is required to calculate the differential cross-section for inelastic scattering. The transition potentials are obtained from the phenomenological optical model potential in a procedure that is called the deformed potential model (DPM). DPM is based on the simple and plausible assumption that the shape of the optical potential for the scattering pairs follows the shape of the density distribution of the target and is either statically deformed or undergoing shape oscillations in the same way [16, 47]. With this assumption, the transition potential can be obtained immediately by analogy with the transition density introduced in the previous section as follows [49],

For $\lambda \geq 2$:

$$U_\lambda(r) = -\delta_\lambda \frac{dU_{OM}}{dr} \tag{2.26}$$

For $\lambda = 0$:

$$U_1(r) = -\alpha_0 \left[3 + r\frac{d}{dr}\right] U_{OM}(r) \tag{2.27}$$

For $\lambda = 1$:

$$U_1(r) = -\frac{\beta_1}{c}\left[3r^2\frac{d}{dr} + 10r - \frac{5}{3} < r^2 > \frac{d}{dr} + \epsilon\left(r\frac{d^2}{dr^2} + 4\frac{d}{dr}\right)\right] U_{OM}(r) \tag{2.28}$$

Here, δ_λ, α_0, β_1 and ϵ are given by Eqs. 2.17, 2.23, 2.25 and 2.13 respectively. U_{OM} is the complex optical model potential obtained phenomenologically by fitting to the elastic scattering data.

The construction of the transition potential described above has some ambiguities which have to be fixed before performing the actual DWBA calculations. One of them is related to the deformation parameter defined above. In most cases the real and the imaginary parts of the optical potential have different geometries resulting in real and imaginary coupling parameters β_R and β_I. This is resolved by adopting the prescription which rests on the idea of constancy of the deformation length, βR, for a certain transition resulting in [16]:

$$\beta_R R_R = \beta_I R_I \tag{2.29}$$

Further, at bombarding energies of $\leq$100 MeV/u, the inelastic cross-section can be explained as mainly due to real coupling, i.e. the real part of the transition potential has the largest contribution to the inelastic cross-section. The most general method is to take the coupling which has the largest contribution to the cross-section obtained from inelastic scattering and assume that the corresponding deformation length (βR) is a constant to which all other deformation lengths are set equal using Eq. 2.29. We use the method of an implicit folding model. It has been argued that the radial moments can be evaluated with respect to the real part of the optical potential on the basis of theorem by Satchler [54],

$$< r^{\lambda} >_{gs} = < r^{\lambda} >_{opt} \tag{2.30}$$

This is strictly true if the optical potential is assumed to be implicitly derived from folding the ground state density independent projectile-nucleon interaction, which is the case for our α analysis. For the deuterium inelastic scattering pure phenomenological optical potential is used for fitting the elastic scattering data. In this case, we use a method proposed by Bernstein [55], wherein the deformation length of the ground-state density (Fermi shape distribution) is assumed to be equal to the deformation length of the optical potential. The radial moments are then calculated with respect to the Fermi mass distribution and substituted in the formulae for the reduced transition matrix elements and the EWSRs.

Secondly, for the transition density the radial moments are calculated with respect to the ground-state density. However, since the transition potential is derived from the optical potential, then in the case of ISGDR $\mathrm{ReU_1}$, $< r^2 >_R$ should be taken with respect to the real part of the optical potential, U_{OM}, and similarly for $\mathrm{ImU_1}$, $< r^2 >_I$ should be taken with respect to the imaginary part of U_{OM}. This is necessary for a proper treatment of the spurious cm motion.

2.5 Contribution from the Isovector Giant Dipole Resonance

The isovector giant dipole resonance (IVGDR) is excited through the Coulomb interaction in the (α, α') reaction. Hence, the contribution from the IVGDR needs to be considered in the analysis. If the IVGDR component is fitted as a free parameter in the MDA, the results of MDA are ambiguous in the lower excitation energy range. This component is therefore estimated and subtracted out of the experimental differential cross-section before the fitting procedure. This is done making use of the available experimental data on the photo-nuclear cross-sections [56, 57].

In the semiclassical theory of the interaction of photon with nuclei, the shape of a fundamental resonance in the absorption cross-section is assumed to be described by the Lorentz function,

$$\sigma(E_x) = \frac{\sigma_m}{1 + [(E_x^2 - E_m^2)^2 / E_x^2 \Gamma^2]} \tag{2.31}$$

where, the Lorentz parameters E_m, σ_m and Γ are the resonance energy, peak cross-section and full width at half maximum respectively. In the Goldhaber-Teller (GT) model, the associated transition density with the 100 % EWSR value for IVGDR are given by [49],

$$\delta\rho_1^n(r) = -\alpha_1 \frac{2Z}{A}\frac{d\rho_n}{dr} \qquad \delta\rho_1^p(r) = -\alpha_1 \frac{2N}{A}\frac{d\rho_p}{dr} \tag{2.32}$$

with the amplitude, α_1, given by,

$$\alpha_1^2 = \frac{\pi\hbar^2}{2m}\frac{A}{NZE_x} \tag{2.33}$$

The IVGDR contribution to the experimental differential cross-section is then determined as follows,

$$\frac{d\sigma^2}{d\Omega dE}(\theta_{c.m.}, E_x)_{\lambda=1,\mu=1} = a_{\lambda=1,\mu=1}(E_x)\ \frac{d\sigma^2}{d\Omega dE}(\theta_{c.m.}, E_x)^{calc}_{\lambda=1,\mu=1} \tag{2.34}$$

where, $a_{\lambda=1,\mu=1}(E_x)$ are defined as,

$$a_{\lambda=1,\mu=1}(E_x) = \frac{\sigma^{abs}}{\int \sigma^{abs}(E_x)dE_x} \tag{2.35}$$

Chapter 3
Experimental Overview and Data Reduction

3.1 Overview

This chapter discusses the experimental details of the (α,α') and (d,d') reactions used to study isoscalar giant resonances in nuclei. The discussion begins with the experimental requirements for the giant resonance studies, followed by the general experimental set-up used for the three experiments. The first part of this chapter concludes by providing the detailed specifications of each experiment.

The second part of the chapter describes in detail the data reduction process needed to obtain the background-free, accurately-calibrated, excitation energy spectra. The chapter concludes with the description of the procedure for extracting the experimental cross-section from these excitation spectra.

3.2 Experimental Setup

The experiments were performed at the Research Center for Nuclear Physics (RCNP), Osaka University, Japan. The cross-section of the giant monopole resonance, which is the focus of this work, is maximum at 0°. Thus the forward angle measurements, including 0°, are extremely important for our analysis. The high-resolution spectrometer at RCNP, Grand Raiden, was used in order to separate the main beam from the scattered beam at extremely forward angle measurements. This unique capability made RCNP an ideal choice for these experiments.

D.C. Patel, *A Study of the Isoscalar Giant Monopole Resonance*, Springer Theses,
DOI 10.1007/978-3-319-22207-3_3

3.2.1 Beam Line at RCNP

The accelerators at RCNP consists of two cyclotrons. The azimuthally varying field (AVF) cyclotron serves as injector into the K400 ring cyclotron, as shown in Fig. 3.1 [58]. A low energy beam is extracted from an electron cyclotron resonance (ECR) ion source and is injected in the AVF cyclotron [59]. The ring cyclotron was used in the single turn extraction mode in order to keep the beam halo to a minimum. The beam was then transported through the WS beam line to the experimental area. The achromatic beam transport was used in order to avoid an increase in the beam halo which could have resulted when using the high-resolution lateral-dispersion matching mode [60].

3.2.2 Grand Raiden Spectrometer

The beam, after its interaction with the target, was guided through the high resolution magnetic spectrometer, Grand Raiden. The main beam is guided through an exit beam pipe at the high-momentum side of the focal plane. The scattered particles were momentum analyzed with a resolution of $p/\triangle\ p\ =\ 37{,}000$ [61]. The schematic set up of the Grand Raiden is shown in Fig. 3.1. Grand Raiden has the configuration of QSQDMD(DSR), where Q, S, D, and M denote quadrupole, sextupole, dipole, and multipole magnets, respectively. An optional magnet, (DSR), is a dipole for spin rotation magnet which was used in our experiment as an extra steering magnet, for the 0° measurement, in order to guide the main beam into the Faraday cup (FC) located at the end of the beam exit pipe [62]. The complete system, shown in Fig. 3.1, was rotated about the center of the scattering chamber for the cross-section measurements at different angles [50, 63]. The main properties of the Grand Raiden spectrometer are listed in Table 3.1.

3.3 Detector Setup

3.3.1 Focal-Plane Detector System

The focal plane detector system consisted of two multiwire drift chambers (MWDCs) followed by two plastic scintillators (PS1 and PS2) as shown in Fig. 3.2 [64]. The detector system was aligned along the focal plane tilted at 45° with respect to the central ray of the spectrometer. The MWDCs have holes at their high-momentum sides of the sensitive area in order to allow for the main beam to pass through it for the 0° measurement. This enabled us to measure nuclear excitation energies at as low as 6 MeV in the case of 400 MeV alpha particles and about 8 MeV in the case of 200 MeV deuterons at 0°.

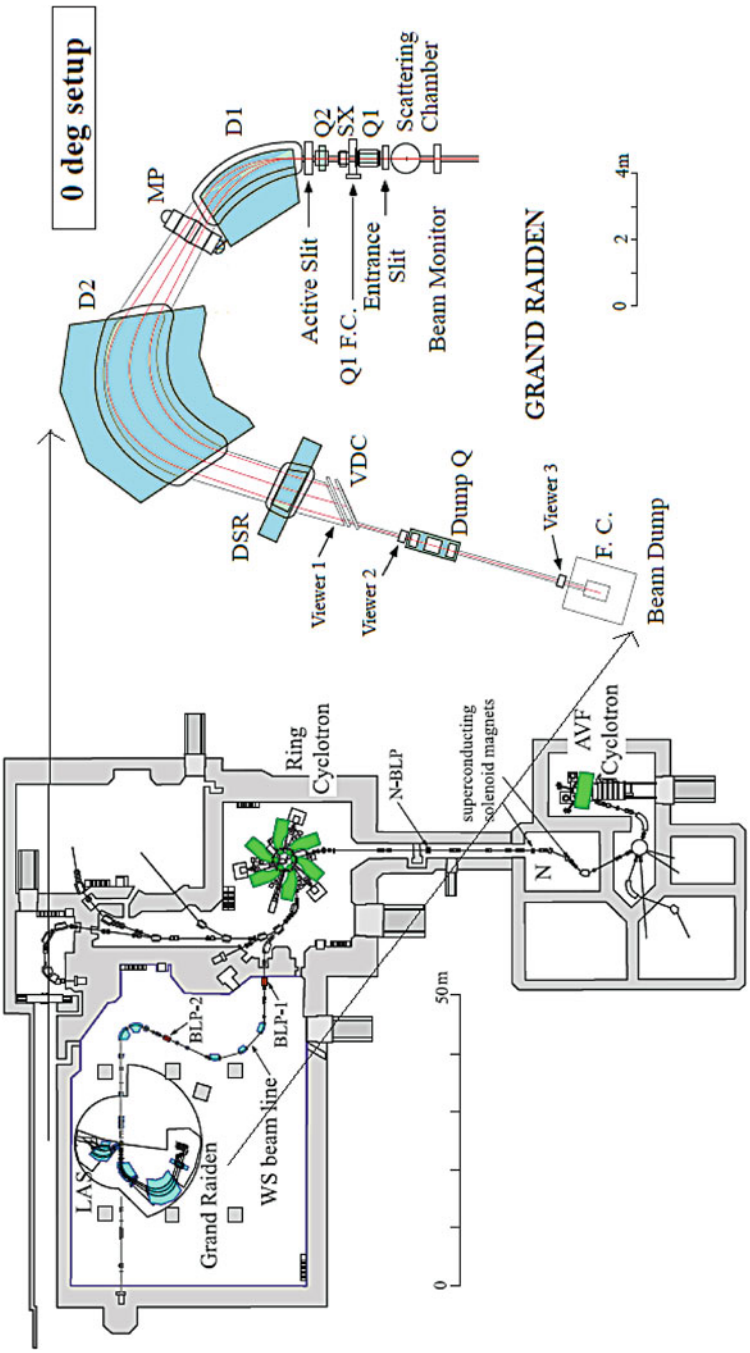

Fig. 3.1 RCNP beam line layout on the left side with the Grand Raiden setup for 0° measurement on the right side

Table 3.1 Design parameters of Grand Raiden and MWDC

Grand Raiden parameters		MWDC design parameters	
Radius of the central orbit	3 m	Active area	1150^{W} mm × 120^{H} mm
Total bending angle	162°	Wire configuration	X(0°), U(−48.2°)
Angular range	−4° to 90°	Anode-cathode gap	10 mm
Tilting angle of focal plane	45°	Anode wire spacing	2 mm
Max. magnetic field strength	18 kG	Sense wire spacing	6 mm (X), 4 mm (U)
Max. magnetic rigidity	5.4 T·m	Number of sense wires	192 (X), 208(U)
Momentum resolution (p/△p)	37,000	Anode sense wire	20 μm Au-W
Momentum acceptance	5 %	Anode potential wire	50 μm Au-Cu/Be
Momentum dispersion	15.451 m	Cathode foil	10 μm carbon-aramid
Max. horizontal acceptance	±20 mr	Gas seal	12.5 μm aramid film
Max. vertical acceptance	±70 mr	Pre-amplifier	LeCroy 2735DC
Horizontal magnification (x|x)	−0.417	Digitizer	LeCroy 3377 TDC
Vertical magnification (y|y)	5.98	–	–

Detailed parameters of the MWDCs are summarized in Table 3.1. Each MWDC consists of X and U anode planes with wire configurations as shown in Fig. 3.3. The X plane was held at −350 V while the U plane was held at −500 V. A high voltage of −5.4 kV was applied to the three cathode planes. The MWDCs were filled with a gas mixture of Ar (71.4 %) and iso-butane (28.6 %). Iso-propyl-alcohol was mixed at 2 °C vapor pressure into argon gas.

3.3.2 Faraday Cup Settings

The inelastic scattering measurements were performed over an angular range of 0° to about 12°. In order to reliably determine the accumulated charge of the incident beam, three different Faraday cups (FC) were used to cover the whole angular range.

1. FC for 0° measurement
   At 0° the main beam passes very close to the scattered beam and hence a special setup, as shown in Fig. 3.2, was used. The main beam was guided through the spectrometer to the beam exit pipe situated at the high-momentum side of the MWDCs. The main beam was stopped in a 0°-FC situated 3 m down stream of the focal plane.
2. FC for $2° < \theta_{Lab} < 5°$ measurement
   For $\theta_{Lab} > 2°$, the main beam does not pass through the spectrometer owing to the limited horizontal acceptance of the spectrometer. Therefore, for the $2° < \theta_{Lab} < 5°$ measurements, a special Faraday cup after quadrupole Q1 called Q1-FC was used. In this setup, the beam passes through the side-gap of the Q1 magnet and is stopped in a FC located between Q1 magnet and SX magnet 1.55 m behind the target.

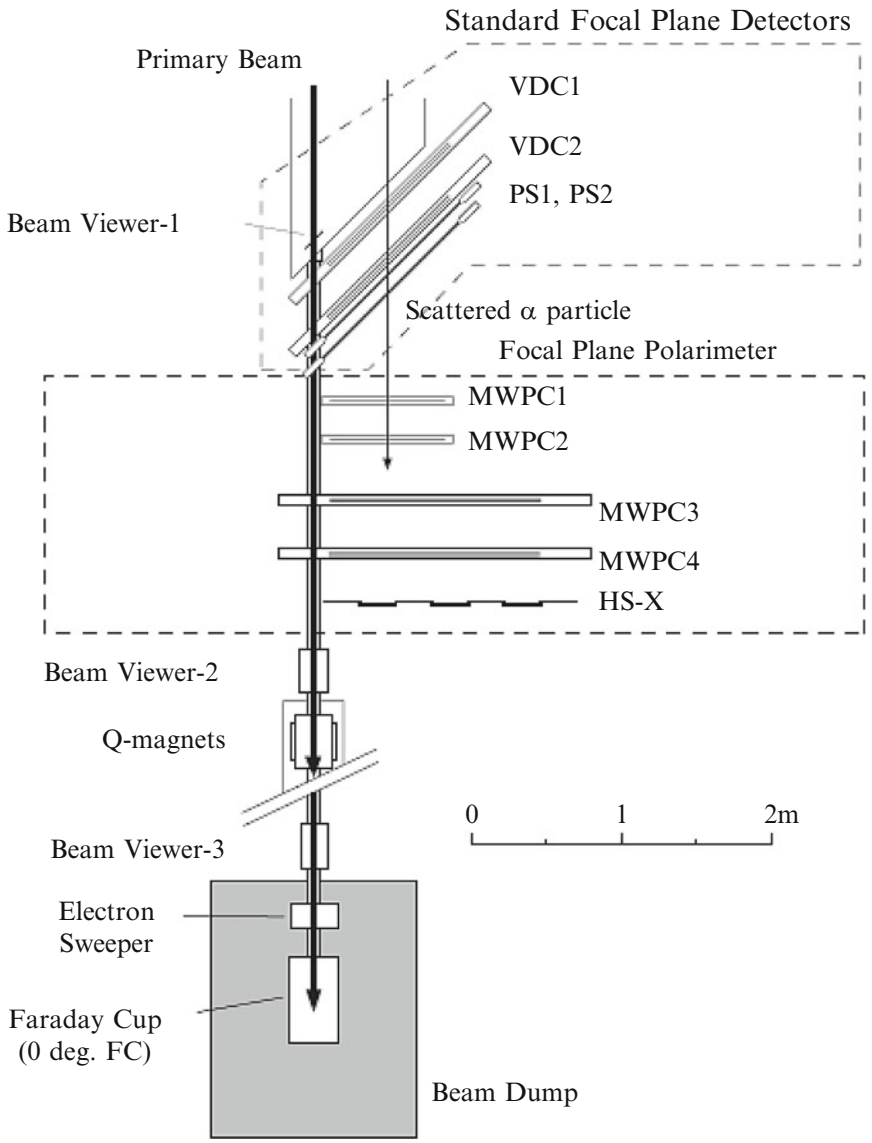

Fig. 3.2 Focal plane detector system shown in the setup for 0° measurement with the primary beam passing close by the high-momentum side

3. FC for $\theta_{Lab} > 6.5°$ measurement

For the measurements at $\theta_{Lab} > 6.5°$, the beam was stopped in the standard scattering chamber (SC) FC, situated inside the SC. The SC-FC is most reliable and stable against fluctuations of the beam intensity.

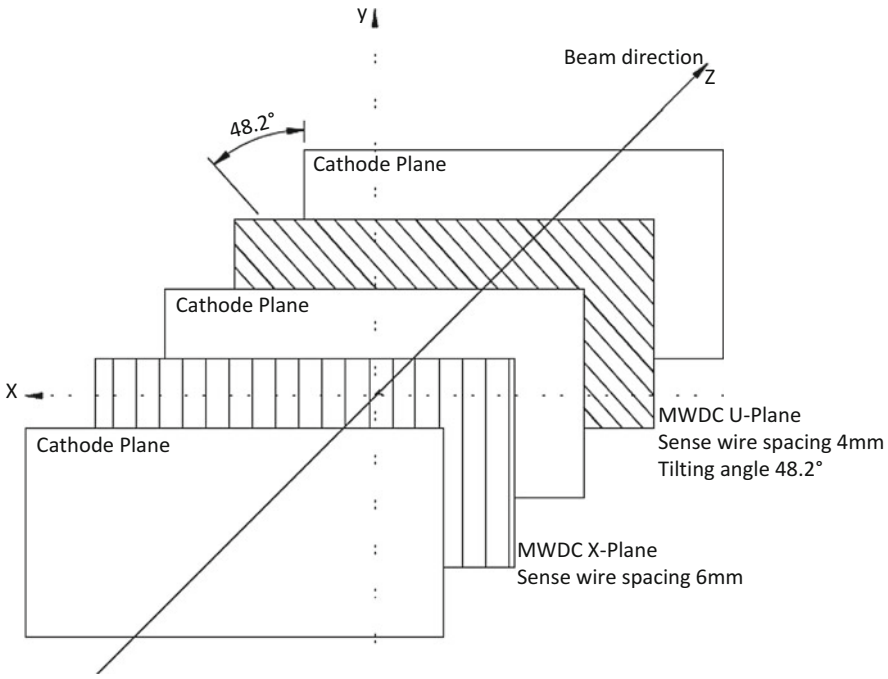

Fig. 3.3 Structure of each plane of MWDC

3.4 Data Acquisition System

The overview of the data acquisition system (DAQ) used for the high rate measurements is presented in Fig. 3.4 [65, 66]. Each event was constructed using drift-time data from the MWDCs (digitized by LeCroy3377 TDC), the charge and timing signals from the trigger scintillators encoded with LeCroy4300B Fast Encoding and Readout ADC (FERA) system and the input register.

The trigger signal was generated from the coincidence of signals from PS1 and PS2 using the trigger circuit shown in Fig. 3.5. The output signals from PS1 and PS2 were sent over two paths; one was discriminated by a constant fraction discriminator (CFD Ortec 935) and the other was sent to the FERA module after a delay. Further the CFD outputs were sent over two paths; one of the CFD outputs was transmitted to the TFC (time to FERA converter) backed by the FERA module and the other one was used to generate the coincidence signal using a mean-timer circuit (REPIC PRN-070) where the two signals from both sides of the same PS were averaged. The trigger system was constructed using a LeCroy 2366 universal logic module (ULM) with field programmable gate-array (FPGA) chips [67]. The trigger signals, after 250 ns delay, were utilized as a common-stop signals for LeCroy3377 TDCs and gate signals for FERA.

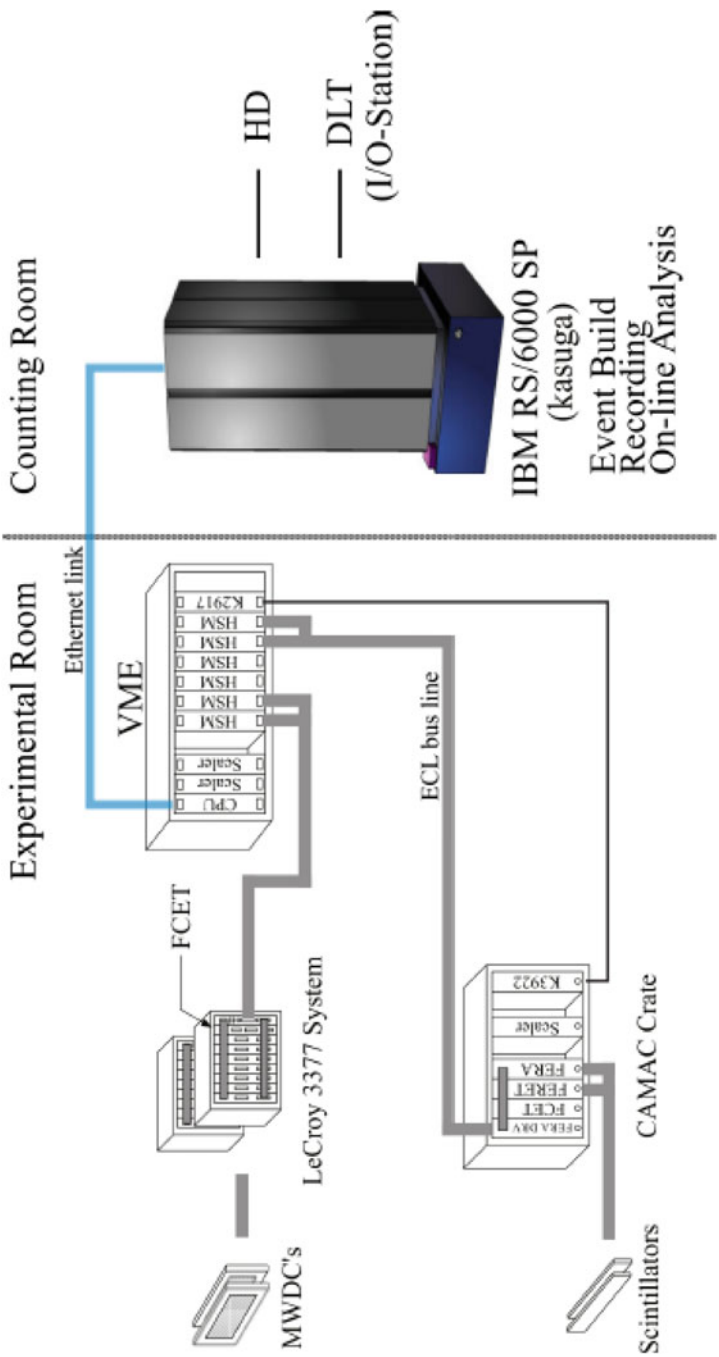

Fig. 3.4 An overview of the DAQ system

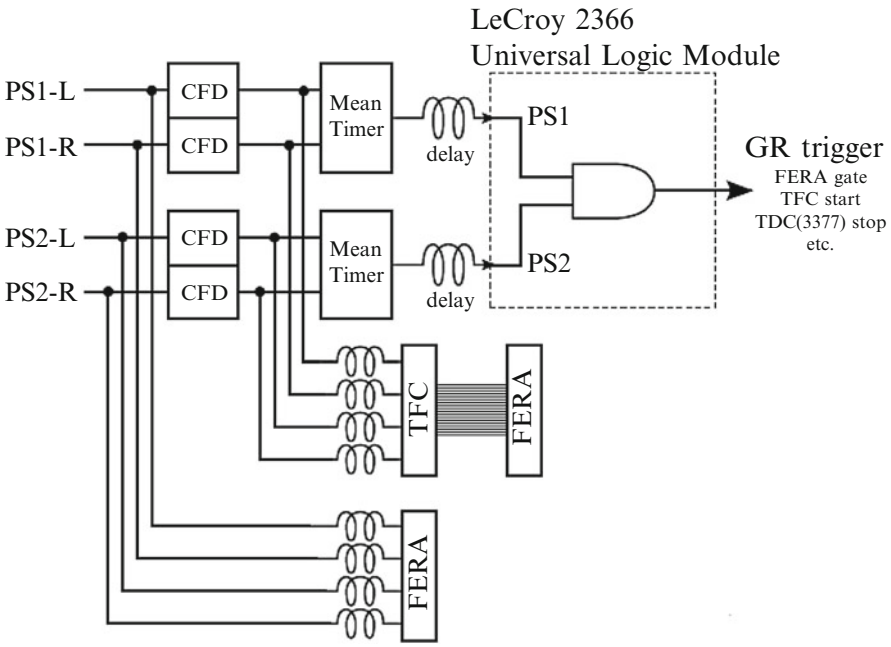

Fig. 3.5 Schematic diagram of the Trigger circuit

As a part of the DAQ system, flow controlling event tagger (FCET) was used to attach the event header, event number and the input register words to each event in order to maintain the consistency of the data flow [68]. The digitized data were transferred via the emitter coupled logic (ECL) line bus to high speed memory modules (HSM) in a Versa Module Europa (VME) system (LeCroy 1191 dual port memory) as shown in Fig. 3.4. Each data line was connected to a pair of HSMs which worked in a double-buffer mode. The timing of the buffer change was controlled by the LeCroy2366 ULM, Since the data readout was independent of the software management and computer automated measurement and control (CAMAC) functions, the effective dead time for encoding events was reduced to less than 30 μs/event. Finally the buffered data was transferred and stored in the work station server IBM RS/6000 SP via gigabit ethernet (GbE) link.

3.5 Experimental Specifications

This section presents the experimental specifications for the three experiments that form part of this thesis work. The first experiment (E-309) was performed using a 100 MeV/u $^{4}He^{++}$ beam to study the giant resonances in the even-even $^{106,110-116}Cd$ isotopes. The second experiment (E-340) was performed using a 100 MeV/u $^{4}He^{++}$

Table 3.2 Target specifications

E-309			E-340			E-318	
Target	Thickness (mg/cm^2)	Enrichment	Target	Thickness (mg/cm^2)	Enrichment	Target	Thickness (mg/cm^2)
^{106}Cd	4.99	96.0	^{204}Pb	5.16	99.94	^{24}Mg	50.0
^{110}Cd	5.01	95	^{206}Pb	4.92	99.76	^{28}Si	58.5
^{112}Cd	5.06	98	^{208}Pb	5.82	99.70	^{58}Ni	1.5
^{114}Cd	6.50	96	–	–	–	^{90}Zr	4.2
^{116}Cd	6.01	93	–	–	–	^{116}Sn	10.0
–	–	–	–	–	–	^{208}Pb	10.0
Calibration targets							
^{12}C	2.2	–	^{26}Mg	2.5	–	^{12}C	2.2

Table 3.3 Angular ranges

Expt.	Beam	Energy MeV	Energy res. keV	Elastic angular range	Inelastic angular range
E-309	$^{4}He^{++}$	386	∼160	$3.4° \leq \theta_{Lab} \leq 19.0°$	$0.0° \leq \theta_{Lab} \leq 9.8°$
E-340	$^{4}He^{++}$	386	∼160	$3.5° \leq \theta_{Lab} \leq 24.0°$	$0.0° \leq \theta_{Lab} \leq 9.5°$
E-318	$^{2}H^{+}$	196	∼120	$3.5° \leq \theta_{Lab} \leq 32.0°$	$0.0° \leq \theta_{Lab} \leq 11.0°$

beam to test the mutually enhanced magicity (MEM) effect on the giant resonances in the even-even $^{204-208}$Pb isotopes. The third experiment (E-318) was performed to establish the feasibility of studying giant resonance in various nuclei using a 100 MeV/u $^{2}H^{+}$ beam.

Elastic and inelastic scattering cross-sections were measured for the self-supporting targets in case of each experiment. The target thicknesses are summarized in Table 3.2. The beam energy, experimentally obtained energy resolution, and the angular range covered for each experiment are summarized in Table 3.3.

In the case of E-340, due to time constraints, the elastic scattering cross-sections for ^{208}Pb were measured over 3.5° to 8.5°, and the previous data from [50] (measured at the same beam energy) were used for angles up to 25°. In the case of E-318, inelastic scattering cross-sections for the giant resonance excitation region were measured only for ^{116}Sn and ^{208}Pb. The elastic scattering cross-sections were measured for all six targets in order to determine the optical model for deuteron scattering.

3.6 Data Reduction

The analyzer program, Yosoi analyzer, was mainly used for the data reduction process [69]. Following particle identification, the gated spectra were further analyzed for background reduction and energy calibration in order to reliably extract the corresponding cross-sections and, hence, the angular distributions.

3.6.1 Particle Identification

The timing and the pulse height information of the trigger signals from the scintillator counters, PS1 and PS2, were used to identify the charged particles. The charged particle loses energy in matter primarily by ionization and the corresponding rate of energy loss of the charged particle as it travels through the material is given by Bethe-Bloch formula as [70],

$$-\frac{dE}{dx} = 2\pi N_A r_e^2 m_e c^2 \rho \frac{Z}{A}\frac{z^2}{\beta^2}\left\{ln\left(\frac{2m_e v^2\gamma^2 W_{max}}{V^2}\right) - 2\beta^2 - \delta - 2\frac{C}{Z}\right\} \tag{3.1}$$

Here, W_{max} is the maximum energy that can be imparted to a free electron in a single collision, N_A is Avogadro's number, r_e is classical electron radius, m_e is electron mass, ρ is density of the medium, Z is atomic number of the medium, A is atomic mass number of the medium, z is charge of the incoming particle, v is velocity of the incoming particle, $\beta = v/c$ of the incoming particle, $\gamma = \frac{1}{\sqrt{1-\beta^2}}$, V is mean excitation potential, δ is density correction, C is shell correction to the total energy loss. Further, the energy loss of a charged particle is approximately proportional to the number of photons produced in the scintillators. The number of scintillation photons, produced at a distance x from the photo multiplier tube (PMT), are attenuated as they pass through the scintillator material. The number of photons entering one of the PMTs, I, can be described as a function of the distance x as,

$$I(x) = I_0 exp\left(-\frac{x}{l}\right) \tag{3.2}$$

where, I_0 is the initial photon number and l is the attenuation length of the scintillator material. If the source point is at a distance x from the left PMT, the geometric mean of the number of photons from the two PMTs, which are at a total distance of L from each other, is given by,

$$\bar{I} = \sqrt{I_L I_R} = \sqrt{I_0 exp\left(-\frac{x}{l}\right)\cdot I_0 exp\left(-\frac{L-x}{l}\right)} = I_0 exp\left(-\frac{L}{2l}\right) \tag{3.3}$$

The geometrical mean, thus, being independent of the position x of the source point of ionization, becomes a good measurement of the deposited energy. The $\bar{I}$ spectra are, therefore, very useful for particle identification (PID), as shown in Fig. 3.6. The threshold of the CFD and the HV for the scintillators are optimized to cut off the events due to low-energy scattered protons in order to improve the live time of the DAQ system. The bottom right panel of the plot shows a spectrum where clear identification can be made between alpha particles and protons. Gates applied to this spectrum help in selecting the particles of interest for further analysis.

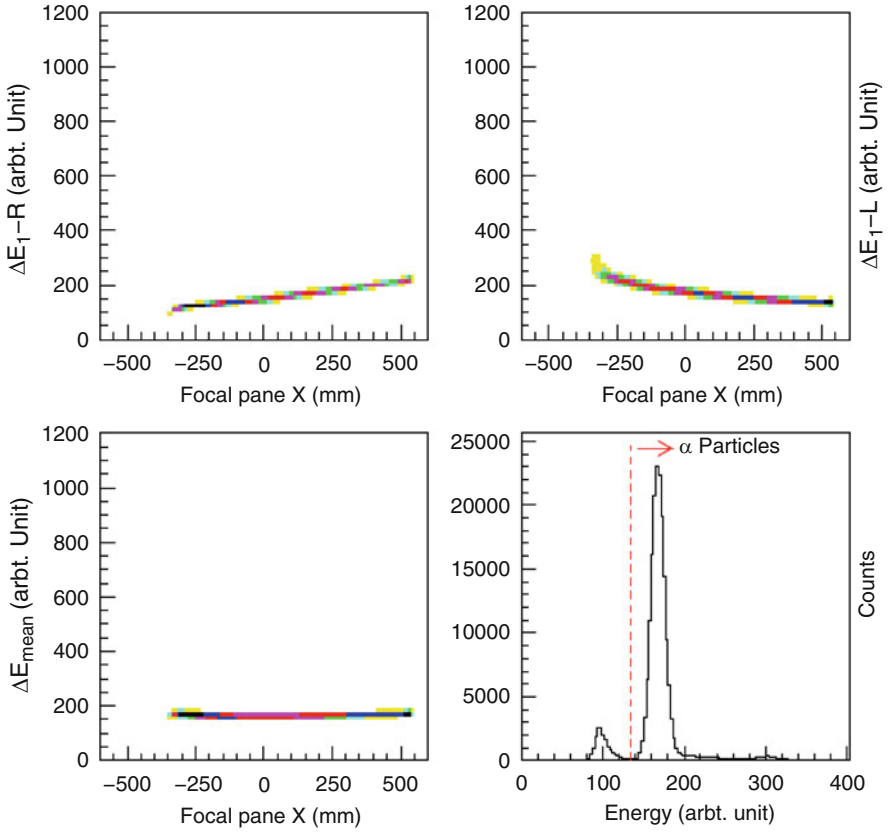

Fig. 3.6 Description of the particle identification technique. *Top left* and *right panel*: Correspond to the *right* and *left* PMT outputs. *Bottom left panel*: Corresponds to the geometrical mean of the left and the right PMT output as described by Eq. 3.3. *Bottom right panel*: Corresponds to the projection of *bottom left panel* on to the energy axis with counts on the y-axis

3.6.2 Particle Track Reconstruction

Three-dimensional particle track reconstruction can be achieved by making use of the signals from the MWDCs. This procedure is depicted in Fig. 3.7. The wire planes of the MWDCs are aligned parallel to the focal plane, i.e. 45° relative to the beam direction. A charged particle passing through the MWDC creates two or more wire hits per plane. The group of these adjacent hit-wires is called a "cluster". This allows for separating any background events created e.g. by X-rays or γ rays, which are usually single hit events. The track reconstruction is based on satisfying the following three conditions: (1) A cluster has at least two wire hits. (2) A single wire hit is ignored. (3) The number of clusters in each anode plane is one.

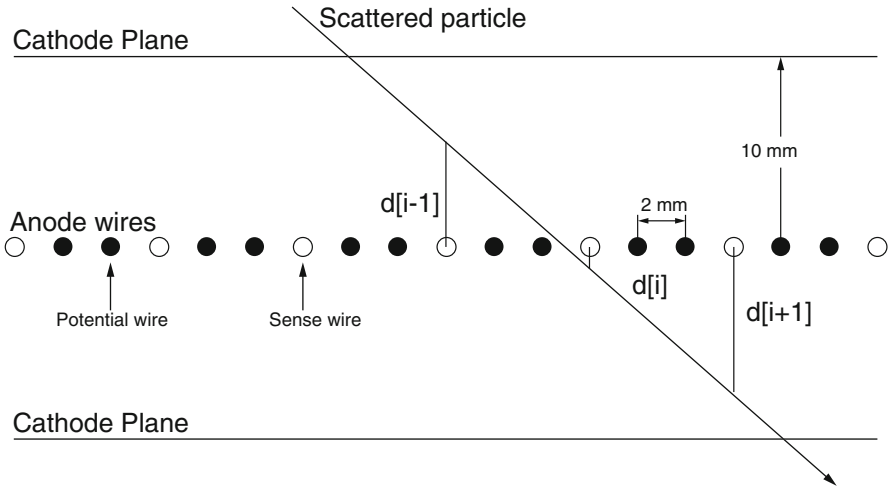

Fig. 3.7 Details of the x-plane configuration of the MWDC

A cluster with three wire hits is depicted in Fig. 3.7. The expected position, p, of the charged particle at an anode plane of the MWDCs is given by,

$$p = p_i + \Delta P \frac{d_{i-1} + d_{i+1}}{d_{i-1} - d_{i+1}} \tag{3.4}$$

Here, p_i is the position of the i-th anode wire and ΔP is the anode wire-spacing, for the geometrical setup where $d_{i-1} < 0$ and $d_{i-1} > 0$. The drift lengths d_i, d_{i+1} and d_{i-1} are obtained from the drift time information measured by the TDC. The free electrons, generated by the charged particles entering the MWDCs, drift in the electric field between the potential wires and the cathode plain generating a drift time spectrum as shown in Fig. 3.8. The edge closest to cathode foil corresponds to the longest drift length. The sharp peak at the edge near anode wire in the TDC spectrum is due to the steep 1/R dependence of the electric field close to the anode wire. Second order corrections were employed to obtain the flat distribution in terms of the drift length, as shown in the lower panel of Fig. 3.8.

The horizontal angle, θ_x, of a particle track is determined from the relative positions at the two X-planes, (x_1,x_2) and the distance L = 250 mm between them, as follows,

$$tan\theta_x = \frac{x_2 - x_1}{L} \tag{3.5}$$

The position resolution was about, $\Delta x_1 = \Delta x_2 = 0.3$ mm in FWHM. This corresponds to an energy resolution of about $29\,\text{keV/mm} * 0.3\,\text{mm} = 8.7\,\text{keV}$ at

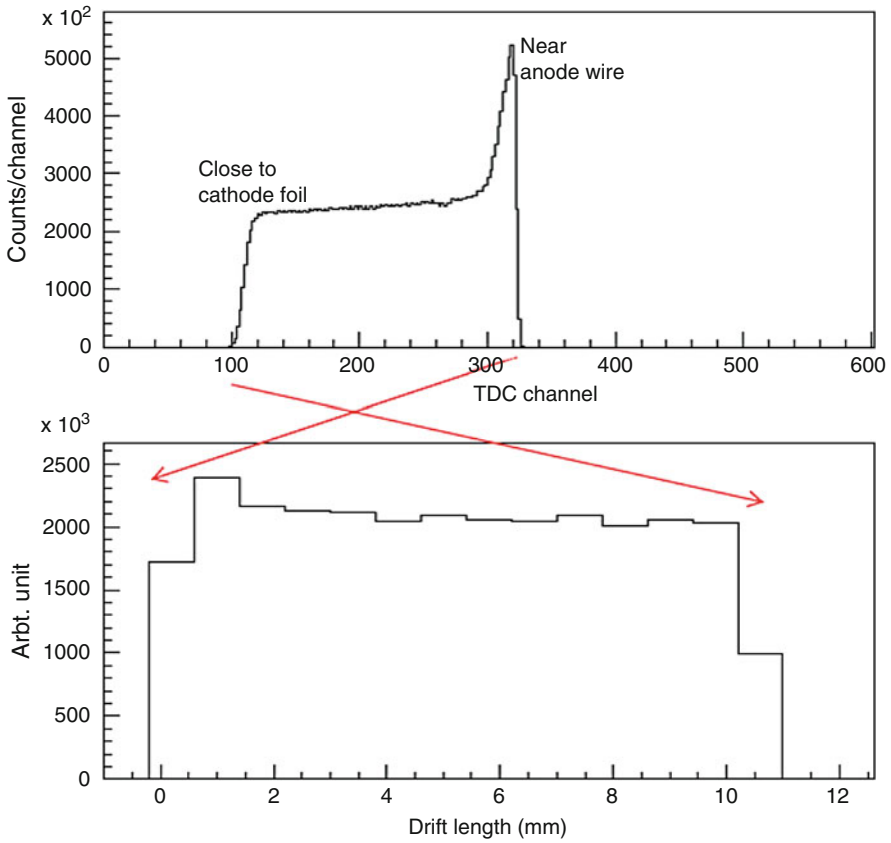

Fig. 3.8 Conversion of drift times to drift lengths for the track reconstruction with MWDCs

the focal plane of Grand Raiden which is better than the beam spread seen in each experiment. The horizontal angular resolution at the focal plane of Grand Raiden is given by,

$$\delta\theta_{fp} = tan^{-1}\left(\frac{\sqrt{2}\ 0.3}{250}\right) \approx 0.1^{\circ} \tag{3.6}$$

At the target, this corresponds to a horizontal scattering angle of, $\delta\theta_{tgt} \approx (\mathrm{x}|\mathrm{x}) * \delta\theta_{fp} \approx 0.417 * 0.1^{\circ} = 0.04^{\circ}$, since the horizontal angular magnification, $(\theta|\theta) \approx 1/(\mathrm{x}|\mathrm{x})$ at the focal plane where $(\mathrm{x}|\theta) \approx 0$. The measured angular resolution of the MWDCs, including the broadening of scattering angle due to the emittance of the beam and the multiple Coulomb-scattering effects, was about 0.15° at the focal plane of Grand Raiden.

3.6.3 Efficiency

Efficiency corrections are important to reliably extract the reaction cross-sections. There were two distinct efficiencies that were corrected for; the intrinsic efficiency of the MWDCs and the efficiency of the DAQ system. The tracking efficiency of each of the four anode-wire planes (two X-planes and two U-planes) was determined using the following description,

$$\epsilon_{Xi} = \frac{N_{Hit}(X_i \cap X_j \cap U_i \cap U_j)}{N_{Total}(X_j \cap U_i \cap U_j)} \tag{3.7}$$

Here the numerator is the number of hit events detected in all four anode-wire planes and the denominator is the total number of events detected by the other three anode-wire planes (baring the one for which the efficiency is calculated). The total MWDC efficiency is then the product of the all four anode-wire planes;

$$\in_{MWDC} = \epsilon_{X_i} \cdot \epsilon_{X_j} \cdot \epsilon_{U_i} \cdot \epsilon_{U_j} \tag{3.8}$$

The DAQ efficiency is calculated as follows,

$$\in_{DAQ} = \frac{\text{Trigger accepted events}}{\text{Requested events}} \tag{3.9}$$

The estimated total efficiency of both, the MWDC and DAQ, was found to be in the range of 90 % to 99 % for most runs.

3.6.4 Acceptance of Spectrometer

The tantalum slits used at the entrance of the Grand Raiden spectrometer determined the vertical and horizontal acceptances of the spectrometer. The aperture of the slits used in the experiments were ± 20 mrad wide horizontally. The horizontal angular acceptance was divided into three regions; $-0.9°$ to $-0.3°$, $-0.3°$ to $0.3°$ and $0.3°$ to $0.9°$, for all the finite angle measurements by using the reconstructed scattering angles as described in the previous section. The horizontal angular acceptance was restricted to $-0.6°$ to $0.6°$ for the $0°$ measurement. The geometrical description of the co-ordinate system used for the calculation of the solid angle is as shown in Fig. 3.9.

The solid angle is given by,

$$\Delta\Omega = \int\int d(cos\theta)d\phi = \int_{\theta_{GR}-\frac{\Delta\theta_x}{2}}^{\theta_{GR}+\frac{\Delta\theta_x}{2}} \int_{-\frac{\Delta\phi}{2}}^{+\frac{\Delta\phi}{2}} d\theta_x d\phi \tag{3.10}$$

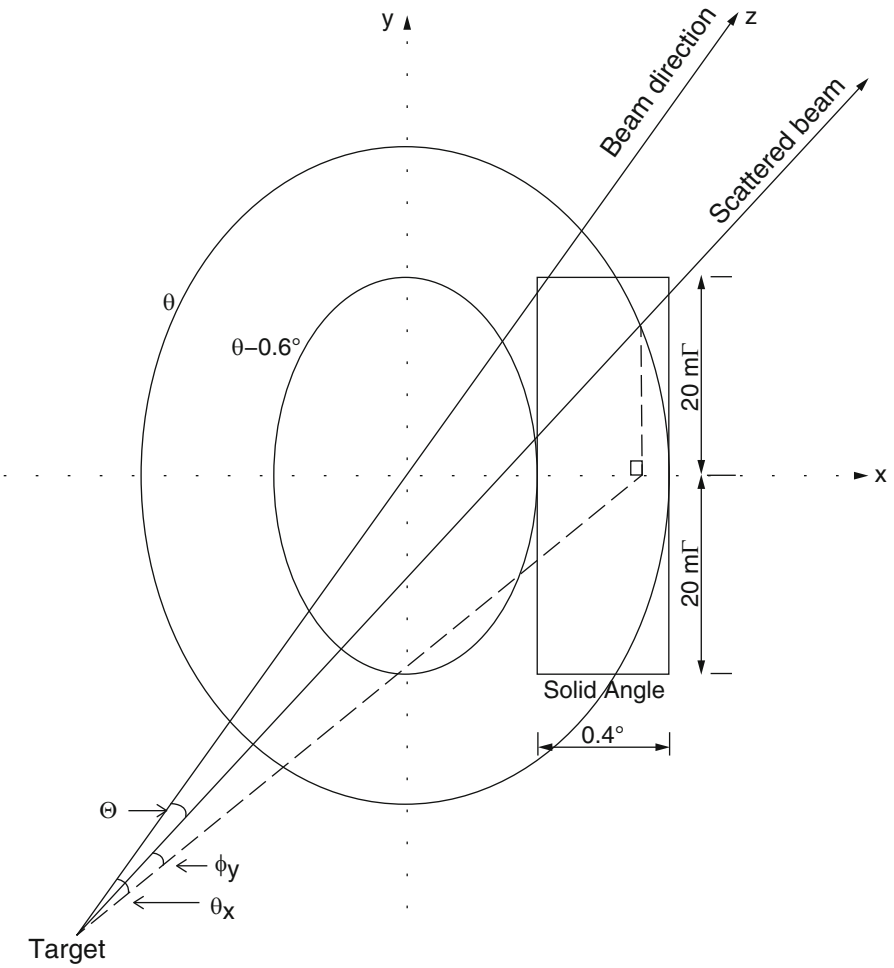

Fig. 3.9 Geometrical description of the co-ordinate system for the solid angle calculation

The average angle in the laboratory frame can be calculated according to Fig. 3.9 as follows,

$$\theta_{av} = \frac{\int_{\theta_{GR}-\frac{\Delta\theta_x}{2}}^{\theta_{GR}+\frac{\Delta\theta_x}{2}} \int_{\frac{-\Delta\phi_y}{2}}^{\frac{\Delta\phi_y}{2}} \Theta d\theta_x d\phi_y}{\int_{\theta_{GR}-\frac{\Delta\theta_x}{2}}^{\theta_{GR}+\frac{\Delta\theta_x}{2}} \int_{\frac{-\Delta\phi_y}{2}}^{\frac{\Delta\phi_y}{2}} d\theta_x d\phi_y} \tag{3.11}$$

$$\Theta = tan^{-1}\sqrt{tan^2\theta_x + tan^2\phi_y} \tag{3.12}$$

For the zero degree measurements, $\theta_{GR} = 0°$, the angular cut was $\Delta\theta_x = 1.2°$ ($-0.6°$ to $0.6°$) and $\Delta\phi_x = 40\,\text{mr}$ ($\pm 20\,\text{mr}$). Thus, the average angle in the laboratory frame corresponding to Grand Raiden angle of 0° is $\theta_{av} = 0.7°$.

3.6.5 Energy Calibration

Energy calibration is an important step in the analysis procedure. ^{12}C and ^{26}Mg were used as calibration targets in our experiments. In order to study the higher excitation energy region continuum, where there are no discrete states, it is required to calibrate the focal plane detector using the well-known low-lying discrete states in"standard" nuclei. Calibration was obtained using the kinematic relation between the incoming particles α/d, the target nucleus A, and the scattered particles α'/d' using the following equation,

$$E_x = \sqrt{(E_{\alpha/d} + M_A - E_{\alpha'/d'} - E_{loss})^2 - (P^2_{\alpha/d} + P^2_{\alpha'/d'} - 2P_{\alpha/d}P_{\alpha'/d'}Cos\theta_{lab})} - M_A \tag{3.13}$$

Here θ_{lab} is the scattering angle of the particle in the laboratory frame. The momentum of the scattered α particle was determined from the MWDC's data using the first order transfer matrix of Grand Raiden calculated along with the actual magnetic field settings using the code 'RAYTRACE' in conjunction with code 'calc_field' (M. Itoh, 2008, Private communication). The correction parameters of the higher order transfer matrix elements were obtained by comparing the calculated values with the experimental data of elastic and low-lying states of ^{12}C. A typical calibration spectrum so obtained is shown in Fig. 3.10.

In the E-340 experiment, the magnetic field setting required to cover the giant resonance excitation energy range in the Pb isotopes led to the 9.64 MeV peak of ^{12}C to being the lowest energy peak in the spectrum. This allows only for a linear calibration. In order to include non-linear terms, ^{26}Mg was used as a calibration target and the corresponding calibration spectrum is shown in Fig. 3.11. ^{26}Mg spectra were taken at three different magnetic field settings in order to calibrate the whole focal plane and determine the quadratic term in the calibration equation. The Bρ v/s focal plane x-position spectrum, constituting three magnetic field settings, is shown in the upper left panel of Fig. 3.11. The quadratic term obtained is of the order of 10^{-6}, confirming the validity of using linear calibration for the kind of energy resolutions obtained using achromatic, halo-free beams in our experiments.

3.6.6 Background Subtraction

All spectra obtained during the experiment contain background events arising from different sources in addition to the desired events. The background arising from the

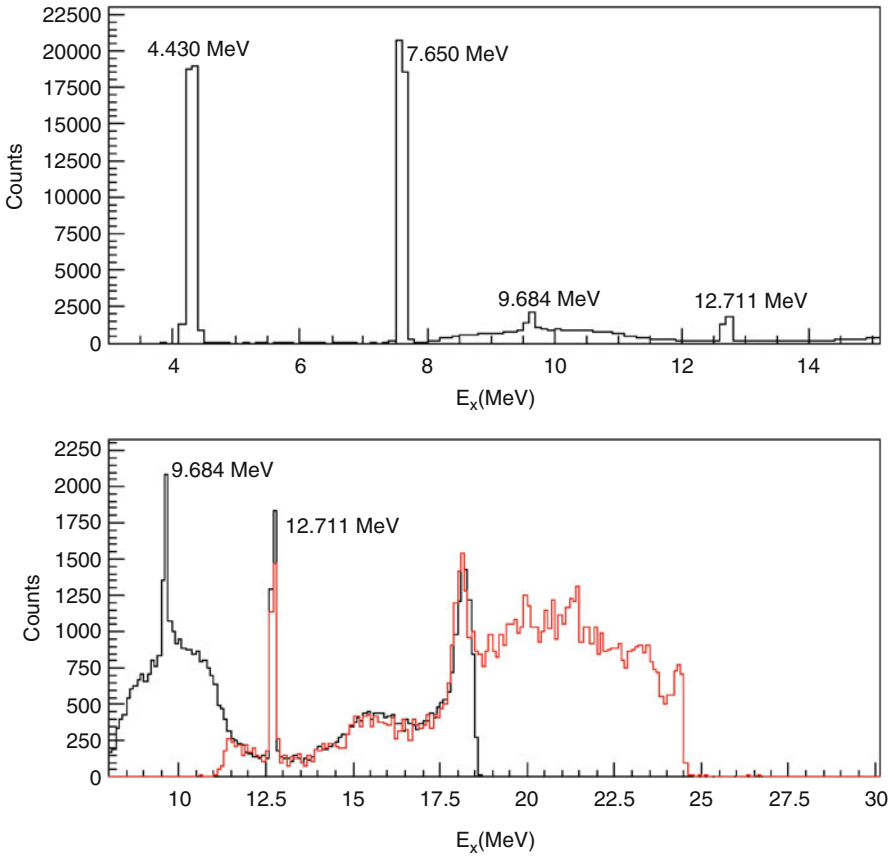

Fig. 3.10 The calibration using ^{12}C target at 0°. *Upper panel*: Calibration spectrum for the lower excitation energy states was taken at a particular magnetic field setting. *Lower panel*: The *black spectrum* is the zoomed-in section of the spectrum in the *upper panel*. The *red spectrum* is the calibration spectrum taken at a different magnetic field settings in order to cover the higher excitation energy region (scaled to the spectrum in *upper panel* of the figure, for comparison)

beam halo is reduced by tuning the accelerator and adjusting the slits. However, most background events originate from multiple coulomb scattering in the target and subsequent re-scattering from the edges of the entrance slit, the magnetic yokes and the walls of the spectrometer. The multiple coulomb scattering poses major problem in particular in forward angle measurements. In order to discriminate this background the Grand Raiden spectrometer was operated in the double focusing mode. While the 'true' events, from the inelastic scattering of the beam particles, are focused in vertical as well as horizontal direction, the background events result in a flat distribution as shown in the vertical Y-position spectrum in Fig. 3.12. The central peak region consist of the 'True + Background' events where the true events are focused in a sharp peak sitting on a flat background. Defining the gates on this

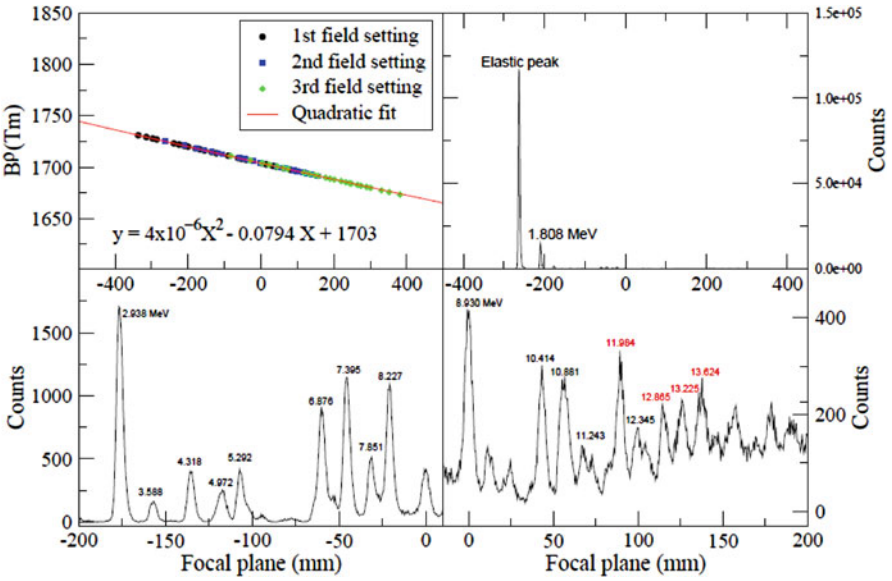

Fig. 3.11 Calibration using ^{26}Mg target at 5°. *Top left panel*: The calibration equation for the entire focal plane using three magnetic field setting data. The *red line* is the quadratic fit to the data points. *Top right panel*: The full spectrum obtained at 5°, showing the elastic and the first excited state of ^{26}Mg. *Bottom left panel*: The zoom in part of spectra b with identified peak energies. *Bottom right panel*: The higher excitation zoom of spectra b. The numbers in *red* represent the identified energies with large uncertainties

Y-position spectrum is translated to the excitation energy spectra as shown in the bottom left panel of Fig. 3.12. The resultant background subtracted spectrum, shown in the bottom right panel, is essentially free from instrumental background.

3.6.7 Differential Cross-Section

The instrumental background free spectrum of the scattered particles of interest, at a given angle, is used to calculate the differential cross-sections. The differential cross-section is defined as follows,

$$\frac{d^2\sigma}{d\Omega dE}(\theta_{av}, E_x) = \frac{Y}{N_I N_T \Delta E \Delta\Omega(\theta_{av}, E_x) \in_{MWDC} (\theta_{av}, E_x) \in_{DAQ} (\theta_{av}, E_x)} \tag{3.14}$$

where θ_{av} is the average scattering angle as defined in Sect. 3.6.4. Y is the yield in the accepted solid angle ($\Delta\Omega$, in msr), ΔE is the energy bin in MeV, and $\in_{MWDC,DAQ}$ are the total MWDC and DAQ efficiencies defined in Sect. 3.6.3. N_I is the total number of incident particles which depends on the integrated current of the incoming beam

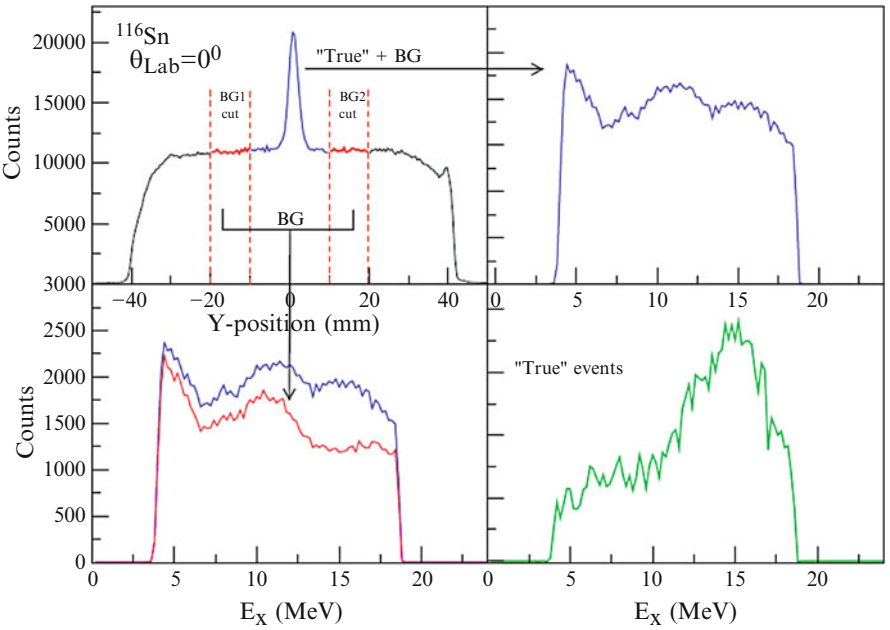

Fig. 3.12 Y-position and gated energy spectra at 0° for ^{116}Sn(d, d′)

Q, its atomic number Z, electron charge e. The total number of target nuclei, N_T, are determined from the target thickness Δx, Avogadro's number N_A and the mass of the target nucleus A. The differential cross-section equation then takes the following form,

$$\frac{d^2\sigma}{d\Omega dE}(\theta_{av}, E_x) = \frac{YAZe}{Q\Delta x N_A \Delta E \Delta\Omega(\theta_{av}, E_x) \in_{MWDC} (\theta_{av}, E_x) \in_{DAQ} (\theta_{av}, E_x)} \tag{3.15}$$

The elastic differential cross-section so obtained are further analyzed for determining the optical model parameters which are used in subsequent analysis of the inelastic scattering angular distributions.

Chapter 4
Data Analysis

4.1 Overview

The elastic angular distributions along with the first few discrete level angular distributions were utilized in modeling the nuclear potential. Details of the nuclear potential models are presented in the first two sections of this chapter followed by the detailed description of the models used in each of the three experiments. This chapter ends with the description of the multipole decomposition analysis (MDA) technique used for the analysis of the giant resonance data.

4.2 Optical Model

The optical model is one of the most successful models used to describe the scattering phenomenon [71]. The optical model essentially characterizes the interaction between two nuclei in terms of a potential. The optical potential is a simple "effective" interaction which is designed to describe the elastic as well as the inelastic scattering channels. It is used to replace the complicated many-body problem posed by the interaction between two nuclei with a much simpler problem of two particles interacting through an 'effective' potential. In order to take into account the inelastic channels, a complex optical model potential is adopted. This is closely related to the use of complex refractive index for describing the passage of light through a given medium. The details of this modeling procedure are described in the following section. The optical model plays an important role in the description of nuclear scattering. Not only does it provide an interpretation of the elastic scattering in terms of a potential, but it also provides the associated wavefunction which could be used to study the inelastic scattering.

D.C. Patel, *A Study of the Isoscalar Giant Monopole Resonance*, Springer Theses,
DOI 10.1007/978-3-319-22207-3_4

4.2.1 Introduction

In order to accurately describe the scattering phenomenon, each term in the complex optical potential can be further modeled based on the reaction under study. Each part of the potential, real and imaginary, can have contributions arising from various possible functional forms based on the modeling of a given reaction. Usually it is assumed [47], at least for light ion scattering, that the interior of the real part of the potential is flat and attractive (negative) and, because of the short range of the nuclear interaction, rises quickly and monotonically to zero at the surface. There are several analytical forms that can be used [72, 73]. In the present experimental investigation, a hybrid optical model potential was employed to model the 100 MeV/u α elastic scattering (E-309 and E-340). In the case of E-318, a phenomenological optical model was used to model the deuteron elastic scattering. These are discussed in further detail in the following subsections.

4.2.1.1 Hybrid Model

The hybrid optical model potential, which has been well established in previous studies of α scattering at similar beam energies [74, 75], was constructed using the density dependent single folding model for the real part of the potential and the Woods-Saxon form for the imaginary part. The form factors for the density dependent single folding real part were obtained using a Gaussian α-nucleon potential described by Satchler and Khoa [74]. The hybrid optical potential form is given by,

$$U = V_C + V_{DDG} + iW_{Vol} \tag{4.1}$$

Where,

$$V_{DDG}(s,\rho) = -V_G(s)f(\rho) = -V_R[1 - \alpha\rho_{gs}(r')^{\beta}]exp(-s^2/t^2)$$

and,

$$W_{Vol} = \frac{W_i}{1 + exp((r - R_i)/A_i)}$$

Here, $s = |r\text{-}r'|$ is the distance between the center of mass of the alpha particle and a target nucleon, $\rho_{gs}(r')$ is the ground-state density of the target nucleus at the position r' of the target nucleon, V_R and W_i are the potential depths for the real and the imaginary part of the potential, range $t = 1.88$ fm, $\alpha = 1.9$, $\beta = 2/3$ and, R_i and A_i are the radius parameter and diffusivity of the imaginary part of the potential.

Table 4.1 Fermi density distribution parameters used for the density dependent single folding calculations

	E-309			E-340		
	^{106}Cd	^{110}Cd	^{116}Cd	^{204}Pb	^{206}Pb	^{208}Pb
ρ_0 (fm^{-3})	0.1561	0.1573	0.1596	0.1583	0.1589	0.1594
c (fm)	5.2875	5.3435	5.4164	6.6169	6.6311	6.6468
a (fm)	0.523	0.523	0.523	0.523	0.523	0.523

V_C is the coulomb potential assumed to be of the form "point and uniform sphere" as described below,

$$V_C = \frac{+Z_p Z_t e^2}{r} : r \geq R_C$$
$$V_C = \frac{+Z_p Z_t e^2 \left[3 - \left(\frac{r}{R_C}\right)^2\right]}{2R_C} : r < R_C \tag{4.2}$$

Here R_C is the coulomb radius. The Fermi parameters c (half density radius) and a (diffuseness parameter) of the ground-state density used in the calculation are summarized in Table 4.1 [76].

Computer programs, SDOLF and DOLF, were used to calculate the real part of the elastic and transition potentials (L. Rickersten, 1976, SDOLF and DOLFIN, unpublished). The form factors for the real part of the potential were given as an input to the computer code PTOLEMY [77]. PTOLEMY input file was generated taking into account the correct relativistic kinematics. This program was used to fit the elastic scattering cross-sections in order to extract the OMPs; viz. V_R, W_i, R_i ($R_i = r_{i0}A^{1/3}$) and A_i, using χ^2 minimization technique. The values obtained for the even-even $^{106,110-116}$Cd isotopes (E-309) and $^{204-208}$Pb isotopes (E-340) are given in Table 4.2. In the case of the E-309, elastic data was obtained only for ^{106,110,116}Cd isotopes and the OMPs for ^{112,114}Cd were interpolated. The experimentally obtained first excited state cross-sections were compared with the calculated cross-section from PTOLEMY using the known B(E2)/B(E3) values from literature [78, 79]. These were used as a test to validate the OMP set obtained from the elastic fits. The elastic fits along with the 1st excited state comparison plots, for the Cd and Pb targets, are shown in Figs. 4.1 and 4.2 respectively. In the case of ^{208}Pb, the experimental elastic and 3_1^- state cross-sections were obtained form the previous data taken using α scattering at same beam energy [50]. The experimental 2_1^+ and 3_1^- angular distributions compare very well with the DWBA angular distributions calculated using the OMP obtained from the corresponding elastic fits and the adopted values of B(E2) and B(E3). Further, a global test was performed as a last check on the OMP as is discussed in the latter part of this chapter in Sect. 4.3.

Table 4.2 Hybrid model: optical model parameters obtained from fitting the experimentally obtained elastic angular distributions

E-309					E-340				
Target	V_R (MeV)	W_i (MeV)	r_{i0} (fm)	A_i (fm)	Target	V_R (MeV)	W_i (MeV)	r_{i0} (fm)	A_i (fm)
^{106}Cd	32.04	31.28	1.025	0.566	^{204}Pb	43.60	34.52	1.086	0.745
^{110}Cd	31.76	32.41	1.010	0.613	^{206}Pb	44.29	39.57	1.073	0.745
^{112}Cd	31.74	32.96	1.008	0.629	^{208}Pb	41.29	48.40	1.035	0.745
^{114}Cd	31.69	34.06	1.003	0.661					
^{116}Cd	31.67	34.61	1.000	0.677					

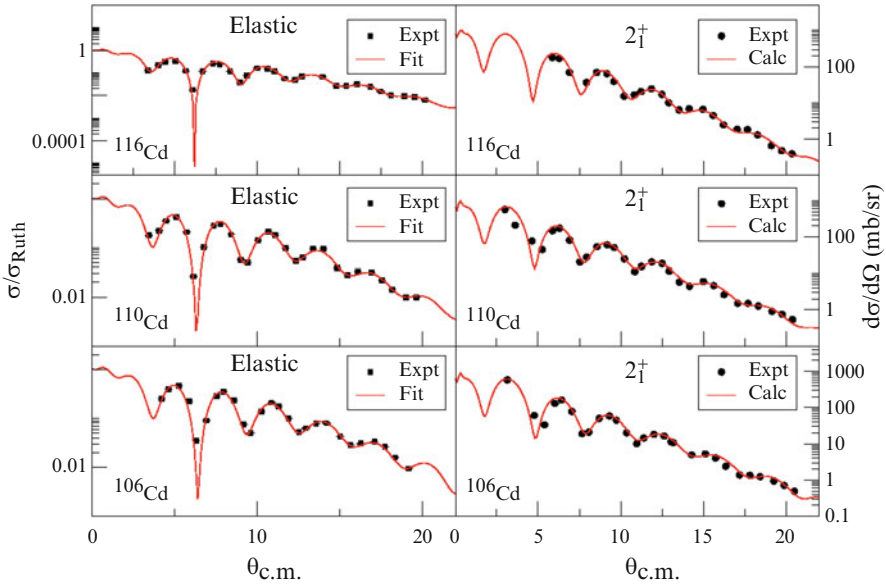

Fig. 4.1 E-309: Elastic and first excited state cross-section spectra obtained for ^{106,110,116}Cd isotopes. The *black squares* and *circles* correspond to the experimentally obtained angular distributions obtained for the elastic and the first excited state respectively. *Red lines* for the elastic state angular distributions are the fits to the experimental data. The *red lines* for the first excited state represent the calculated angular distribution obtained using the OMPs from the corresponding elastic fits and the known B(E2) values from literature

4.2.1.2 Phenomenological Potential Model

The customary optical model used for deuteron scattering consists of a complex central potential of the Wood-Saxon shape and its derivatives, a spin-orbit term of the Thomas form and a Coulomb term. These are described in further detail in Refs. [80–83]. Deuteron carries one unit of spin in its ground state. This requires inclusion of a real spin-orbit term in the optical potential. In addition to this, an

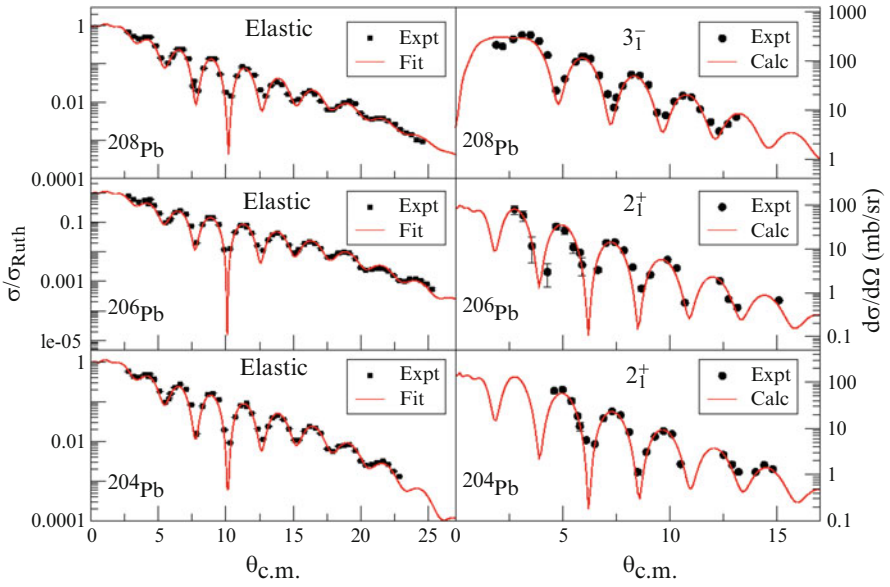

Fig. 4.2 E-340: Elastic and first excited state cross-section spectra obtained for ^{204,206,208}Pb isotopes. The *black squares* and *circles* correspond to the experimentally obtained angular distributions for the elastic and the first excited state respectively. *Red lines* for the elastic state angular distributions are the fits to the experimental data. The *red lines* for the first excited state represent the calculated angular distribution obtained using the OMPs from the corresponding elastic fits and the known B(E2)/B(E3) values from the literature

imaginary surface term is also required to account for the surface absorption. Thus, the phenomenological optical model potential employed in the current study had the following functional form,

$$V = V_{Coul} + V_{VOL} + i[W_{VOL} + W_{SURF}] + V_{LS} \tag{4.3}$$

where,

$$V_{VOL} = -V_{vol} f_v(r, R_v, a_v),\ W_{VOL} = -W_{vol} f_{wv}(r, R_{wv}, a_{wv}),$$

$$W_{SURF} = 4a_{ws} W_{surf} \frac{d}{dr} f_{ws}(r, R_{ws}, a_{ws}),$$

$$V_{LS} = V_{ls} \left(\frac{\hbar}{m_\pi c}\right)^2 \frac{1}{r} (\vec{L} \cdot \vec{S}) \frac{d}{dr} f_{ls}(r, R_{ls}, a_{ls}),$$

The computer code DFPD4 was used to calculate the folded Coulomb part of the optical potential [84]. The functional form of "f" was chosen to be of the Woods-Saxon form,

$$f(r, R, a) = \frac{1}{1 + e^{\frac{(r-R)}{a}}} \tag{4.4}$$

The Coulomb transition potential is calculated in the same way as the nuclear transition potential by the folding model in which the proton density of the target nucleus is used. Further, spin-orbit transition potentials were obtained using the same deformation parameters as for volume and surface potentials.

^{116}Sn and ^{90}Zr were used as test cases for establishing the model appropriateness since the OMP test could be performed on two low lying states viz. 2_1^+ and 3_1^- simultaneously in each nucleus thereby constraining the model better. The resultant best fits with this model for ^{116}Sn and ^{90}Zr nuclei are shown in Fig. 4.3. The elastic angular distribution fits and the DWBA calculations were done using computer code ECIS97 [2, 85]. The experimental 2_1^+ angular distributions for both nuclei compare very well with the calculated angular distributions using the adopted B(E2) values [78]. The 3_1^- experimental angular distribution for ^{116}Sn agrees very well with the calculated 3_1^- distribution with the adopted value of B(E3) from Ref. [79] within errors. For the case of ^{90}Zr the adopted value of B(E3) = 0.098 e^2b^3 overestimated the experimentally observed angular distribution. Instead, a lower value of

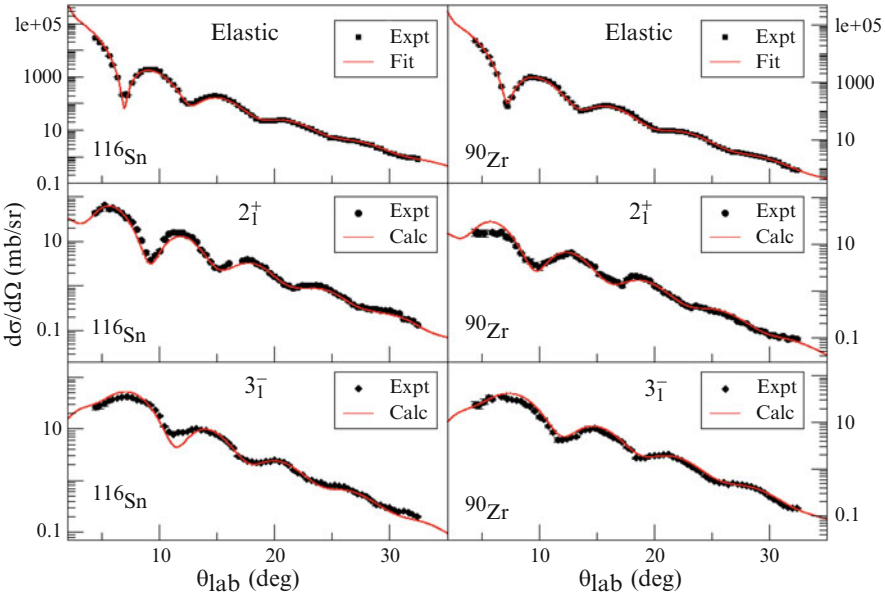

Fig. 4.3 E-318: Elastic and lowlying excited state cross-section spectra obtained for ^{116}Sn and ^{90}Zr. The *solid data points* correspond to the experimental data obtained for the elastic, 2_1^+ and 3_1^- states. *Red line* for the elastic state angular distributions is the best fit to the experimental data. The *red lines* for the excited states represent the calculated angular distributions obtained using the OMPs from the corresponding elastic fit and the known B(E2)/B(E3) values from the literature

Table 4.3 Phenomenological model: optical model parameters obtained from fitting the experimentally obtained elastic angular distributions

E-318										
Target	V_{vol} MeV	a_v fm	W_{vol} MeV	r_{0wv} fm	a_{wv} fm	W_{surf} MeV	r_{0ws} fm	a_{ws} fm	r_{0ls} fm	a_{ls} fm
^{208}Pb	48.54	0.938	20.59	1.20	0.361	7.0	1.24	0.79	1.12	1.23
^{116}Sn	44.33	0.911	20.87	1.07	0.571	7.0	1.12	1.09	0.93	1.11
^{90}Zr	42.95	0.997	20.20	1.06	0.538	7.9	1.10	0.997	1.20	0.985
^{58}Ni	39.07	0.914	21.41	1.07	0.456	7.6	1.04	1.03	1.19	1.11
^{28}Si	35.58	0.911	22.67	1.07	0.420	7.95	1.02	0.989	1.19	1.11
^{24}Mg	34.42	0.977	26.39	1.07	0.551	8.0	1.02	0.920	0.956	1.364

B(E3)= 0.043 e^2b^3 obtained from previous inelastic scattering data listed in Ref. [79] was used to reproduce the experimentally observed angular distribution.

Deuteron elastic scattering data was obtained for six different target nuclei. Some of the less sensitive parameters were held constant in order to reduce the number of free parameters and thence reduce the ambiguity in the parameter sets. Two parameters, $r_{0v} = 1.18$ fm and $V_{ls} = 2.11$ MeV, were held fixed in the fits. OMP extracted for all the nuclei studied in this experiment, corresponding to the simultaneous best reproduction of first excited state angular distribution, are summarized in Table 4.3.

The fits obtained using these parameter sets are plotted in Fig. 4.4. The fits tend to get worse for lighter nuclei. This is an implication of the failure of the pure phenomenological model for light mass nuclei. Similar limitation of the phenomenological model in the case of light nuclei is also noted in Refs. [81, 86]. However, this model works very well for the heavier nuclei like ^{116}Sn and ^{208}Pb. This model was employed further to test the global validity of the OMP set before the MDA.

4.3 Global Optical Model Analysis

The ratio of volume integral of an optical potential to the product of the projectile and target mass, $J_{R(I)}/(A_pA_t)$, has been found to be a suitable parameter for investigating the systematic trend of the optical model potentials [87, 88]. It is possible to refer to data that typically covers incident energy from 20 MeV to 1000 MeV. The comparison with this data, results in an important consistency test for the optical potentials obtained in a given experiment. The volume integrals are defined as,

$$J_{R(I)} = \int U_{R(I)}(r) d^3r \tag{4.5}$$

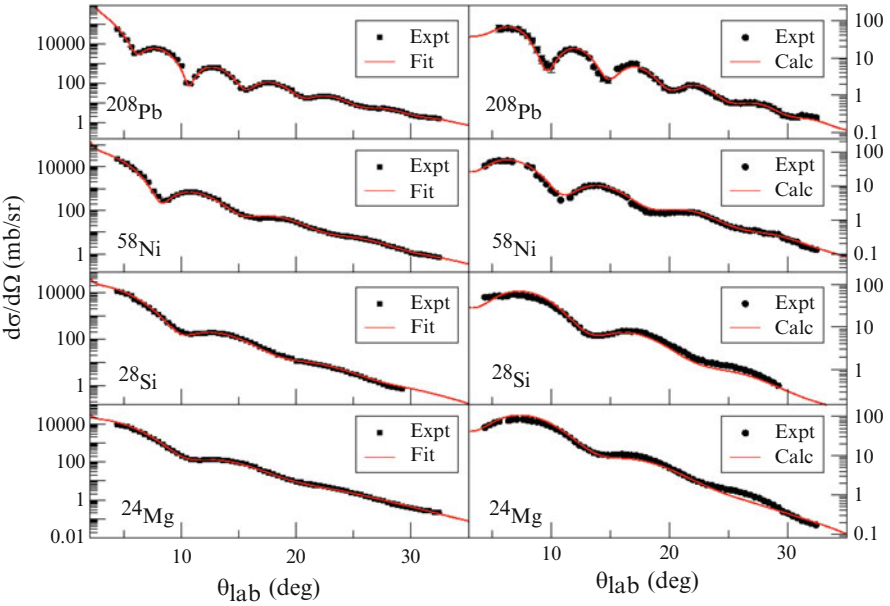

Fig. 4.4 E-318: Elastic and lowlying excited state cross-section spectra obtained for ^{208}Pb, ^{58}Ni, ^{28}Si and ^{24}Mg. The *solid data points* correspond to the experimental data obtained for the elastic and 2_1^+ state. *Red line* for the elastic state angular distributions is the best fit to the experimental data. The *red lines* for the excited states represent the calculated angular distributions obtained using the OMPs from the corresponding elastic fit and the known B(E2)/B(E3)(to within 20 %) values from the literature

Figure 4.5 shows the comparison of volume integrals obtained from previous work against those obtained from this work. The squares represent data obtained from α scattering and circles represent data obtained from deuteron scattering. The compilation data was obtained from previous experimental observations, as described in Refs. [24, 27, 81, 89–94]. All the current values, for both the real and imaginary volume integrals, follow the general trend as seen in the figure. The real part of the volume integral appear to show a decrease with energy, whereas, the imaginary part appears to be nearly constant. Within the scattered data set, the values obtained from the current analysis are quite reasonable, indicating the appropriateness of our optical model parameterizations.

4.4 Multipole Decomposition Analysis

The inelastic scattering cross-section spectra obtained at higher excitation energy consist of overlapping contributions from varied angular momentum transfers. It thus becomes important to extract the contribution from each of these multipolarities

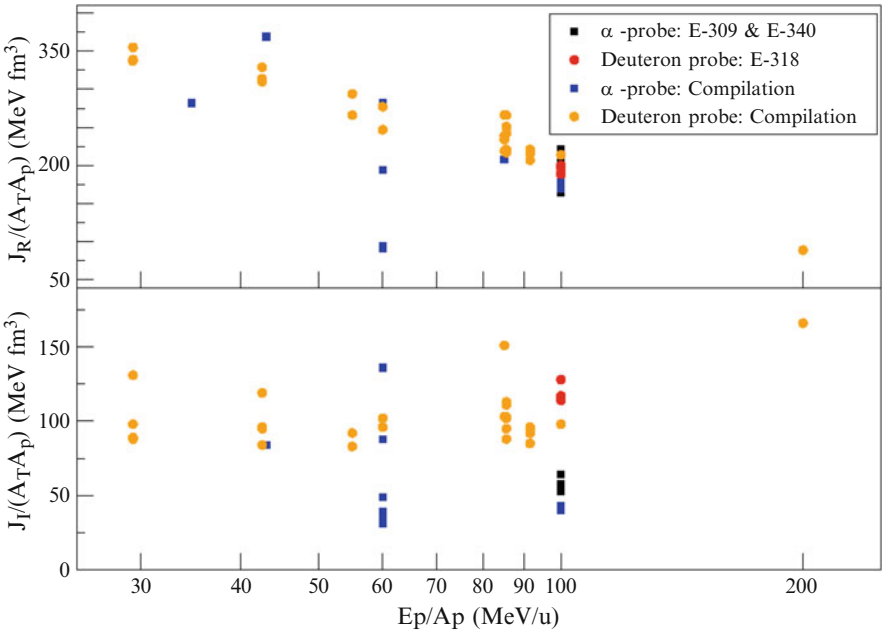

Fig. 4.5 Real and imaginary volume integrals for the central part of the optical potential. Data points in *square* are those obtained from α scattering experiments while the *circles* represents data points obtained from the deuteron scattering experiments. *Black* and the *red data points* are from the experiments performed towards this thesis work

in order to study the specific nuclear vibrational modes of interest. This section describes in detail the multipole decomposition technique used to separate strengths corresponding to each multipolarity.

4.4.1 Introduction

The OMP sets obtained from the analysis of the elastic scattering cross-sections are used to calculate the DWBA cross-sections. These calculations are carried out in the giant resonance excitation energy region and for various multipoles corresponding to different angular momenta transferred during the reaction. Calculations were performed with the help of PTOLEMY and ECIS codes using the transition densities and sum rules for various multipolarities described in Chap. 2.

The 0° inelastic scattering cross-sections measured for all the isotopes studied in this work are presented in Figs. 4.6, 4.7 and 4.8. Similar spectra were obtained for a number of angles over the angular ranges listed in Table 3.3. Each spectrum is divided into 1 MeV wide bins for further analysis, providing an "experimental" angular distribution for each energy bin. The contribution due to IVGDR, arising

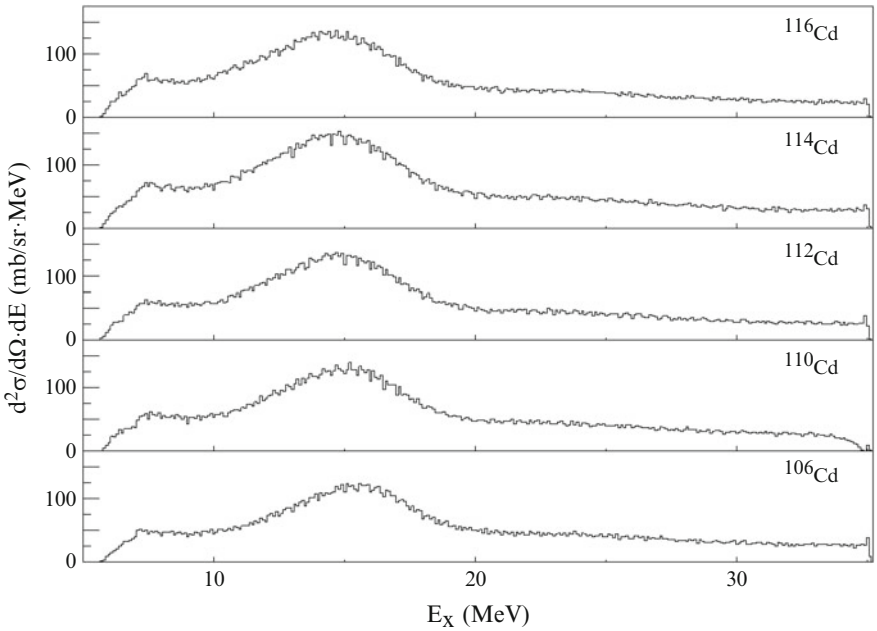

Fig. 4.6 E-309: (α,α') cross-section spectra (100 keV bin size) obtained for the even-even $^{106,110-116}$Cd isotopes at $\theta_{av} = 0.7°$

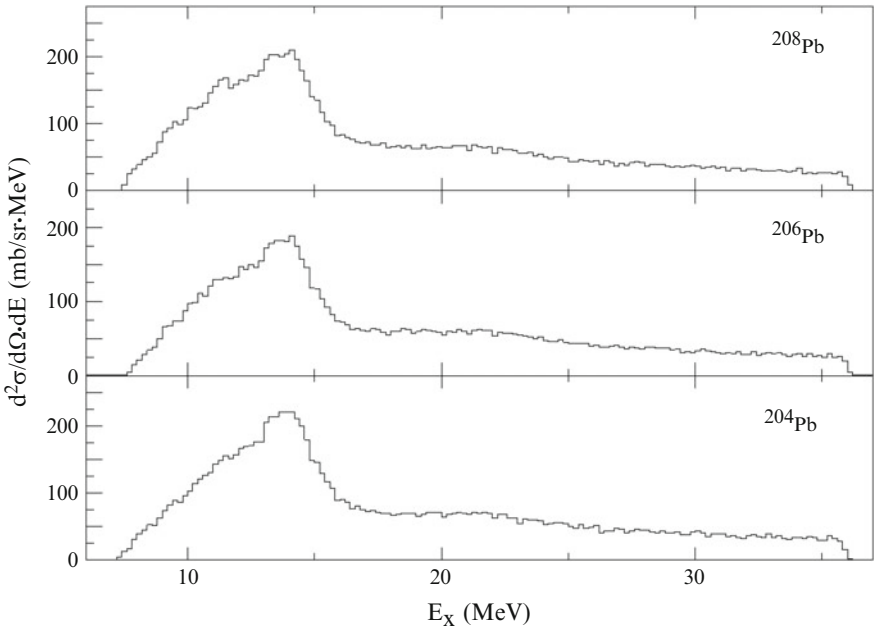

Fig. 4.7 E-340 : (α,α') cross-section spectra (200 keV bin size) obtained for the even-even $^{204-208}$Pb isotopes at $\theta_{av} = 0.7°$

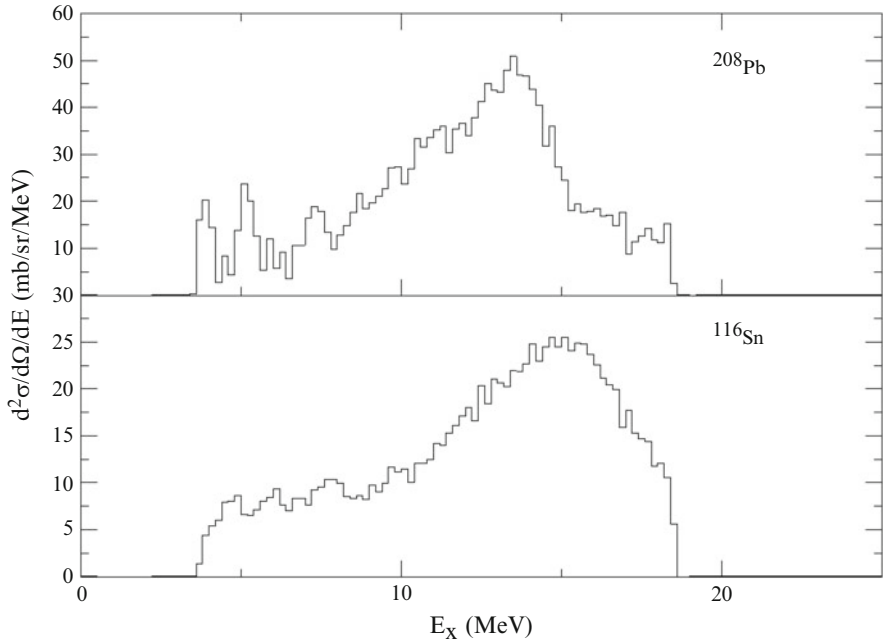

Fig. 4.8 E-318: (d,d') cross-section spectra (200 keV bin size) obtained for ^{116}Sn and ^{208}Pb isotopes at $\theta_{av} = 0.7°$

from the coulomb interaction, is subtracted out from the total cross-section before the MDA. The IVGDR contribution is obtained using the photonuclear cross-section data in conjunction with DWBA calculations on the basis of Goldhaber-Teller model. The details are presented in Sect. 2.5. No photonuclear cross-section data is available for ^{204}Pb; in this case the parameters were obtained from a global equation derived from the best fit to the available data over a wide range of nuclear masses [57]. In the event, the corresponding IVGDR cross-sections are too small to affect the MDA results in any significant way.

The IVGDR subtracted cross-sections are then expressed as the linear combination of the calculated DWBA differential cross-sections as follows,

$$\frac{d^2\sigma^{exp}(\theta_{Lab}, E_x)}{d\Omega dE} = \sum_L a_L(E_x) \frac{d^2\sigma_L^{DWBA}(\theta_{Lab}, E_x)}{d\Omega dE} \tag{4.6}$$

MDA fits are performed up to maximum angular momentum transfer of $\Delta L_{max} = 7$, in the case of α particle scattering, since the χ^2/ν saturates to 1 near about $\Delta L_{max} = 7$. However in the case of the deuteron scattering, minimum χ^2/ν was found at about $\Delta L_{max} = 5$ and MDA was performed upto $\Delta L_{max} = 5$. The fitting was obtained using a χ^2 minimization technique.

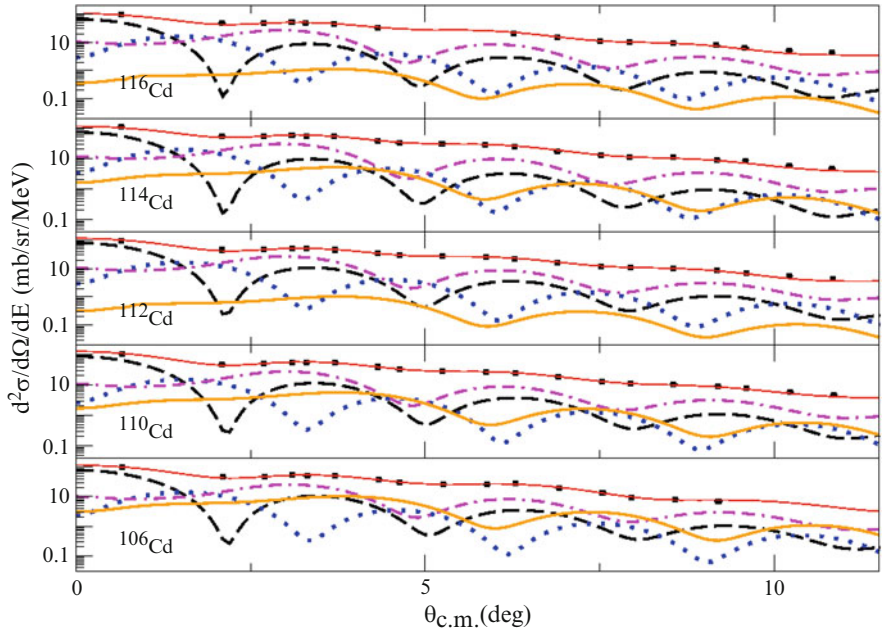

Fig. 4.9 E-309: MDA fits to the experimental differential cross-sections of $^{106,110-116}$Cd isotopes at 16.5 MeV. The *black squares* are the experimental data points. The *red line* is the fit to the data. Fits were performed for upto $L_{max} = 7$ and the corresponding contributions of only the first four multipoles, L = 0–3, are also shown: *black dashed line* for L = 0; *blue dotted line* for L = 1; *magenta dot-dashed line* for L = 2; and, *solid orange line* for L = 3

MDA fits for different target nuclei at excitation energies of corresponding ISGMR centroid energies are presented in Figs. 4.9 and 4.10 for E-309 and E-340, respectively. For E-318, experiment MDA fits at an excitation energy of 13.5 MeV are presented in Fig. 4.11; ISGMR in the case of ^{208}Pb and ISGQR in the case of ^{116}Sn peak around this excitation energy. A clear dominance of the L = 0 can be seen for ^{208}Pb as against the dominant contribution of L = 2 in the case of ^{116}Sn nucleus. MDA fits were obtained at each excitation energy within a 1 MeV grid in order to obtain the strength distributions for different multipoles. A complete set of these plots at each value of excitation energy for all the isotopes studied as a part of this thesis are presented in Appendix A.

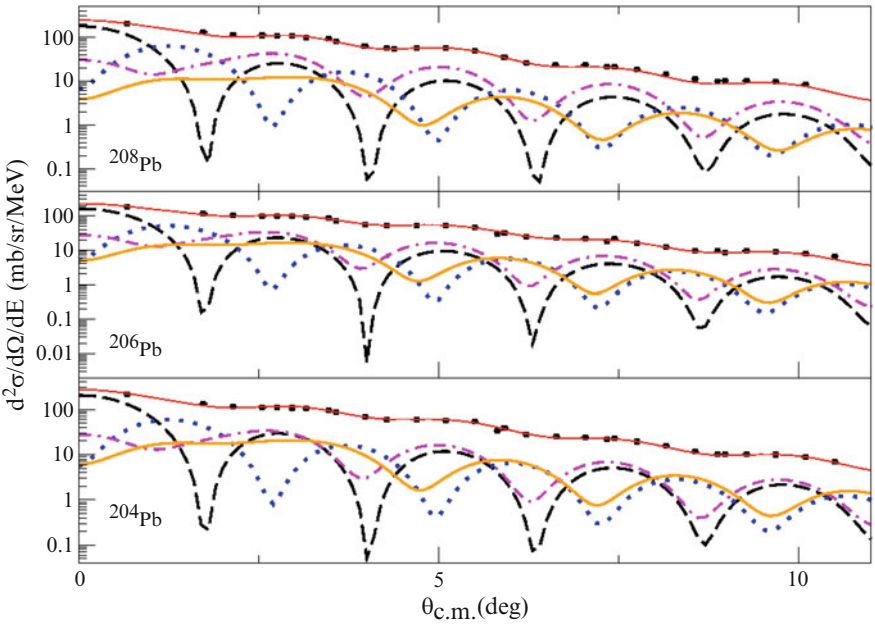

Fig. 4.10 E-340: MDA fits to the experimental differential cross-sections of $^{204–208}$Pb isotopes at 13.5 MeV. The *black squares* are the experimental data points. The *red line* is the fit to the data. Fits were performed for upto $L_{max} = 7$ and the corresponding contributions of only the first four multipoles, L = 0–3, are also shown: *black dashed line* for L = 0; *blue dotted line* for L = 1; *magenta dot-dashed line* for L = 2; and, *solid orange line* for L = 3

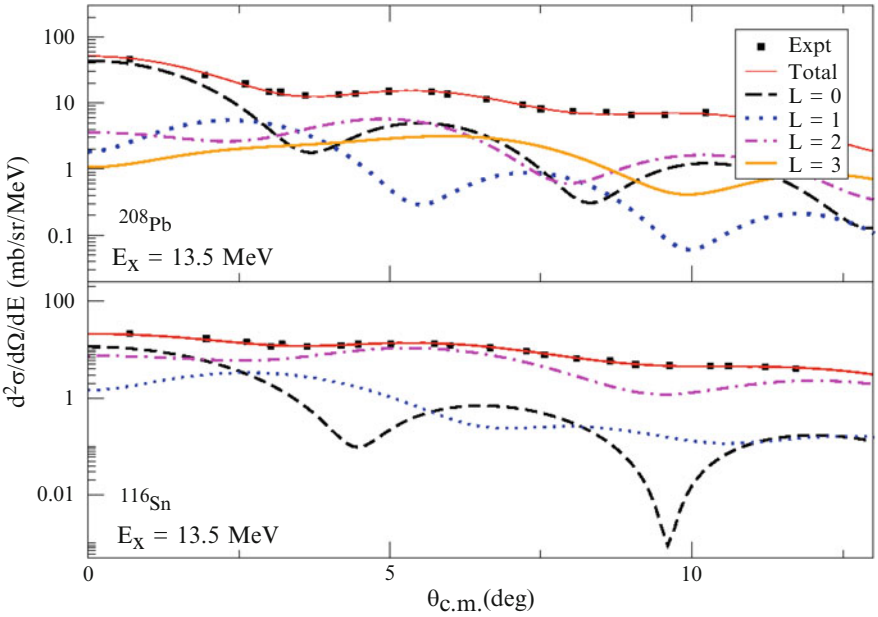

Fig. 4.11 E-318: MDA fits to the experimental differential cross-sections of ^{116}Sn and ^{208}Pb isotopes at 13.5 MeV. The *black squares* are the experimental data points. The *red line* is the fit to the data. Fits were performed for upto $L_{max} = 5$ and the corresponding contributions of only the first four multipoles, L = 0–3, are also shown: *black dashed line* for L = 0; *blue dotted line* for L = 1; *magenta dot-dashed line* for L = 2; and, *solid orange line* for L = 3

Chapter 5
Results and Discussion

5.1 Overview

As described in the previous chapter a multipole deconposition analysis (MDA) is performed. In order to extract the strength distribution of various multipoles, MDA yields the coefficients, $a_L(E_x)$ (defined by Eq. 4.6), as a function of excitation energy for a given multipolarity. These coefficients are referred to as the fractions of EWSR. These EWSR fractions are directly related to the multipole strengths by the following definitions,
For L = 0,

$$S_0(E_x) = \frac{2\hbar^2 A < r^2 >}{mE_x} a_0(E_x) \tag{5.1}$$

For L = 1,

$$S_1(E_x) = \frac{3\hbar^2 A}{32\pi mE_x}\left(11 < r^4 > -\frac{25}{3} < r^2 >^2 -10\epsilon < r^2 >\right) a_1(E_x) \tag{5.2}$$

where ϵ is defined by Eq. 2.13.
For L ≥ 2,

$$S_{L\geq 2}(E_x) = \frac{\hbar^2 A < r^{2L-2} >}{8\pi mE_x} L(2L+1)^2 a_L(E_x) \tag{5.3}$$

Here, A is the mass number, m is the nucleon mass, E_x is the excitation energy and $< r^n >$ is the nth radial moment of the ground state density. The extracted strength distributions for the isoscalar giant monopole resonance are presented in this chapter. Each strength distribution is fitted to a Lorentzian curve in order to extract the shape-parameters of the corresponding giant monopole resonances.

D.C. Patel, *A Study of the Isoscalar Giant Monopole Resonance*, Springer Theses,
DOI 10.1007/978-3-319-22207-3_5

These results are further discussed in detail for each experiment. The properties of the other giant resonances (L≥0) have also been extracted as a part of this thesis work and are presented in Appendix B.

5.2 E-309: $^{106,110-116}$Cd(α,α')

In an experimental investigation of ISGMR in a series of Sn isotopes, an intriguing feature was observed: the ISGMR centroid energies of Sn isotopes were found to be consistently lower than those predicted by relativistic and non-relativistic calculations, by as much as 1 MeV [24, 29]. These theoretical models, however, were accurately calibrated, and could reproduce ISGMR strength distributions in ^{90}Zr, ^{144}Sm and ^{208}Pb very well. In order to investigate this problem further, we have made GR measurements in the neighboring Cd isotopes. The ISGMR strength distributions extracted from the MDA analysis in the current experiment are presented in Fig. 5.1 for ^{106,110,112,114,116}Cd isotopes. The experimental strength distributions are fitted with a Lorentzian curve for each isotope and the parameters extracted are presented in Table 5.1. The centroid energies for the ISGMR, for the case of ^{110}Cd and ^{116}Cd nuclei, agree within errors with the previously obtained values [95].

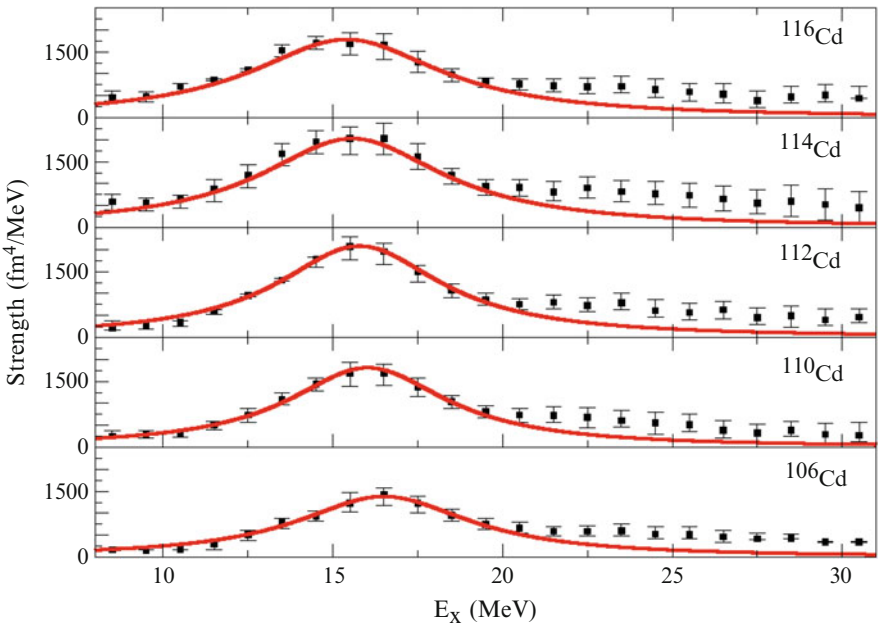

Fig. 5.1 E-309: The ISGMR strength distributions in the Cd isotopes investigated in this work. The *solid red lines* represent Lorentzian fits to the data

Table 5.1 Lorentzian-fit parameters for the ISGMR strength distributions in the Cd isotopes investigated in this work

Target	E (MeV)	Γ (MeV)	E (MeV) Ref. [95]	Γ (MeV) Ref. [95]
^{106}Cd	16.50 ± 0.19	6.14 ± 0.37	–	–
^{110}Cd	16.09 ± 0.15	5.72 ± 0.45	$15.71\ ^{+0.11}_{-0.11}$	$5.18\ ^{+0.16}_{-0.17}$
^{112}Cd	15.72 ± 0.10	5.85 ± 0.18	–	–
^{114}Cd	15.59 ± 0.20	6.41 ± 0.64	–	–
^{116}Cd	15.43 ± 0.12	6.51 ± 0.40	$15.17\ ^{+0.12}_{-0.11}$	$5.40\ ^{+0.16}_{-0.14}$

Note: For comparison, ISGMR parameters from Lui et al. (Gaussian fits) are also provided

The extra strength seen at the higher excitation energies is not well understood. However, similarly enhanced E0 and E1 strengths at high excitation energies are noted previously [29, 53, 96] and have been attributed to the contributions to the continuum from three-body channels, such as knockout reactions, which are forward peaked [97], this leads to a mimicking of the L = 0 angular distribution. These processes are implicitly included in the MDA as background and may lead to spurious contributions to the extracted multipole strengths at higher energies where the associated cross-sections are very small. This conjecture was supported by measurements of proton decay from the ISGDR at backward angles (quasifree knockout results in protons that are forward peaked) wherein no such spurious strength was observed in the spectra in coincidence with the decay protons [98–101]. Similar increase in the ISGMR strength at high excitation energies has been reported in previous work reported by Li et. al. in Sn isotopes [24] and by TAMU group in ^{12}C [102].

The ISGMR centroid energies obtained from the current analysis are compared with the calculations based on various interactions and are presented graphically in Fig. 5.2. The ISGMR centroid energies are calculated theoretically in terms of the moment ratios, defined as $m_k = \int E_x^k S(E_x) dx$. The moment ratios obtained from this work and the theoretical results extracted from the distributions of isoscalar monopole strength computed in a relativistic random phase approximation (RPA) using the accurately calibrated NL3 ($K_\infty = 271$ MeV) [103] and FSUGold ($K_\infty = 230$ MeV) [104] effective interactions are summarized in Table 5.2. A detailed description of the relativistic RPA formalism and its implementation may be found in Ref. [105]. The use of the NL3 effective interaction, with an incompressibility coefficient significantly larger than FSUGold, exacerbates the discrepancy between theory and experiment even further. Likewise, in a recently available calculation [4] within the Skyrme Hartree-Fock+BCS and quasiparticle RPA with the SLy5 parameter set ($K_\infty = 230$ MeV), which reproduces the ISGMR in ^{208}Pb very well, the centroids of ISGMR strength distributions in the Cd isotopes (also shown in Fig. 5.2) are, again, significantly larger than the experimentally-obtained results. Thus, the question originally posed in Refs. [26, 35, 106] of "*Why are the Sn isotopes so Fluffy*" extends to the cadmium isotopes as well.

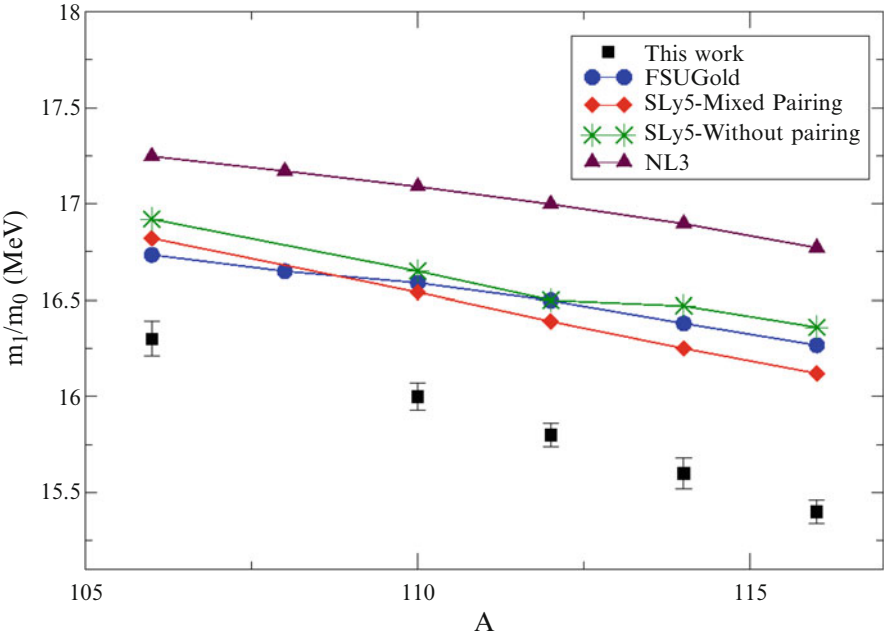

Fig. 5.2 E-309: Systematics of the moment ratio, m_1/m_0 for the ISGMR strength distributions in the Cd isotopes investigated in this work. The experimental results (*squares*) are compared with relativistic calculations performed using the FSUGold (*circles*) and NL3 interaction (*diamonds*). Also presented are results from non-relativistic calculations performed using the SLy5 parameter set in the HFB+QRPA formalism with and without the mixed pairing interaction (*diamonds* and *stars*, respectively) [4]. The *solid lines* are to guide the eye

As can be noted, even with the inclusion of pairing effects, using a mixed pairing interaction [4], the centroids of the ISGMR remain well above the experimental values (Fig. 5.2) – the net effect pf pairing appears to be that of lowering the centroid by only $\sim$100 keV in ^{106}Cd to a maximum of $\sim$240 keV in ^{116}Cd. Thus, the impact of superfluid correlations on the compressibility of a fermionic droplet remains an interesting open question [36] to date in spite of significant theoretical effort [4, 31, 33, 34, 36, 107], no single approach has been able to simultaneously describe the centroid energies in ^{90}Zr, ^{208}Pb, and the Sn/Cd isotopes. The remaining challenge, therefore, is not only to describe the distribution of monopole strength along the isotopic chain in tin and cadmium, but to do so without sacrificing the enormous success already achieved in reproducing a host of ground-state observables and collective modes.

Measurements made on series of isotopes presents a way to extract the asymmetry term, K_τ, in nuclear incompressibility expansion, Eq. 1.11. K_τ obtained from the study of finite nuclei is strongly correlated with the corresponding term in infinite

Table 5.2 Moment ratios calculated over the excitation-energy range 10.5–20.5 MeV

Target	$\sqrt{m_1/m_{-1}}$ (MeV)	m_1/m_0 (MeV)				
		This work	FSUGold	NL3	SLy5 [4]	
					Mixed pairing	Without pairing
^{106}Cd	16.06±0.05	16.27±0.09	16.73	17.25	16.82±0.55	16.92
^{108}Cd	–	–	16.65	17.17	–	–
^{110}Cd	15.72±0.05	15.94±0.07	16.59	17.09	16.54± 0.60	16.65
^{112}Cd	15.59±0.05	15.80±0.05	16.50	17.00	16.39± 0.59	16.50
^{114}Cd	15.37±0.08	15.61±0.08	16.38	16.90	16.25±0.64	16.47
^{116}Cd	15.19±0.06	15.44±0.06	16.27	16.77	16.12±0.68	16.36

Note: The numbers for the SLy5 interaction without pairing were obtained in a private communication with G. Colò

nuclear matter, K_τ^∞, and is vital in placing stringent constraints on the density dependence of the symmetry energy. K_τ^∞ is simply related to a few fundamental parameters of the equation of state [108]:

$$K_\tau^\infty = K_{\rm sym} - 6L - \frac{Q_0}{K_\infty} L\,, \tag{5.4}$$

where Q_0 is the *"skewness"* parameter of symmetric nuclear matter, and L and $K_{\rm sym}$, respectively, are the slope and curvature of the symmetry energy. It is the strong sensitivity of K_τ^∞ to the density dependence of the symmetry energy that makes the present study of critical importance in constraining the EOS of neutron-rich matter.

In order to extract K_τ from the observed nuclear incompressibility, K_A, in the Cd isotopes, Eq. 1.11 can be rewritten as,

$$K_A - K_{Coul} Z^2 A^{-4/3} = K_{vol}\left(1 + cA^{-1/3}\right) + K_\tau \left(\frac{N-Z}{A}\right)^2 \tag{5.5}$$

Here, c ≈ -1 [109], and K_{Coul} is essentially model independent (in the sense that the deviations from one theoretical model to another are quite small), so that the associated term can be calculated for a given isotope. For the series of $^{106,110-116}$Cd isotopes studied as a part of this thesis work, the neutron-proton asymmetry changes by 83 % across the isotopic chain. Whereas the $K_{vol}(1+cA^{-1/3})$ term changes 0.5 % over the isotopic chain. Therefore, an approximately quadratic relation between $\left[K_A - K_{Coul} Z^2 A^{-4/3}\right]$ and the neutron-proton asymmetry, (N-Z)/A, of the form $y = A + Bx^2$ can be applied to fit the experimental data. K_τ can then be identified as the fitting parameter B. K_A is calculated using Eq. 1.9 where the moment ratio $\sqrt{m_1/m_{-1}}$ is identified as E_{ISGMR}. The value of K_{Coul} is taken to be -5.2 ± 0.7 MeV from Ref. [5]. The quadratic fit for the Cd isotopes is shown in Fig. 5.3. The value of K_τ obtained from this fit is -555 ± 75 MeV; the quoted error includes the effect ($\sim$20 MeV) of the uncertainty in the value of K_{Coul}. This result

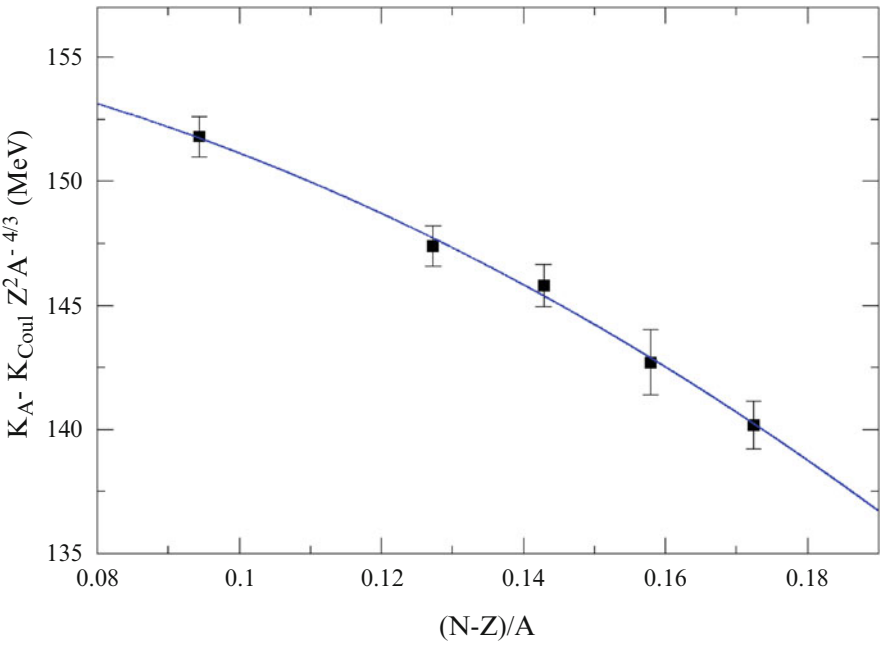

Fig. 5.3 The difference $K_A - K_{Coul}Z^2A^{-4/3}$ in the Cd isotopes investigated in this work plotted as a function of the asymmetry parameter, $(N-Z)/A$. The values of K_A have been derived using the customary moment ratio $\sqrt{m_1/m_{-1}}$ for the energy of ISGMR, and a value of 5.2±0.7 MeV has been used for K_{Coul} [5]. The *solid line* represents a quadratic fit to the data

confirms, and is in excellent agreement with, the value $K_\tau = -550\pm100$ MeV obtained from the Sn isotopes [24, 29]. This value is also consistent with the $K_\tau = -370\pm120$ MeV obtained from the analysis of the isotopic transport ratios in medium-energy heavy-ion reactions [110], $K_\tau = -500^{+120}_{-100}$ MeV obtained from constraints placed by neutron-skin data from anti-protonic atoms across the mass table [108], and $K_\tau = -500\pm50$ MeV obtained from theoretical calculations using different Skyrme interactions and relativistic mean-field (RMF) Lagrangians [5].

5.3 E-340: $^{204-208}$Pb(α,α')

The softness observed in Sn isotopes is confirmed from the experimental investigation on Cd isotopes (E-309) [111]. An intriguing proposal put forward to explain this discrepancy was that the mutual enhancement of magicity (MEM) effect may play a role in the nuclear incompressibility [36]. MEM refers to a strong underbinding observed in the Hartree-Fock mass formulas (HFMF) for all doubly magic nuclei and their immediate neighbors, formed by adding or removing not more than one nucleon [112, 113]. As noted in Ref. [113], there are 27 such nuclei for which the

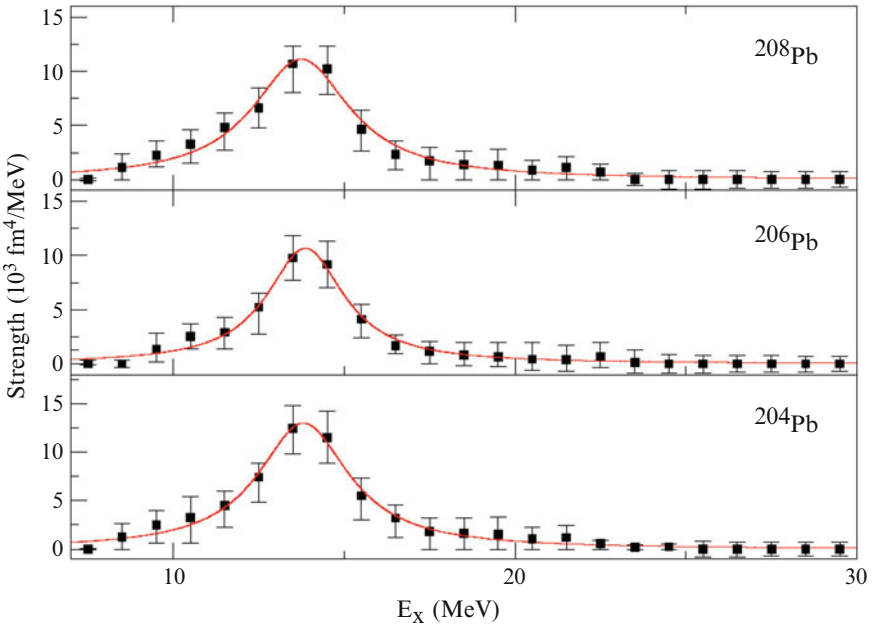

Fig. 5.4 The ISGMR strength distributions of the Pb isotopes investigated in this work. *Solid lines* represent Lorentzian fits to the data

mean error between the experimentally measured values of the nuclear masses and those calculated by HFMF is ≈1.31 MeV as against ≈40 keV for the complete set of >1700 data points available at the time of that compilation. For the Pb isotopes, inclusion of this MEM effect in the calculation of ISGMR centroid energies has been shown to predict higher ISGMR centroid energy in ^{208}Pb by ∼600 keV, compared to corresponding ISGMR centroid energies in ^{204,206}Pb nuclei [36]. With a view to test this MEM effect in Pb isotopes, measurements were made on the three lead isotopes simultaneously in order to eliminate the systematic errors. The results of the MDA fits were used to obtain the ISGMR strength distributions; these strength distributions are shown in Fig. 5.4. Experimental distributions were fitted with a Lorentzian curve and the parameters for these fits are summarized in Table 5.3. The centroid energies obtained from this experiment, for the ^{206}Pb and ^{208}Pb nuclei, agree within errors with the previous measurements [114–116]. The experimental ISGMR centroid energies are very close to each other for the three Pb isotopes, in stark disagreement with the predicted ∼600 keV difference in the ISGMR centroid energies of ^{204}Pb and ^{208}Pb resulting from the MEM effect as shown in Fig. 5.5.

The moment ratio, $\sqrt{m_1/m_{-1}}$, for the three Pb isotopes obtained in this experiment have been compared with theoretical values calculated in the constrained HFB formalism taking into account the MEM effect. The results are presented in Table 5.4. The moment ratios were computed over the energy range 9.5–19.5 MeV; this energy range incorporates nearly all of the ISGMR strength. Also the values

Table 5.3 Lorentzian fit parameters for the ISGMR distributions obtained for the three Pb isotopes

Target		This work	RCNP-U[114]	TAMU* [115]	KVI[116]
^{204}Pb	E (MeV)	13.8 ± 0.1	–	–	–
	Γ (MeV)	3.3 ± 0.2	–	–	–
^{206}Pb	E (MeV)	13.8 ± 0.1	–	–	14.0 ± 0.3
	Γ (MeV)	2.8 ± 0.2	–	–	2.0 ± 0.4
^{208}Pb	E (MeV)	13.7 ± 0.1	13.5 ± 0.2	13.96 ± 0.20	13.9 ± 0.3
	Γ (MeV)	3.3 ± 0.2	4.2 ± 0.3	2.88 ± 0.20	2.5 ± 0.4

Note: Parameter values marked with an astrisk (*) were extracted from the moment ratios rather than peak fitting

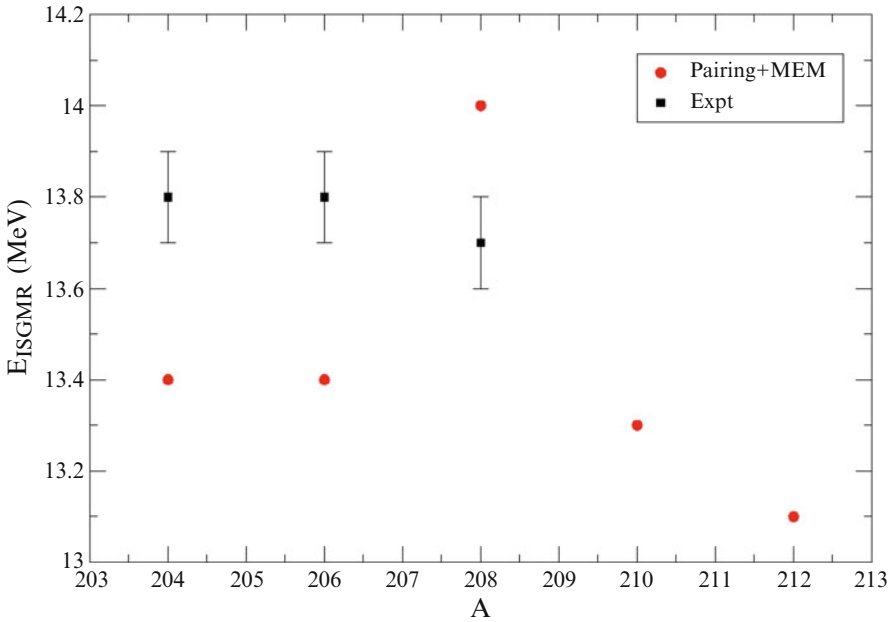

Fig. 5.5 The ISGMR centroid energies of the Pb isotopes. *Red circles* are the energies calculated with constrainted HFB method, taking into account the MEM effect [3] and *black squares* are experimentally obtained values [6]

of the product, $E_{ISGMR}A^{-1/3}$, are compared with theoretical values. $E_{ISGMR}A^{1/3}$ is practically identical for the three isotopes, indicating that the ISGMR centroid energies follow the standard $A^{-1/3}$ dependence.

These results are in contrast with the theoretical predictions of Ref. [36], where $E_{ISGMR}A^{1/3}$ varies by 4 MeV between ^{204}Pb and ^{208}Pb. It can be concluded without much ambiguity, then, that the MEM effect does not play a measurable role in the energy of the ISGMR in the Pb isotopes and, thence, in the nuclear incompressibility. The MEM effect, thus, fails to account for the observed softness of the Sn and the Cd isotopes, and this question remains open still.

Table 5.4 The moment ratio, $\sqrt{m_1/m_{-1}}$, values obtained in this experiment and calculated over the energy range of 9.5–19.5 MeV are presented

Target	$\sqrt{m_1/m_{-1}}$ (MeV)		$E_{ISGMR}A^{1/3}$ (MeV)	
	This work	Pairing+MEM [36]	This work	Pairing+MEM [36]
^{204}Pb	13.7±0.1	13.4	81.2±0.6	78.9
^{206}Pb	13.6±0.1	13.4	81.5±0.6	79.1
^{208}Pb	13.5±0.1	14.0	81.2±0.6	82.9

Incidentally, the difference in E_{ISGMR} for ^{204}Pb and ^{208}Pb due to the K_τ value obtained from the measurements on the Sn and Cd isotopes [6, 24, 29] would be 0.19±0.03 MeV, consistent with the current meaurements.

5.4 E-318: ^{116}Sn(d,d'),^{208}Pb(d,d')

Giant resonance in stable isotopes have been studied extensively using various probes. With the current inconsistencies between experimental observations and theoretical calculations, as described in the previous sections, it is important to explore nuclear incompressibility in nuclei far from line of stability. This is important in understanding the effect of large neutron-proton asymmetries on the nuclear incompressibility. There is also a possibility of exploring the properties of "Pygmy" resonance in halo nuclei, resulting from the "core" oscillating against the skin. One would then be looking at two incompressibilities, that of the "core" and the "skin". These measurements would have to be done in inverse kinematics using radioactive ion beams. With high intensity radioactive ion beams becoming available at various facilities around the world, these measurements are now possible. One option for performing such measurements is using an active target-time projection chamber (AT-TPC) [41]. Deuteron gas can be used as an active target having dual functionality- serving as both the target gas and as a detector gas. However, establishing the feasibility in obtaining the ISGMR strength distributions correctly such a measurement is very important. The goal of the current experiment was to measure GR properties in two previously studied "standard" nuclei, ^{116}Sn and ^{208}Pb, to establish the appropriateness of this probe for such studies. Also, for the first time, we have employed the MDA technique, previously developed for α-particles, to extract strength distributions of various multipoles for inelastic spectra obtained using the deuteron probe.

The extracted ISGMR and ISGQR strength distributions for the ^{116}Sn and ^{208}Pb nuclei are shown in Figs. 5.6 and 5.7. The data was taken over only a limited energy range due to experimental constraints. The strength distributions are fitted to a Lorentzian curve and the extracted parameters are presented in Tables 5.5 and 5.6. For comparison, the ISGMR and ISGQR strength distribution parameters from previous measurements using the α and deuteron probes are also presented. As can

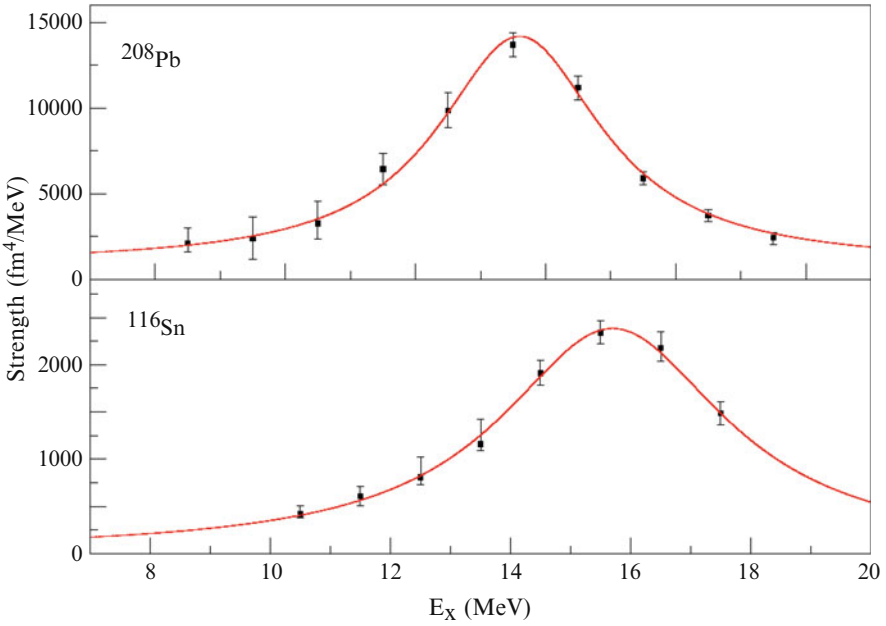

Fig. 5.6 The ISGMR strength distributions for ^{116}Sn (*lower panel*) and ^{208}Pb (*upper panel*) obtained in this work. *Solid lines* represent Lorentzian fits to the data

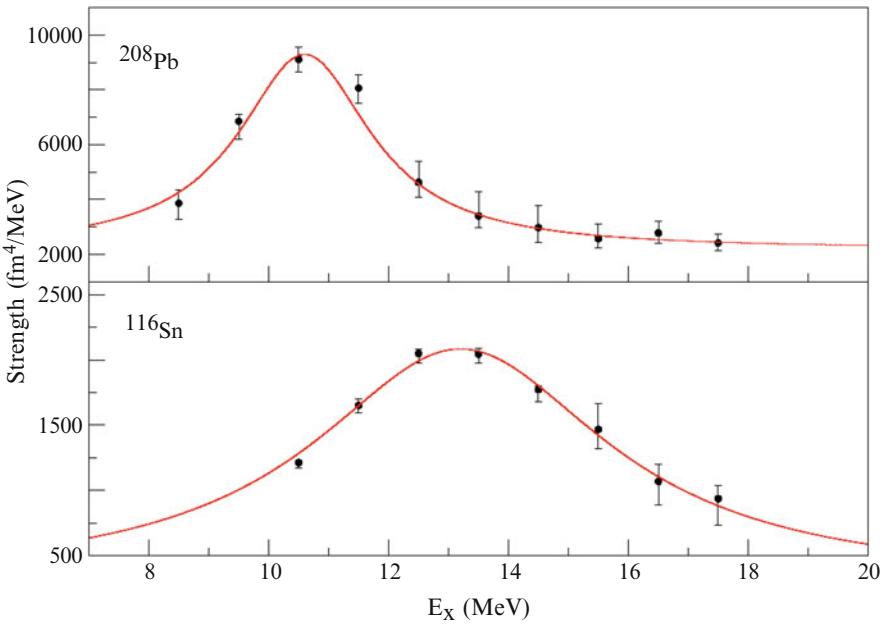

Fig. 5.7 The ISGQR strength distributions for ^{116}Sn (*lower panel*) and ^{208}Pb (*Upper panel*) isotopes investigated in this work. *Solid lines* represent Lorentzian fits to the data

Table 5.5 Lorentzian fit parameters for the ISGMR strength distributions for ^{116}Sn and ^{208}Pb

	E_{ISGMR} (MeV)	Γ_{ISGMR} (MeV)	% EWSR
	^{208}Pb		
This work	13.6 ± 0.1	3.1 ± 0.4	147 ± 18
Orsay [46]	13.5 ± 0.3	2.8 ± 0.2	307 ± 60
Jülich [27]	13.8 ± 0.3	2.6 ± 0.3	–
RCNP [114]	13.5 ± 0.2	4.2 ± 0.3	58 ± 3
TAMU* [115]	13.96 ± 0.20	2.88 ± 0.20	99 ± 15
IUCF [117]	13.9 ± 0.4	3.2 ± 0.4	100 ± 20
KVI [116]	13.9 ± 0.3	2.5 ± 0.4	110 ± 22
	^{116}Sn		
This work	15.7 ± 0.1	4.6 ± 0.7	73 ± 15
RCNP [24]	15.8 ± 0.1	4.1 ± 0.3	99 ± 5
TAMU* [115]	15.85 ± 0.20	5.27 ± 0.25	112 ± 15
KVI [118]	15.69 ± 0.16	3.73 ± 0.39	101 ± 22

Note: Parameter values marked with an astrisk (*) were extracted from the moment ratios rather than peak fitting

Table 5.6 Lorentzian fit parameters for the ISGQR strength distributions for ^{116}Sn and ^{208}Pb

	E_{ISGQR} (MeV)	Γ_{ISGQR} (MeV)	% EWSR
	^{208}Pb		
This work	10.6 ± 0.2	2.7 ± 0.4	98 ± 9
Orsay [46]	10.5 ± 0.2	2.8 ± 0.2	85 ± 15
Jülich [27]	10.9 ± 0.3	2.6 ± 0.3	–
TAMU* [115]	10.89 ± 0.30	3.00 ± 0.30	100 ± 13
IUCF [117]	10.9 ± 0.3	2.4 ± 0.4	77 ± 15
KVI [116]	10.9 ± 0.3	3.0 ± 0.3	145 ± 30
	^{116}Sn		
This work	13.2 ± 0.1	6.0 ± 1.0	73 ± 23
RCNP [24]	13.1 ± 0.1	6.4 ± 0.4	112 ± 4
TAMU* [115]	13.50 ± 0.35	5.00 ± 0.30	108 ± 12
KVI [118]	13.39 ± 0.14	2.94 ± 0.31	134 ± 28

be noted, the values obtained from current experiment agree well, within errors, with all the previous measurements. The EWSR values are obtained over the excitation energy range covered in this experiment; the quoted uncertainties in EWSR values are statistical only.

The current measurement clearly establishes that a reliable extraction of the ISGMR strength distributions from inelastic deuteron scattering using the MDA technique is possible. Small-angle deuteron inelastic scattering can thus serve reliably for investigation of the ISGMR in nuclei far from stability using inverse-kinematics reactions, making it possible to investigate the properties of ISGMR in the exotic nuclei at the rare isotope beam facilities currently operational, and being planned, worldwide.

Chapter 6
Summary and Current Status

The nuclear matter equation of state (EOS) plays an important role in our understanding of nuclear bulk properties, as well as processes taking place in the stellar environments (i.e. dynamics of supernovae collapse and structure of neutron stars). The EOS also sheds light on the phase transitions taking place in the heavy ion collision reactions. Its exact determination is being pursued extensively, both experimentally and theoretically. Nuclear incompressibility is an important parameter of the nuclear matter EOS. The centroid energy of one of the nuclear compression modes – the isoscalar Giant Monopole Resonance (ISGMR) – is a direct experimental tool to constrain the value of nuclear matter incompressibility.

We have measured giant resonance (GR) strength distributions in a series of ^{106,110,112,114,116}Cd and ^{204,206,208}Pb isotopes with a view of answering one of the "open" questions in nuclear physics [7, 13]: "Why are Sn isotopes so soft?". Additionally, with an aim to further extend the work to more neutron-rich nuclei, the last part of this thesis is dedicated to establishing the feasibility of deuterium as a probe for future GR studies in nuclei far from the line of stability and thus explore the density dependence of symmetry energy in more detail.

Experiments were performed at the Research Center for Nuclear Physics (RCNP), Osaka University, Japan. Extremely forward angle inelastic scattering measurements (including 0°) were made to take advantage of the distinctive angular distributions exhibited by transitions of different multipolarity using the high resolution spectrometer, Grand Raiden. Elastic scattering measurements were performed in order to obtain the optical model parameters. Multipole decomposition analysis (MDA) was performed to extract the strength distributions for the various multipole. Distorted-wave Born approximation (DWBA) angular distributions were calculated in the frame-work of the hybrid model for α scattering experiments and the phenomenological model for the deuteron scattering experiment. A hybrid optical model was constructed with the single folding calculation (using density dependent α-nucleon interaction) for the real part and Wood-Saxon shaped potential for the imaginary part.

D.C. Patel, *A Study of the Isoscalar Giant Monopole Resonance*, Springer Theses,
DOI 10.1007/978-3-319-22207-3_6

The ISGMR strength distributions were extracted for the Cd isotopes. The ISGMR centroid energies show softness similar to that in the Sn isotopes (observed in a previous study). The relativistic, as well as the non-relativistic calculations including pairing effects, overestimate the ISGMR centroid energies in the Cd isotopes. The asymmetry term in the nuclear incompressibility, K_τ, extracted from the analysis of Cd isotopes was found to be -555 ± 75 MeV [111].

We investigated an intriguing theoretical conjecture to explain the softness in the Sn and Cd isotopes, viz. consequences of the MEM effect on ISGMR centroid energies. The GR measurements in Pb isotopes were dedicated to testing this MEM effect as predicted to manifest in Pb isotopes. The ISGMR centroid energies measured in the series of Pb isotopes indicated a standard $A^{-1/3}$ dependence in stark contrast to a sharp increase of 0.6 MeV in the ISGMR centroid energy of ^{208}Pb when compared to the centroid energy of ^{204}Pb that was predicted as resulting from the MEM effect. These results clearly established that MEM effect does not play a measurable role in the energy of the ISGMR, thereby leaving the question of "softness" in the Sn and Cd unanswered still [6].

Combining the results of GR measurements from this thesis work (in Cd and Pb isotopes) and all the previous measurements, a more global picture can be constructed. A strong correlation exists between the symmetry energy coefficient J and the asymmetry term in the nuclear incompressibility. Using this correlation and the value of K_τ obtained from the GR experiments and other independent measurements the value of J is found to lie between, $27.7 \leq J \leq 35.6$ MeV corresponding to $K_\tau = -550 \pm 100$ MeV, as shown in Fig. 6.1 [7].

The parameter-set for a given class of energy functionals is characterized by specific values of K_∞ and K_τ. The "experimental" values thus obtained from the ISGMR for K_∞ and K_τ taken together can provide a means of selecting the most appropriate of the interactions used in nuclear structure and EOS calculations. Figure 6.2 shows K_∞ values plotted against different K_τ values used in different interactions. The constraints put by K_τ values obtained from the ISGMR in the Sn and Cd isotopes and the currently adopted value of $K_\infty = 240 \pm 20$ MeV [7, 13], leaves only a small number of the commonly used interactions as "acceptable".

To facilitate future GR studies in radioactive isotopes, the feasibility of deuteron inelastic scattering for such studies was tested as a third and the last part of this thesis work. The ISGMR and ISGQR strength distributions in ^{116}Sn and ^{208}Pb were extracted using a high energy (100 MeV/u) deuteron beam. For the first time, the MDA technique was successfully employed to delineate different multipole contributions reliably. Various features of these strength distributions are compared with the previous measurements; they agree within experimental errors. This established the feasibility of using deuteron probe to study GRs in the radioactive nuclei using inverse kinematics [119]. With the new radioactive beam facilities becoming available world wide and the improved detector systems for such measurements, GR studies would be possible in the radioactive nuclei. With these measurements in nuclei far from stability line, one hopes to answer the question of "softness" in some detail and also explore the density dependence of the symmetry energy in the nuclear matter EOS.

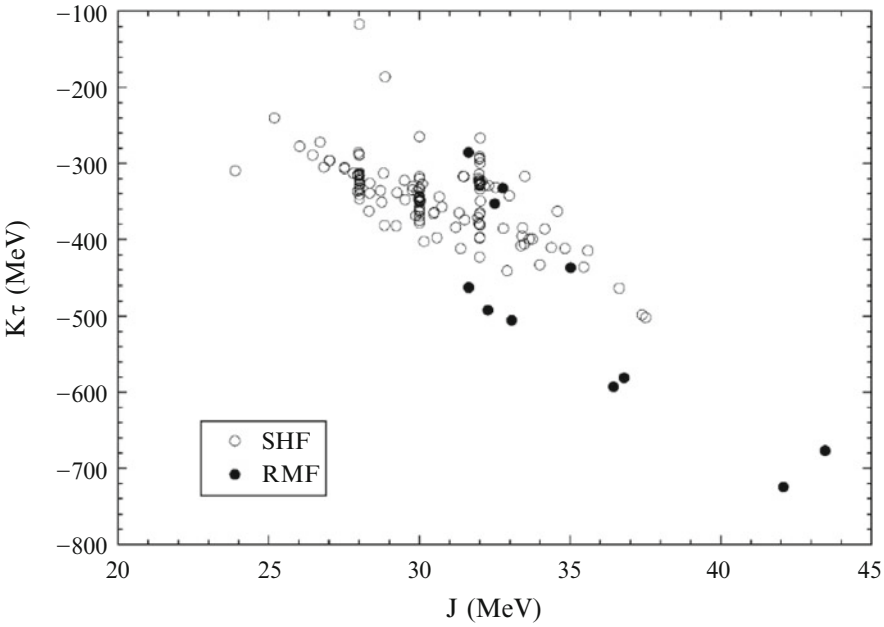

Fig. 6.1 Correlation between the asymmetry term of the finite nucleus incompressibility K_τ and the volume symmetry term J, calculated by using various Skyrme parameter sets (SHF, *open circles*) and relativistic Lagrangians (RMF, *filled circles* [Adapted from Ref. [7]])

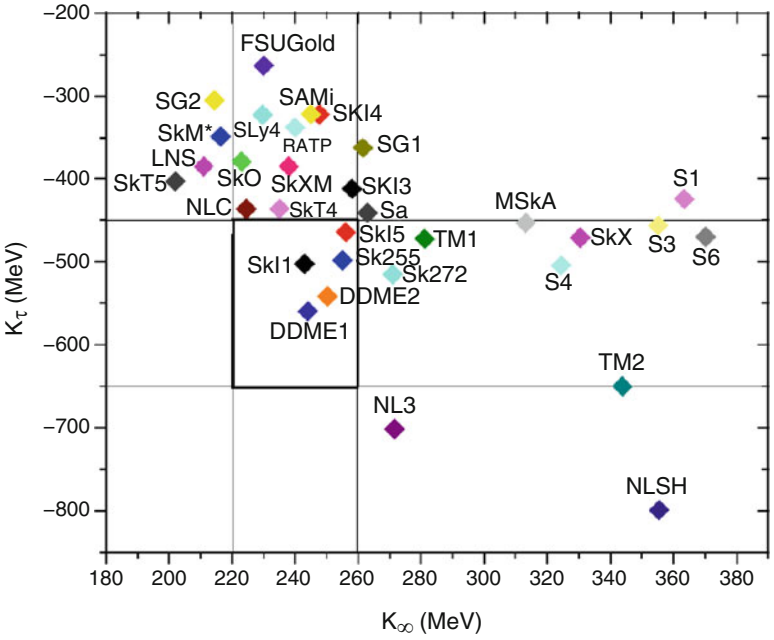

Fig. 6.2 Values of K_∞ and K_τ calculated from the parameter-sets of various interactions as labled [7]. The *vertical* and *horizontal lines* indicate the experimental ranges of K_∞ and K_τ, as determined from the GMR work

Appendix A
Multipole Decomposition Analysis Results

Multipole decomposition analysis was performed on the experimental angular distributions at excitation energy interval of 1 MeV. The results of these fits for all the isotopes studied as a part of this thesis work are presented in this section.

D.C. Patel, *A Study of the Isoscalar Giant Monopole Resonance*, Springer Theses,
DOI 10.1007/978-3-319-22207-3

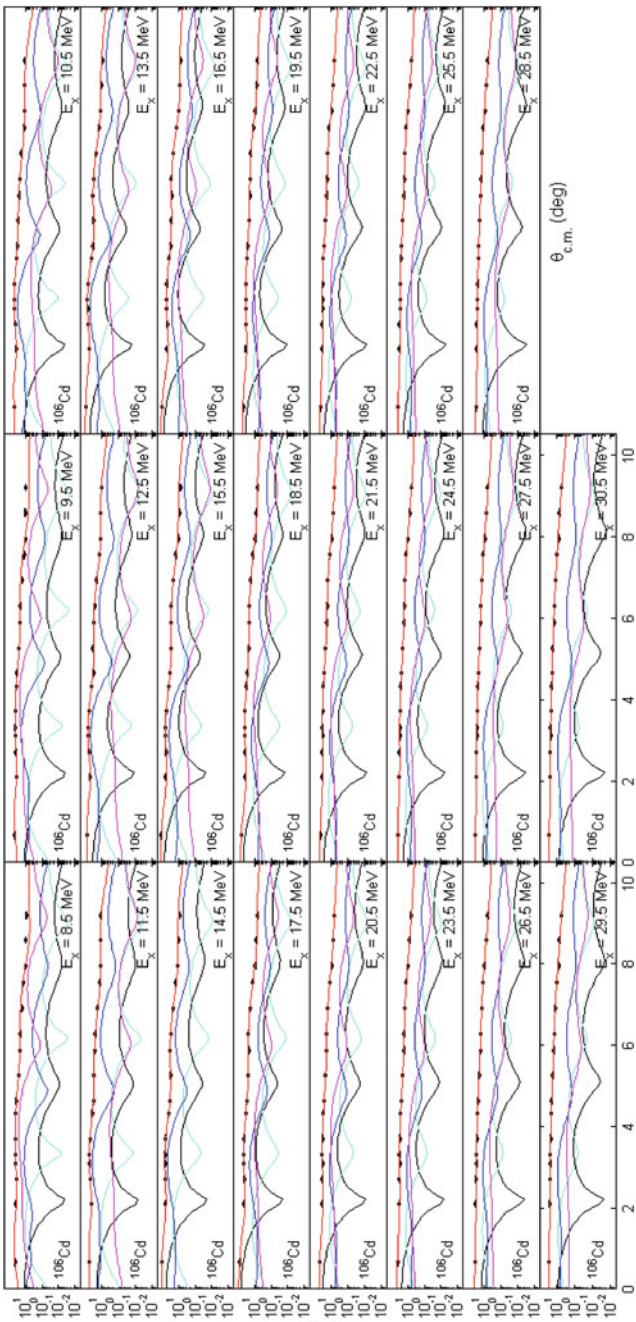

Fig. A.1 Results of MDA analysis for ^{106}Cd at E_x = 8.5 to 30.5 MeV. *Black squares* are the experimental data points. *Red line* is the fit to the data. The corresponding contributions of the first four multipoles, L = 0–3 are shown. *Black line* for L = 0, *cyan line* for L = 1, *blue line* for L = 2 and *magenta line* for L = 3

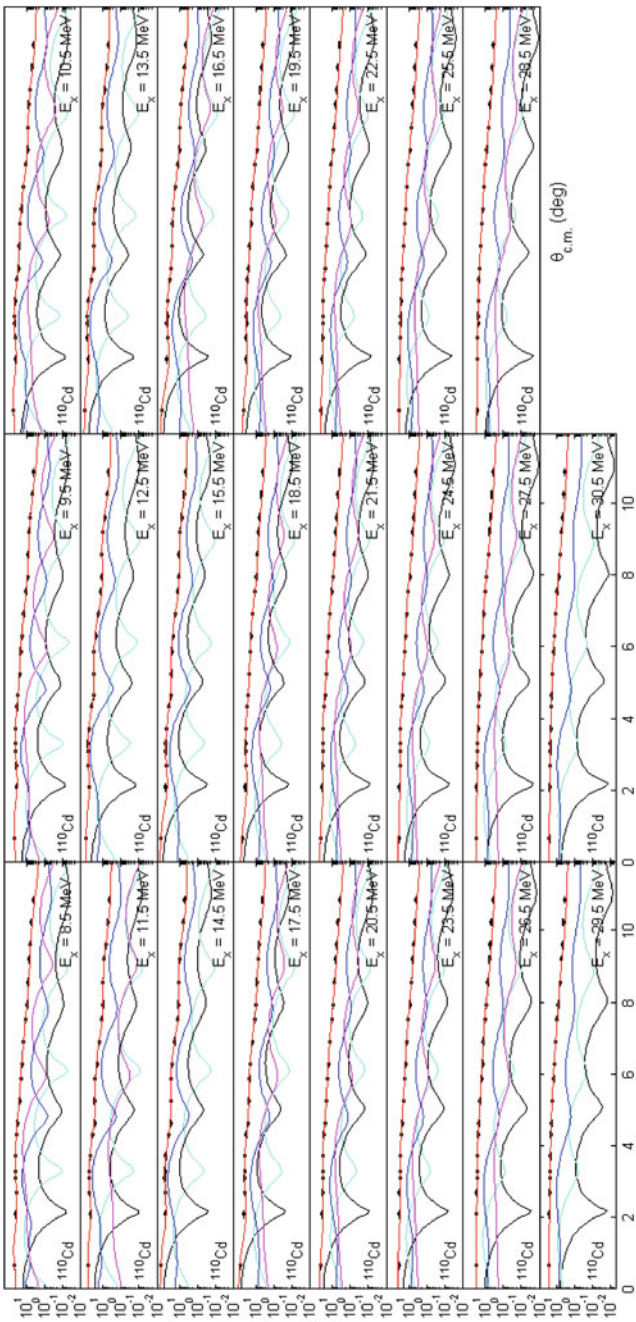

Fig. A.2 Results of MDA analysis for ^{110}Cd at E_x = 8.5 to 30.5 MeV. *Black squares* are the experimental data points. *Red line* is the fit to the data. The corresponding contributions of the first four multipoles, L = 0–3 are shown. *Black line* for L = 0, *cyan line* for L = 1, *blue line* for L = 2 and *magenta line* for L = 3

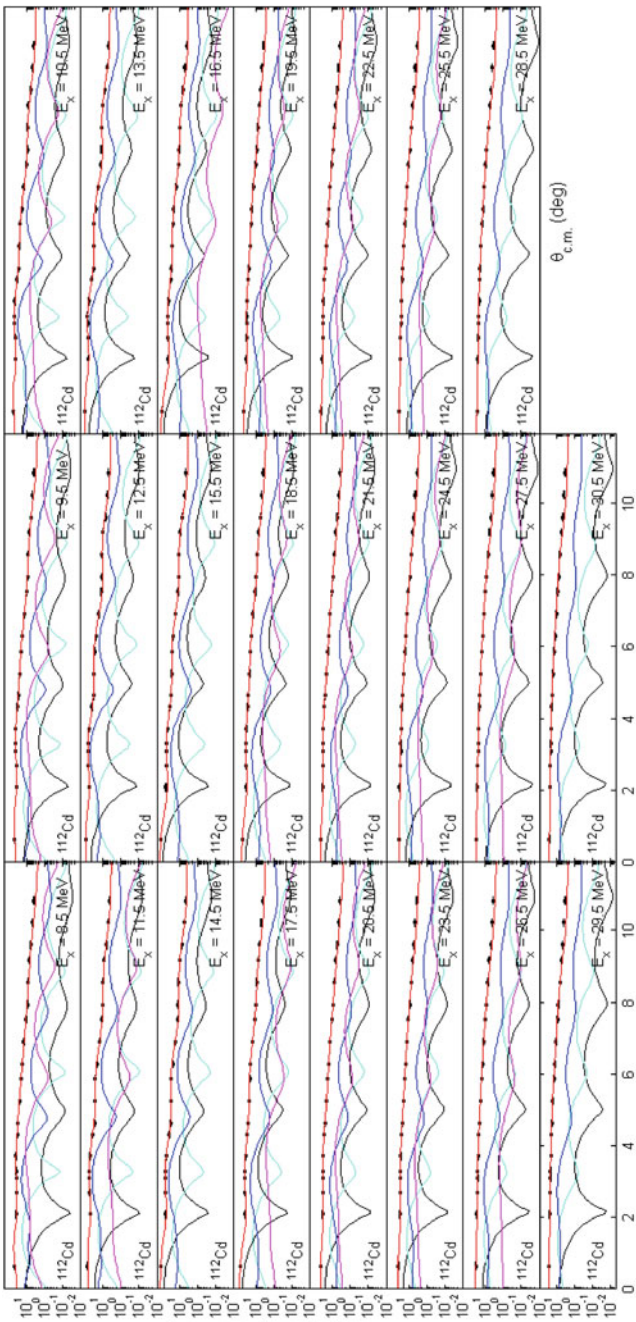

Fig. A.3 Results of MDA analysis for ^{112}Cd at E_x = 8.5 to 30.5 MeV. *Black squares* are the experimental data points. *Red line* is the fit to the data. The corresponding contributions of the first four multipoles, L = 0–3 are shown. *Black line* for L = 0, *cyan line* for L = 1, *blue line* for L = 2 and *magenta line* for L = 3

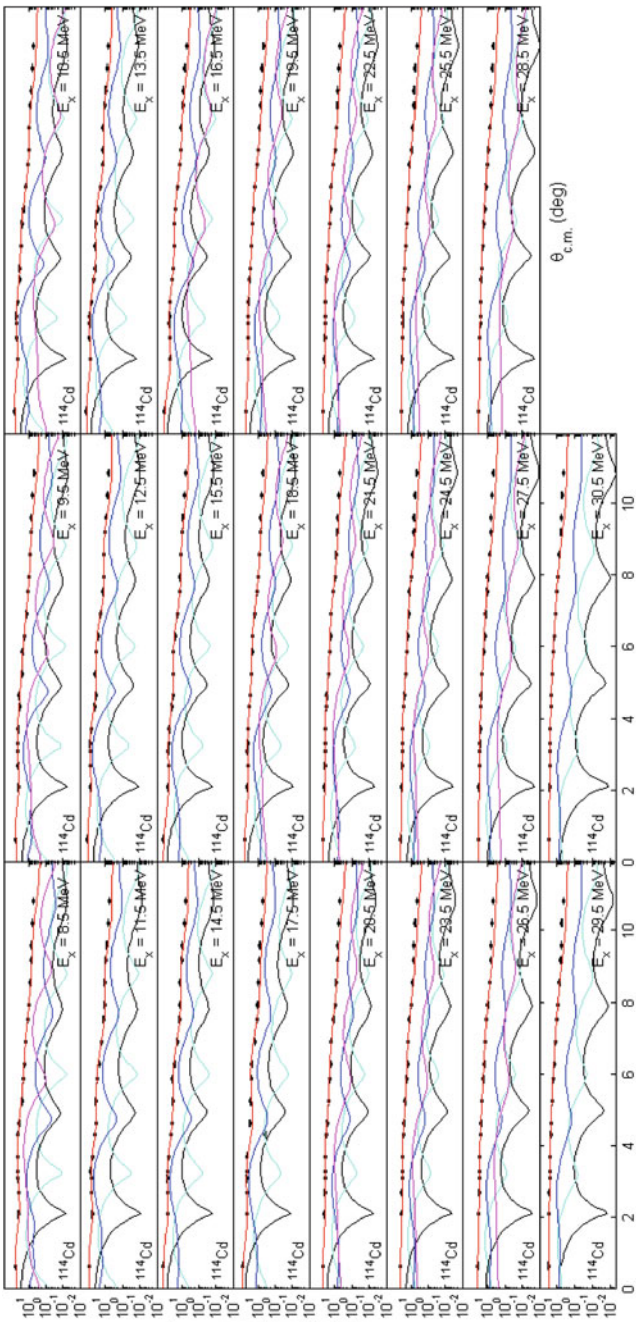

Fig. A.4 Results of MDA analysis for ^{114}Cd at E_x = 8.5 to 30.5 MeV. *Black squares* are the experimental data points. *Red line* is the fit to the data. The corresponding contributions of the first four multipoles, L = 0–3 are shown. *Black line* for L = 0, *cyan line* for L = 1, *blue line* for L = 2 and *magenta line* for L = 3

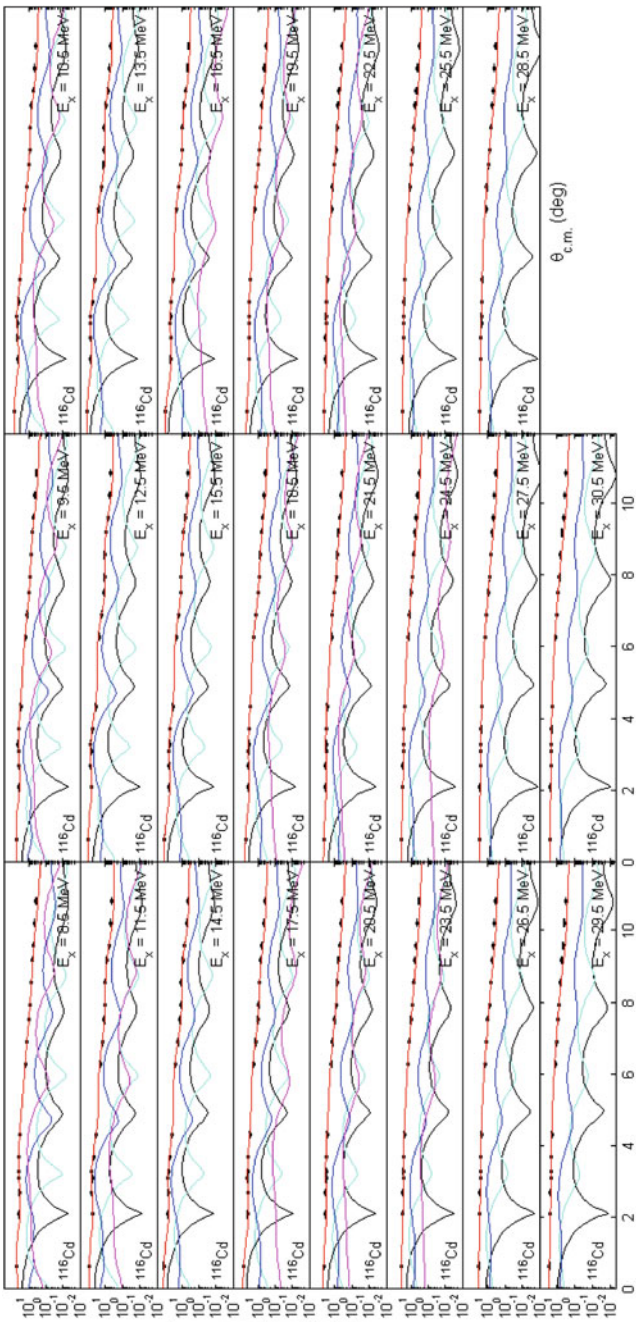

Fig. A.5 Results of MDA analysis for ^{116}Cd at E_x = 8.5 to 30.5 MeV. *Black squares* are the experimental datapoints. *Red line* is the fit to the data. The corresponding contributions of the first four multipoles, L = 0–3 are shown. *Black line* for L = 0, *cyan line* for L = 1, *blue line* for L = 2 and *magenta line* for L = 3

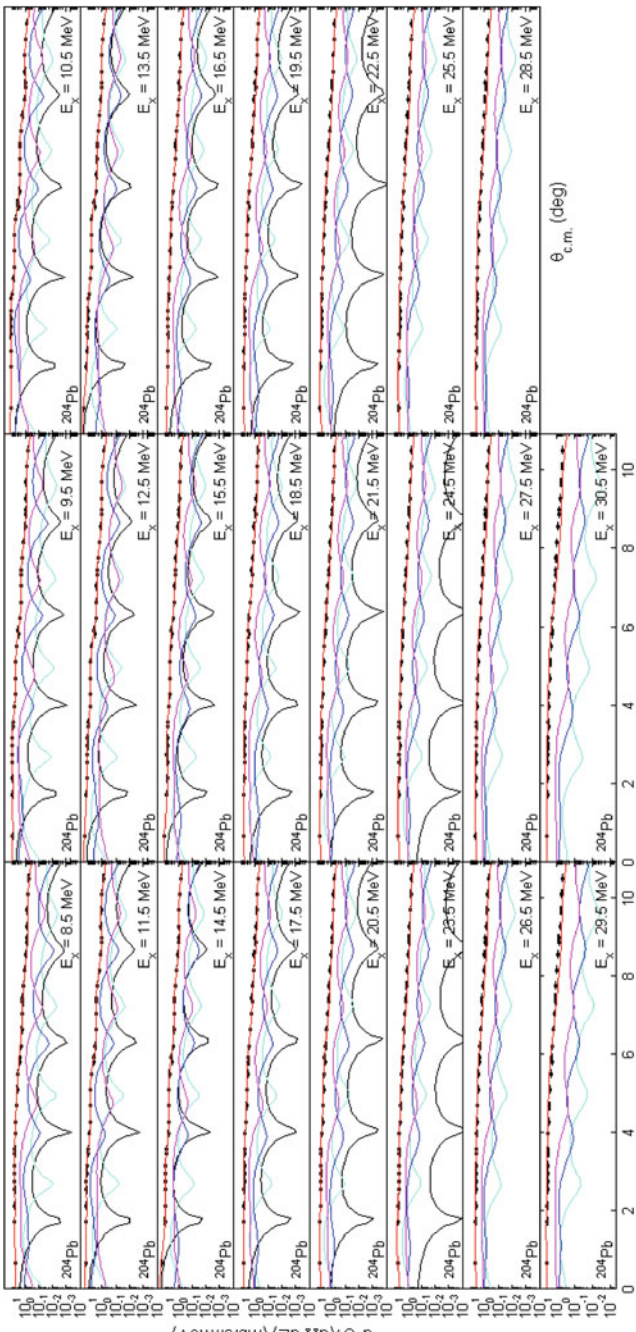

Fig. A.6 Results of MDA analysis for ^{204}Pb at E_x = 8.5 to 30.5 MeV. *Black squares* are the experimental data points. *Red line* is the fit to the data. The corresponding contributions of the first four multipole, L = 0–3 are shown. *Black line* for L = 0, *cyan line* for L = 1, *blue line* for L = 2 and *magenta line* for L = 3

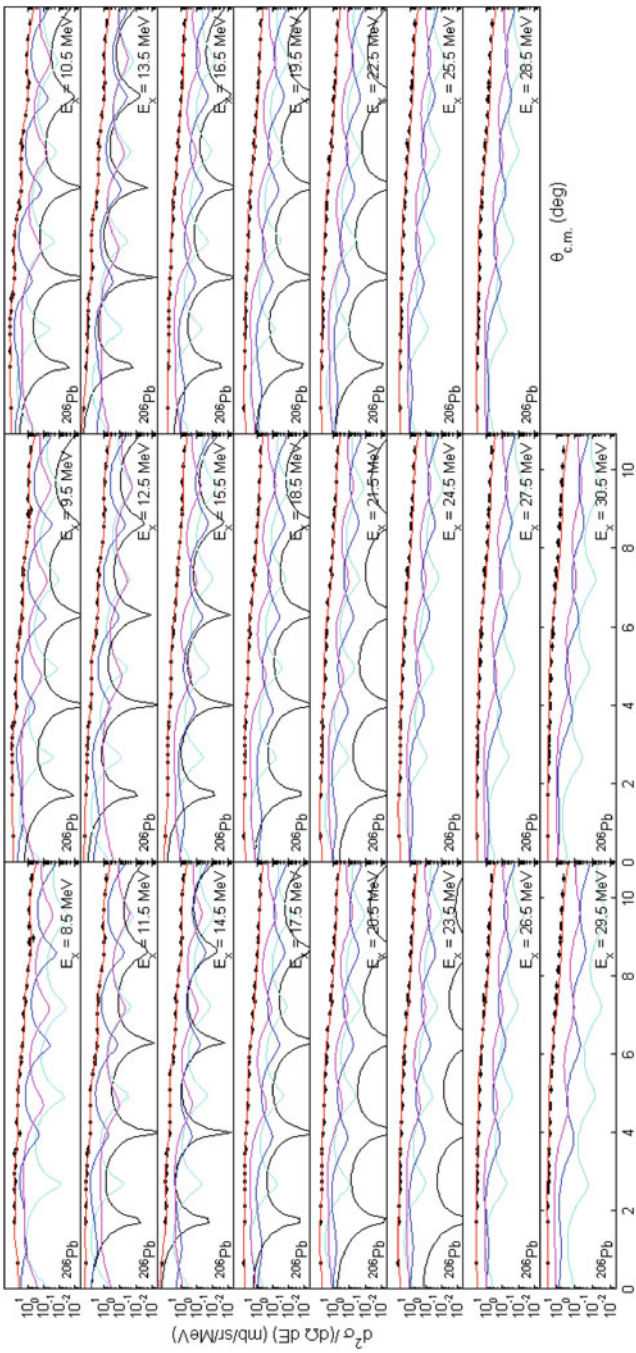

Fig. A.7 Results of MDA analysis for ^{206}Pb at E_x = 8.5 to 30.5 MeV. *Black squares* are the experimental data points. *Red line* is the fit to the data. The corresponding contributions of the first four multipoles, L = 0–3 are shown. *Black line* for L = 0, *cyan line* for L = 1, *blue line* for L = 2 and *magenta line* for L = 3

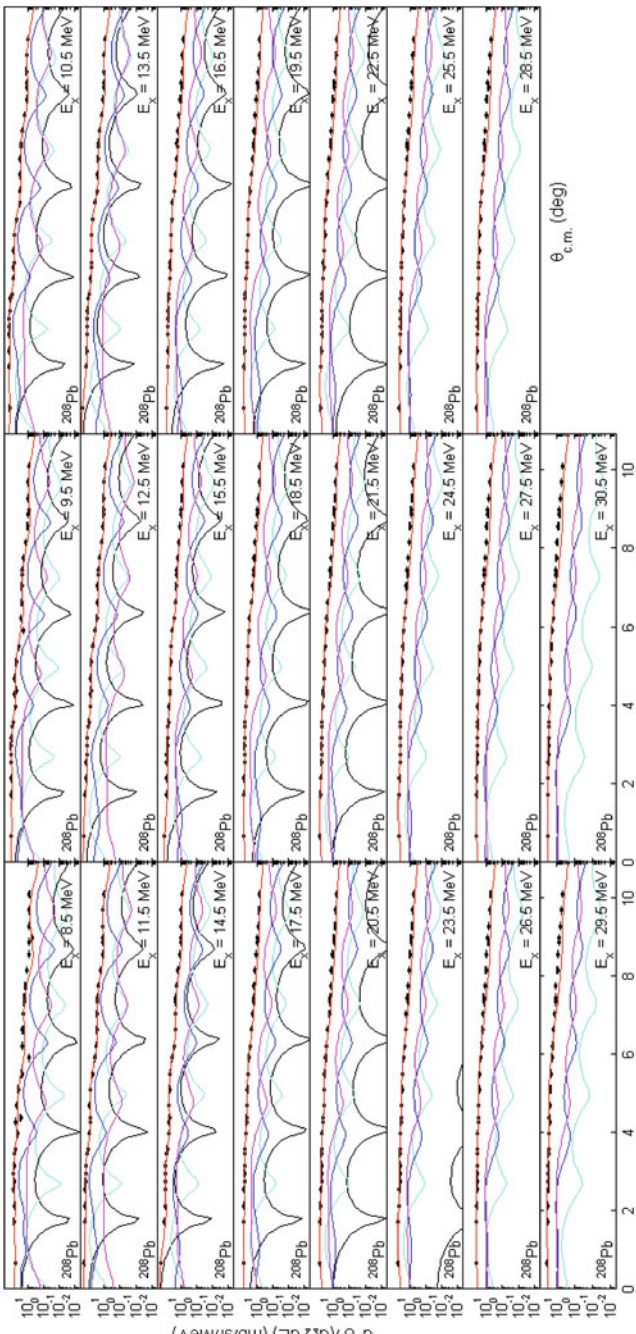

Fig. A.8 Results of MDA analysis for ^{208}Pb at E_x = 8.5 to 30.5 MeV. *Black squares* are the experimental data points. *Red line* is the fit to the data. The corresponding contributions of the first four multipoles, L = 0–3 are shown. *Black line* for L = 0, *cyan line* for L = 1, *blue line* for L = 2 and *magenta line* for L = 3

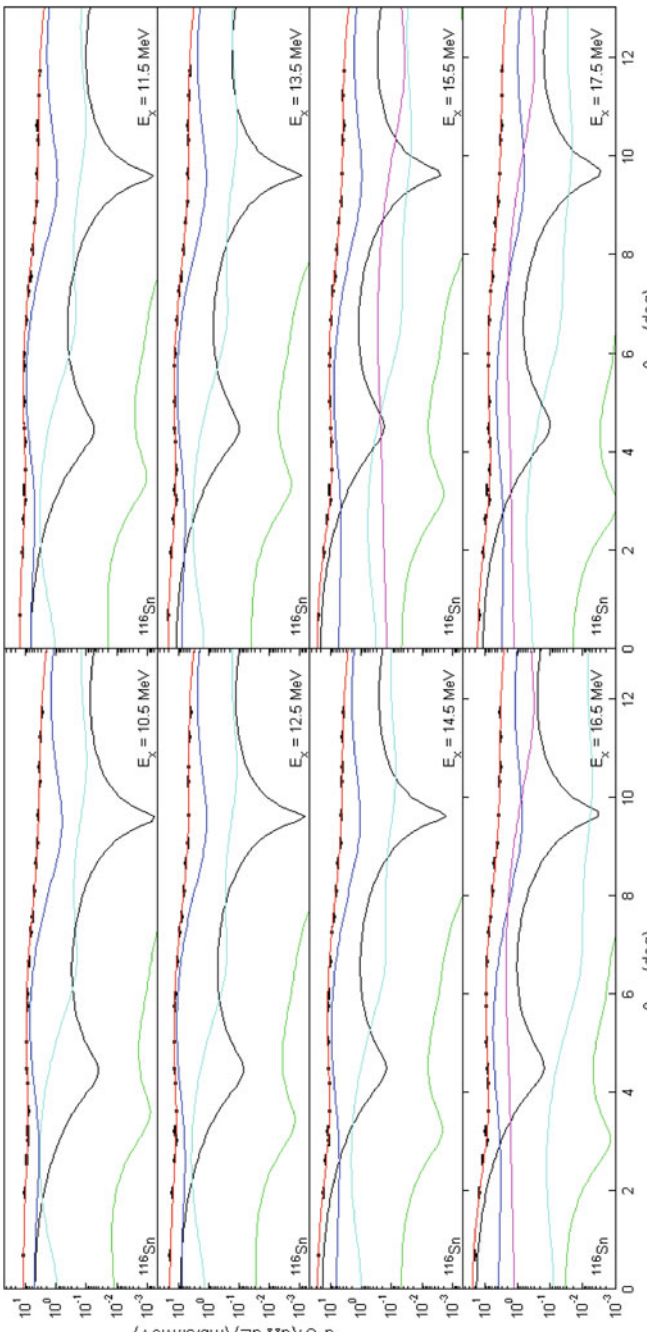

Fig. A.9 Results of MDA analysis for ^{116}Sn at E_x = 10.5 to 17.5 MeV. *Black squares* are the experimental data points. *Red line* is the fit to the data. The corresponding contributions of the first four multipoles, L = 0–3 along with IVGDR contribution are shown. *Black line* for L = 0, *cyan line* for L = 1, *blue line* for L = 2, *magenta line* for L = 3 and *green line* for IVDGR

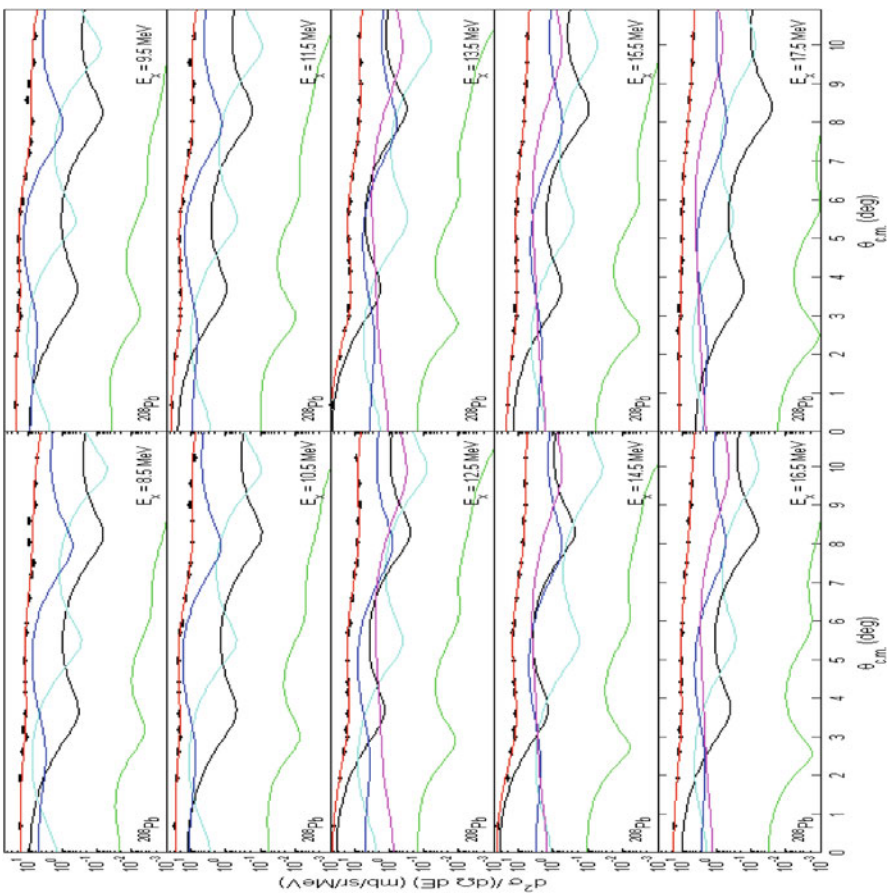

Fig. A.10 Results of MDA analysis for ^{208}Pb at E_x = 8.5 to 17.5 MeV. *Black squares* are the experimental data points. *Red line* is the fit to the data. The corresponding contributions of the first four multipoles, L = 0–3 along with IVGDR contribution are shown. *Black line* for L = 0, *cyan line* for L = 1, *blue line* for L = 2, *magenta line* for L = 3 and *green line* for IVDGR

Appendix B
Isoscalar Giant Dipole and Isoscalar Giant Quadrupole Resonances

The isoscalar giant dipole resonance (ISGDR) and the isoscalar giant quadrupole resonance (ISGQR) strength distributions were extracted as a part of the multipole decomposition analysis (MDA)for the Cd isotopes (E-309) and the Pb isotopes (E-340).

E-309: The ISGDR strength distributions are presented in Figs. B.1 and B.2. The Lorentzian fits to the data are shown by red lines and the parameters obtained from these fits are summarized in Tables B.1 and B.2. For comparison, ISGDR parameters corresponding to the low energy (LE) component and the high energy (HE) components from Lui et al. (Gaussian fits) are also provided [95].

E-340: The ISGDR and ISGQR strength distributions are presented in Fig. B.3. The Lorentzian fits to the data are shown by red lines and the parameters obtained from these fits are summarized in Tables B.3 and B.4. For comparison, ISGDR parameters corresponding to the low energy (LE) component and the high energy (HE) components from previous measurements are also provided. Parameter values marked with an asterisk (*) were extracted from the moment ratios rather than peak fitting.

D.C. Patel, *A Study of the Isoscalar Giant Monopole Resonance*, Springer Theses,
DOI 10.1007/978-3-319-22207-3

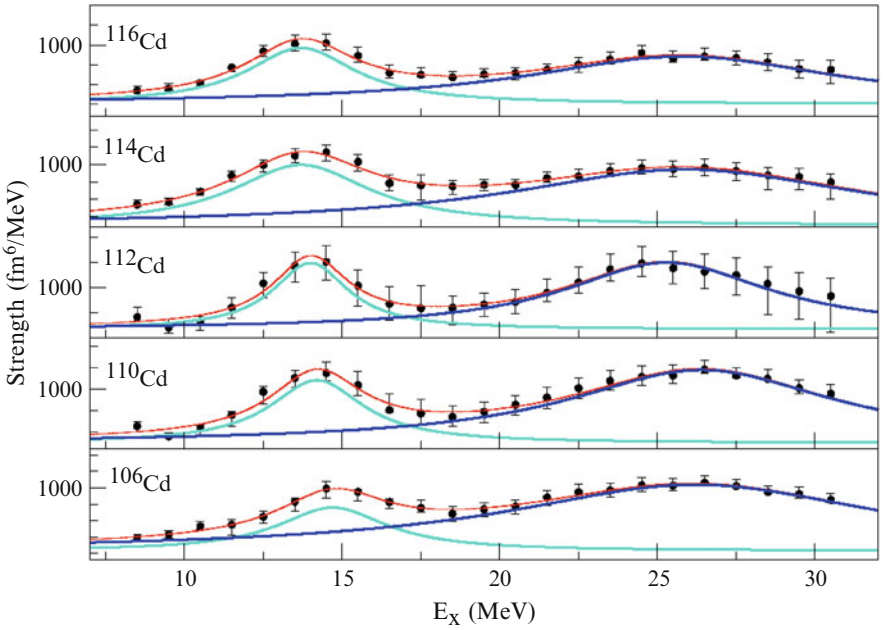

Fig. B.1 E-309: The ISGDR strength distributions in the Cd isotopes investigated in this work. The *solid red lines* represent Lorentzian fits to the data

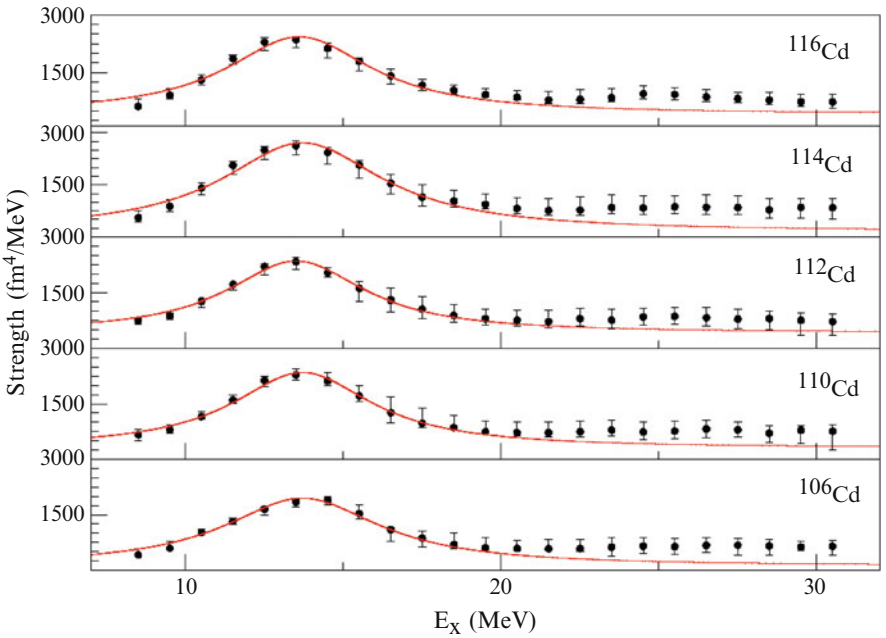

Fig. B.2 E-309: The ISGQR strength distributions in the Cd isotopes investigated in this work. The *solid red lines* represent Lorentzian fits to the data

Table B.1 Lorentzian fit parameters for the ISGDR strength distributions in the Cd isotopes investigated in this work

Target	E_{ISGDR} (MeV)		Γ (MeV)	E_{ISGDR} (MeV) Ref. [95]	FWHM (MeV) Ref. [95]
^{106}Cd	LE	14.7 ± 0.2	4.2 ± 1.2	–	–
	HE	26.2 ± 0.4	14.6 ± 1.9	–	–
^{110}Cd	LE	14.2 ± 0.2	3.6 ± 0.6	$14.47\ ^{+0.44}_{-0.47}$	$8.7\ ^{+0.87}_{-0.87}$
	HE	26.4 ± 0.3	10.3 ± 1.3	$23.30\ ^{+0.55}_{-0.48}$	$7.32\ ^{+1.07}_{-0.78}$
^{112}Cd	LE	14.0 ± 0.3	2.9 ± 1.0	–	–
	HE	25.3 ± 0.7	7.9 ± 2.4	–	–
^{114}Cd	LE	13.7 ± 0.2	5.3 ± 1.0	–	–
	HE	25.9 ± 0.7	13.6 ± 3.2	–	–
^{116}Cd	LE	13.7 ± 0.2	4.2 ± 0.7	$13.94\ ^{+0.26}_{-0.30}$	$8.31\ ^{+0.59}_{-0.46}$
	HE	25.8 ± 0.5	12.0 ± 2.2	$23.58\ ^{+0.42}_{-0.42}$	$9.22\ ^{+0.92}_{-0.72}$

Table B.2 Lorentzian fit parameters for the ISGQR strength distributions in the Cd isotopes investigated in this work

Target	E_{ISGQR} (MeV)	Γ (MeV)	E_{ISGQR} (MeV) Ref. [95]	FWHM (MeV) Ref. [95]
^{106}Cd	13.7 ± 0.3	6.0 ± 1.6	–	–
^{110}Cd	13.7 ± 0.2	5.4 ± 1.0	$13.09\ ^{+0.14}_{-0.13}$	$5.18\ ^{+0.09}_{-0.41}$
^{112}Cd	13.5 ± 0.2	5.35 ± 1.2	–	–
^{114}Cd	13.7 ± 0.3	6.2 ± 1.9	–	–
^{116}Cd	13.6 ± 0.2	5.6 ± 0.9	$13.13\ ^{+0.12}_{-0.12}$	$4.94\ ^{+0.18}_{0.16}$

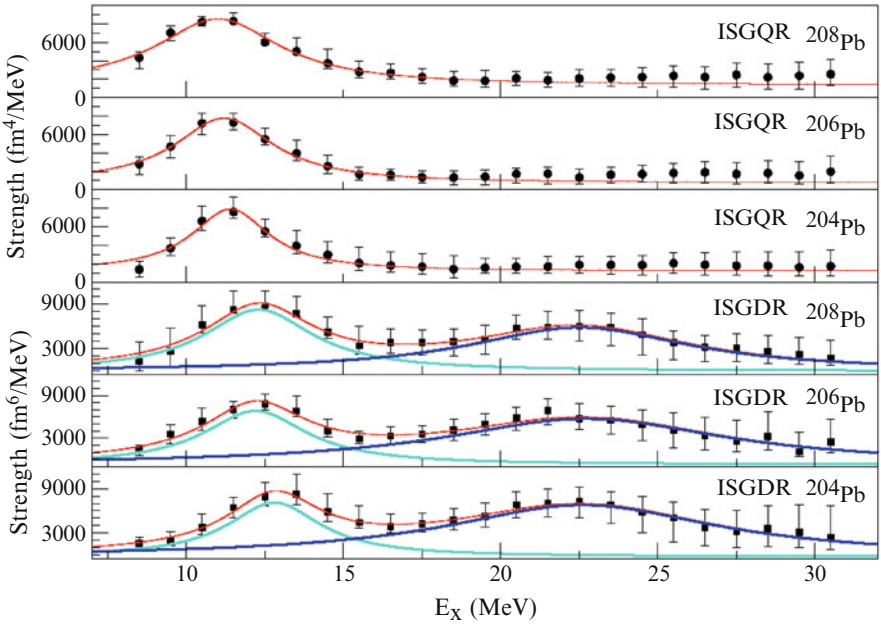

Fig. B.3 E-340: The ISGDR and the ISGQR strength distributions in the three Pb isotopes investigated in this work are shown in the *lower three panels* and the *upper three panels* respectively. The *solid red lines* represent Lorentzian fits to the data

Table B.3 Lorentzian fit parameters for the ISGDR strength distributions in the Pb isotopes investigated in this work

Target			This work	RCNP-U [53]	TAMU-Y [115]	TAMU-C [120]
^{204}Pb	LE	E (MeV)	12.8 ± 0.3	–	–	–
		Γ (MeV)	3.6 ± 1.3	–	–	–
	HE	E (MeV)	22.6 ± 0.8	–	–	–
		Γ (MeV)	10.6 ± 4.8	–	–	–
^{206}Pb	LE	E (MeV)	12.2 ± 0.3	–	–	–
		Γ (MeV)	4.0 ± 1.4	–	–	–
	HE	E (MeV)	22.7 ± 1.1	–	–	–
		Γ (MeV)	11.0 ± 5.8	–	–	–
^{208}Pb	LE	E (MeV)	12.3 ± 0.3	13.0 ± 0.1	13.26 ± 0.30	12.2 ± 0.6
		Γ (MeV)	4.2 ± 1.3	1.1 ± 0.4	5.68 ± 0.50	4.5 ± 1.2
	HE	E (MeV)	22.5 ± 0.9	22.7 ± 0.2	22.2 ± 0.30	19.9 ± 0.8
		Γ (MeV)	8.6 ± 6.8	11.9 ± 0.4	9.39 ± 0.35	5.9 ± 1.4

Table B.4 Lorentzian fit parameters for the ISGQR strength distributions for the three Pb isotopes studied as a part of this thesis work

	(MeV)	This work	Jülich [27]	TAMU* [115]	IUCF [117]	KVI [116]
^{204}Pb	E	11.4 ± 0.2	–	–	–	–
	Γ	3.0 ± 0.9	–	–	–	–
^{206}Pb	E	11.2 ± 0.2	–	–	–	11.0 ± 0.3
	Γ	3.8 ± 1.0	–	–	–	2.7 ± 0.3
^{208}Pb	E	11.0 ± 0.2	10.9 ± 0.3	10.89 ± 0.30	10.9 ± 0.3	10.9 ± 0.3
	Γ	4.8 ± 1.0	2.6 ± 0.3	3.00 ± 0.30	2.4 ± 0.4	3.0 ± 0.3

Bibliography

1. J. Speth, *Electric and Magnetic Giant Resonance in Nuclei*, vol. 7 (World Scientific, Singapore/River Edge, 1991)
2. X. Chen, Giant resonance study by 6Li scattering. Ph.D. thesis, Texas A & M University, 2008
3. E. Khan, The Giant monopole resonance in Pb isotopes. (2009), http://arxiv.org/pdf/0907.3423.pdf
4. L.-G. Cao, H. Sagawa, G. Colò, Microscopic study of the isoscalar giant monopole resonance in Cd, Sn, and Pb isotopes. Phys. Rev. C **86**(5), 054313 (2012). ISSN 0556-2813. doi:10.1103/PhysRevC.86.054313
5. H. Sagawa, S. Yoshida, G.-M. Zeng, J.-Z. Gu, X.-Z. Zhang, Isospin dependence of incompressibility in relativistic and nonrelativistic mean field calculations. Phys. Rev. C **76**(3), 034327 (2007). ISSN 0556-2813. doi:10.1103/PhysRevC.76.034327
6. D. Patel, U. Garg, M. Fujiwara, T. Adachi, H. Akimune, G.P.A. Berg, A. Okamoto, K. Sault, R. Talwar, M. Uchida, M. Yosoi, Testing the mutually enhanced magicity effect in nuclear incompressibility via the giant monopole resonance in the ^{204,206,208}Pb isotopes. Phys. Lett. B **726**, 178–181 (2013). doi: 10.1016/j.physletb.2013.08.027
7. G. Colò, U. Garg, H. Sagawa, Symmetry energy from the nuclear collective motion: constraints from dipole, quadrupole, monopole and spin-dipole resonances. Eur. Phys. J. A **50**(2), 26 (2014). ISSN 1434-6001. doi:10.1140/epja/i2014-14026-9
8. G. Colò, The compression modes in atomic nuclei and their relevance for the nuclear equation of state. Phys. Part. Nucl. **39**(2), 286–305 (2011). ISSN 1063-7796. doi:10.1134/S1063779608020056
9. J. Piekarewicz, Unmasking the nuclear matter equation of state. Phys. Rev. C **69**(4), 041301 (2004). ISSN 0556-2813. doi:10.1103/PhysRevC.69.041301
10. J.M. Lattimer, M. Prakash, Neutron star structure and the equation of state. Astrophys. J. **550**(1), 426–442 (2001). ISSN 0004-637X. doi:10.1086/319702
11. C.J. Horowitz, Neutron star structure and the neutron radius of ^{208}Pb. Phys. Rev. Lett. **86**(25), 5647–5650 (2001). ISSN 0031-9007. doi:10.1103/PhysRevLett.86.5647
12. J. Piekarewicz, M. Centelles, Incompressibility of neutron-rich matter. Phys. Rev. C **79**(5), 054311 (2009). ISSN 0556-2813. doi:10.1103/PhysRevC.79.054311
13. J. Piekarewicz, Symmetry energy constraints from giant resonances: a relativistic mean-field theory overview. Eur. Phys. J. A **50**(2), 25 (2014). ISSN 1434-6001. doi:10.1140/epja/i2014-14025-x
14. A. Bohr, B. Mottelson, *Nuclear Structure*, vol. II (Benjamin, New York, 1975)
15. N. Glendenning, Equation of state from nuclear and astrophysical evidence. Phys. Rev. C **37**(6), 2733–2743 (1988). ISSN 0556-2813. doi:10.1103/PhysRevC.37.2733

D.C. Patel, *A Study of the Isoscalar Giant Monopole Resonance*, Springer Theses,
DOI 10.1007/978-3-319-22207-3

16. M.N. Harakeh, A. van der Woude, *Giant Resonances Fundamental High-Frequency Modes of Nuclear Ecistations* (Oxford University Press, New York, 2001)
17. G. Satchler, New giant resonances in nuclei. Phys. Rep. **14**(3), 97–127 (1974). ISSN 03701573. doi:10.1016/0370-1573(74)90039-8
18. S. Stringari, Sum rules for compression modes. Phys. Lett. B **108**(4–5), 232–236 (1982). ISSN 03702693. doi:10.1016/0370-2693(82)91182-0
19. J. Treiner, H. Krivine, O. Bohigas, J. Martorell, Nuclear incompressibility: from finite nuclei to nuclear matter. Nucl. Phys. A **371**(2), 253–287 (1981). ISSN 03759474. doi:10.1016/0375-9474(81)90067-1
20. J. Blaizot, J. Berger, J. Dechargé, M. Girod, Microscopic and macroscopic determinations of nuclear compressibility. Nucl. Phys. A **591**(3), 435–457 (1995). ISSN 03759474. doi:10.1016/0375-9474(95)00294-B
21. J. Blaizot, Nuclear compressibilities. Phys. Rep. **64**(4), 171–248 (1980). ISSN 03701573. doi:10.1016/0370-1573(80)90001-0
22. J. Pearson, The incompressibility of nuclear matter and the breathing mode. Phys. Lett. B **271**(1–2), 12–16 (1991). ISSN 03702693. doi:10.1016/0370-2693(91)91269-2
23. S. Shlomo, D. Youngblood, Nuclear matter compressibility from isoscalar giant monopole resonance. Phys. Rev. C **47**(2), 529–536 (1993). ISSN 0556-2813. doi:10.1103/PhysRevC.47.529
24. T. Li, U. Garg, Y. Liu, R. Marks, B.K. Nayak, P.V. Madhusudhana Rao, M. Fujiwara, H. Hashimoto, K. Nakanishi, S. Okumura, M. Yosoi, M. Ichikawa, M. Itoh, R. Matsuo, T. Terazono, M. Uchida, Y. Iwao, T. Kawabata, T. Murakami, H. Sakaguchi, S. Terashima, Y. Yasuda, J. Zenihiro, H. Akimune, K. Kawase, M.N. Harakeh, Isoscalar giant resonances in the Sn nuclei and implications for the asymmetry term in the nuclear-matter incompressibility. Phys. Rev. C **81**(3), 034309 (2010). ISSN 0556-2813. doi:10.1103/PhysRevC.81.034309
25. J. Piekarewicz, Correlating the giant-monopole resonance to the nuclear-matter incompressibility. Phys. Rev. C **66**(3), 034305 (2002). ISSN 0556-2813. doi:10.1103/PhysRevC.66.034305
26. J. Piekarewicz, Why is the equation of state for tin so soft? Phys. Rev. C **76**(3), 031301 (2007). ISSN 0556-2813. doi:10.1103/PhysRevC.76.031301
27. H. Morsch, C. Sükösd, M. Rogge, P. Turek, H. Machner, C. Mayer-Böricke, Giant monopole and quadrupole resonances and other multipole excitations in ^{208}Pb studied in 43 MeV/nucleon α-particle and deuteron scattering. Phys. Rev. C **22**(2), 489–500 (1980). ISSN 0556-2813. doi:10.1103/PhysRevC.22.489
28. A.M. Austin, *The Two-Body Force in Nuclei* (Plenum, New York, 1972)
29. T. Li, U. Garg, Y. Liu, R. Marks, B.K. Nayak, P.V.M. Rao, M. Fujiwara, H. Hashimoto, K. Kawase, K. Nakanishi, S. Okumura, M. Yosoi, M. Itoh, M. Ichikawa, R. Matsuo, T. Terazono, M. Uchida, T. Kawabata, H. Akimune, Y. Iwao, T. Murakami, H. Sakaguchi, S. Terashima, Y. Yasuda, J. Zenihiro, M.N. Harakeh, Isotopic dependence of the giant monopole resonance in the even-A $^{112-124}$Sn isotopes and the asymmetry term in nuclear incompressibility. Phys. Rev. Lett. **99**(16), 162503 (2007). ISSN 0031-9007. doi:10.1103/PhysRevLett.99.162503
30. O. Civitarese, A. Dumrauf, M. Reboiro, P. Ring, M. Sharma, Effect of pairing on breathing mode and nuclear matter compressibility. Phys. Rev. C **43**(6), 2622–2630 (1991). ISSN 0556-2813. doi:10.1103/PhysRevC.43.2622
31. J. Li, G. Colò, J. Meng, Microscopic linear response calculations based on the Skyrme functional plus the pairing contribution. Phys. Rev. C **78**(6), 064304 (2008). ISSN 0556-2813. doi:10.1103/PhysRevC.78.064304
32. E. Khan, Role of superfluidity in nuclear incompressibilities. Phys. Rev. C **80**(1), 011307 (2009). ISSN 0556-2813. doi:10.1103/PhysRevC.80.011307
33. V. Tselyaev, J. Speth, S. Krewald, E. Litvinova, S. Kamerdzhiev, N. Lyutorovich, A. Avdeenkov, F. Grümmer, Description of the giant monopole resonance in the even-A $^{112-124}$Sn isotopes within a microscopic model including quasiparticle-phonon coupling. Phys. Rev. C **79**(3), 034309 (2009). ISSN 0556-2813. doi:10.1103/PhysRevC.79.034309

34. P. Veselý, J. Toivanen, B.G. Carlsson, J. Dobaczewski, N. Michel, A. Pastore, Giant monopole resonances and nuclear incompressibilities studied for the zero-range and separable pairing interactions. Phys. Rev. C **86**(2), 024303 (2012). ISSN 0556-2813. doi:10.1103/PhysRevC.86.024303
35. J. Piekarewicz, Do we understand the incompressibility of neutron-rich matter? J. Phys. G: Nucl. Part. Phys. **37**(6), 064038 (2010). ISSN 0954-3899. doi:10.1088/0954-3899/37/6/064038
36. E. Khan, Giant monopole resonance in Pb isotopes. Phys. Rev. C **80**(5), 057302 (2009). ISSN 0556-2813. doi:10.1103/PhysRevC.80.057302
37. H. Sagawa, I. Hamamoto, X.Z. Zhang, Giant monopole states in nuclei near drip lines. J. Phys. G: Nucl. Part. Phys. **24**(8), 1445–1454 (1998). ISSN 0954-3899. doi:10.1088/0954-3899/24/8/019
38. E. Khan, N. Paar, D. Vretenar, Low-energy monopole strength in exotic nickel isotopes. Phys. Rev. C **84**(5), 051301 (2011). ISSN 0556-2813. doi:10.1103/PhysRevC.84.051301
39. E. Khan, N. Paar, D. Vretenar, L.-G. Cao, H. Sagawa, G. Colò, Incompressibility of finite fermionic systems: stable and exotic atomic nuclei. Phys. Rev. C **87**(6), 064311 (2013). ISSN 0556-2813. doi:10.1103/PhysRevC.87.064311
40. D. Savran, T. Aumann, A. Zilges, Experimental studies of the Pygmy dipole resonance. Prog. Part. Nucl. Phys. **70**, 210–245 (2013). ISSN 01466410. doi:10.1016/j.ppnp.2013.02.003
41. C. Demonchy, W. Mittig, H. Savajols, P. Roussel-Chomaz, M. Chartier, B. Jurado, L. Giot, D. Cortina-Gil, M. Caamaño, G. Ter-Arkopian, A. Fomichev, A. Rodin, M. Golovkov, S. Stepantsov, A. Gillibert, E. Pollacco, A. Obertelli, H. Wang, MAYA, a gaseous active target. Nucl. Instrum. Methods Phys. Res. Sect. A: Accel. Spectrom. Detect. Assoc. Equip. **573**(1–2), 145–148 (2007). ISSN 01689002. doi:10.1016/j.nima.2006.11.025
42. A. Vorobyov, G. Korolev, A. Dobrovolsky, A. Khanzadeev, G. Petrov, E. Spiridenkov, Y. Terrien, J. Lugol, J. Saudinos, B. Silverman, F. Wellers, Experimental apparatus for the study of small angle neutron-proton elastic scattering at intermediate energies. Nucl. Instrum. Methods Phys. Res. Sect. A: Accel. Spectrom. Detect. Assoc. Equip. **270**(2–3), 419–430 (1988). ISSN 01689002. doi:10.1016/0168-9002(88)90710-3
43. C. Monrozeau, E. Khan, Y. Blumenfeld, W. Mittig, D. Beaumel, M. Caamaño, D. Cortina-Gil, C. Demonchy, N. Frascaria, U. Garg, M. Gelin, A. Gillibert, D. Gupta, F. Maréchal, A. Obertelli, P. Roussel-Chomaz, J.-A. Scarpaci, Measurement of the GMR in the unstable ^{56}Ni nucleus using the active target maya. Nucl. Phys. A **788**(1–4), 182–187 (2007). ISSN 03759474. doi:10.1016/j.nuclphysa.2007.01.080
44. C. Monrozeau, E. Khan, Y. Blumenfeld, C. Demonchy, W. Mittig, P. Roussel-Chomaz, D. Beaumel, M. Caamaño, D. Cortina-Gil, J. Ebran, N. Frascaria, U. Garg, M. Gelin, A. Gillibert, D. Gupta, N. Keeley, F. Maréchal, A. Obertelli, J.-A. Scarpaci, First measurement of the Giant monopole and quadrupole resonances in a short-lived nucleus: ^{56}Ni. Phys. Rev. Lett. **100**(4), 042501 (2008). ISSN 0031-9007. doi:10.1103/PhysRevLett.100.042501
45. N. Marty, Orsay Report IPNO-PhN-75-11 (1979), http://www.iaea.org/inis/collection/NCLCollectionStore/_Public/11/512/11512772.pdf
46. A. Willis, M. Morlet, N. Marty, R. Frascaria, C. Djalali, V. Comparat, P. Kitching, Excitation of the giant monopole resonance in ^{208}Pb, ^{120}Sn, ^{90}Zr, ^{58}Ni and ^{40}Ca by the scattering of 108 MeV deliterons. Nucl. Phys. A **344**(1), 137–150 (1980). ISSN 03759474. doi:10.1016/0375-9474(80)90435-2
47. G. Satchler, *Direct Nuclear Reaction* (Oxford University Press, Oxford, 1983)
48. M. Harakeh, A. Dieperink, Isoscalar dipole resonance: form factor and energy weighted sum rule. Phys. Rev. C **23**(5), 2329–2334 (1981). ISSN 0556-2813. doi:10.1103/PhysRevC.23.2329
49. G. Satchler, Isospin and macroscopic models for the excitation of giant resonances and other collective states. Nucl. Phys. A **472**(2), 215–236 (1987). ISSN 03759474. doi:10.1016/0375-9474(87)90208-9
50. M. Uchida, Thesis: isoscalar giant dipole resonance ad nuclear incompressibility, June 2003

51. T. Deal, S. Fallieros, Models and sum rules for nuclear transition densities. Phys. Rev. C **7**(4), 1709–1710 (1973). ISSN 0556-2813. doi:10.1103/PhysRevC.7.1709
52. Y.-W. Lui, D. Youngblood, H. Clark, Y. Tokimoto, B. John, Isoscalar giant resonances for nuclei with mass between 56 and 60. Phys. Rev. C **73**(1), 014314 (2006). ISSN 0556-2813. doi:10.1103/PhysRevC.73.014314
53. M. Uchida, H. Sakaguchi, M. Itoh, M. Yosoi, T. Kawabata, Y. Yasuda, H. Takeda, T. Murakami, S. Terashima, S. Kishi, U. Garg, P. Boutachkov, M. Hedden, B. Kharraja, M. Koss, B. Nayak, S. Zhu, M. Fujiwara, H. Fujimura, H. Yoshida, K. Hara, H. Akimune, M. Harakeh, Systematics of the bimodal isoscalar giant dipole resonance. Phys. Rev. C **69**(5), 051301 (2004). ISSN 0556-2813. doi:10.1103/PhysRevC.69.051301
54. G.R. Satchler, Particle. Part. Nucl. **5**, 105 (1972)
55. A.M. Bernstein, *Advances in Nuclear Physics* (Plenum Press, New York, 1969)
56. S.S. Dietrich, B.L. Berman, Atlas of photoneutron cross sections obtained with monoenergetic photons. At. Data Nucl. Data Tables **38**(2), 199–338 (1988). ISSN 0092640X. doi:10.1016/0092-640X(88)90033-2
57. B. Berman, S. Fultz, Measurements of the giant dipole resonance with monoenergetic photons. Rev. Mod. Phys. **47**(3), 713–761 (1975). ISSN 0034-6861. doi:10.1103/RevModPhys.47.713
58. K. Hatanaka, M. Fukuda, M. Kibayashi, S. Morinobu, K. Nagayama, Present status of the RCNP cyclotron facility, in *Proceedings of IPAC'10*, Kyoto (2010)
59. K. Hatanaka, K. Takahisa, H. Tamura, M. Sato, I. Miura, Performance of the RCNP polarized ion source. Nucl. Instrum. Methods Phys. Res. Sect. A: Accel. Spectrom. Detect. Assoc. Equip. **384**(2–3), 575–582 (1997). ISSN 01689002. doi:10.1016/S0168-9002(96)00941-2
60. T. Wakasa, K. Hatanaka, Y. Fujita, G. Berg, H. Fujimura, H. Fujita, M. Itoh, J. Kamiya, T. Kawabata, K. Nagayama, T. Noro, H. Sakaguchi, Y. Shimbara, H. Takeda, K. Tamura, H. Ueno, M. Uchida, M. Uraki, M. Yosoi, High resolution beam line for the Grand Raiden spectrometer. Nucl. Instrum. Methods Phys. Res. Sect. A: Accel. Spectrom. Detect. Assoc. Equip. **482**(1–2), 79–93 (2002). ISSN 01689002. doi:10.1016/S0168-9002(01)01686-2
61. M. Fujiwara, H. Akimune, I. Daito, H. Fujimura, Y. Fujita, K. Hatanaka, H. Ikegami, I. Katayama, K. Nagayama, N. Matsuoka, S. Morinobu, T. Noro, M. Yoshimura, H. Sakaguchi, Y. Sakemi, A. Tamii, M. Yosoi, Magnetic spectrometer Grand Raiden. Nucl. Instrum. Methods Phys. Res. Sect. A: Accel. Spectrom. Detect. Assoc. Equip. **422**(1–3), 484–488 (1999). ISSN 01689002. doi:10.1016/S0168-9002(98)01009-2
62. M. Itoh, H. Sakaguchi, H. Takeda, T. Taki, M. Uchida, RCNP annual report. Technical report, 1999
63. M. Itoh, Thesis: compressional-mode Giant resonance in deformed nuclei. Ph.D. thesis, Osaka University, 2003
64. T. Noro, M. Fujiwara, O. Kamigaito, S. Hirata, Y. Fujita, RCNP annual report. Technical report, 1991
65. A. Tamii, H. Sakaguchi, H. Takeda, M. Yosoi, H. Alumune, M. Fujiwara, H. Ogata, M. Tanaka, H. Togawa, New data acquisition system for the focal plane polarimeter of the Grand Raiden spectrometer. IEEE Trans. Nucl. Sci. **43**(5), 2488–2491 (1996)
66. A. Tamii, M. Itoh, T. Kawabata, H. Sakaguchi, Proceedings of the 2nd international data acquisition workshop on network data acquisition system. Technical report, 1996
67. H. Yoshida, T. Baba, T. Noro, M. Kawabata, H. Akimune, RCNP annual report. Technical report, 1996
68. T. Kawabata, H. Sakaguchi, M. Nakamura, H. Sakamoto, RCNP annual report. Technical report, 1996
69. M. Yosoi, Yosoi analyzer (2010), http://www.rcnp.osaka-u.ac.jp/~yosoi/
70. G.F. Knoll, *Radiation Detection and Measurement* (Wiley, New York, 2000)
71. G.R. Satchler, *Introduction to Nuclear Reactions*, 1st edn. (Wiley, 1980). ISBN 0-470-26467-5

72. P.E. Hodgson, *The Optical Model of Elastic Scattering* (Oxford Uniersity Press, Oxford, 1963)
73. I. Ulehla, L. Gomolcak, Z. Pluhar, *Optical Model of the Atomic Nucleus* (Academic, New York, 1964)
74. G. Satchler, D. Khoa, Missing monopole strength in ^{58}Ni and uncertainties in the analysis of α-particle scattering. Phys. Rev. C **55**(1), 285–297 (1997). ISSN 0556-2813. doi:10.1103/PhysRevC.55.285
75. M. Itoh, H. Sakaguchi, M. Uchida, T. Ishikawa, T. Kawabata, T. Murakami, H. Takeda, T. Taki, S. Terashima, N. Tsukahara, Y. Yasuda, M. Yosoi, U. Garg, M. Hedden, B. Kharraja, M. Koss, B. Nayak, S. Zhu, H. Fujimura, M. Fujiwara, K. Hara, H. Yoshida, H. Akimune, M. Harakeh, M. Volkerts, Systematic study of L = 3 giant resonances in Sm isotopes via multipole decomposition analysis. Phys. Rev. C **68**(6), 064602 (2003). ISSN 0556-2813. doi:10.1103/PhysRevC.68.064602
76. G. Fricke, C. Bernhardt, K. Heilig, L. Schaller, L. Schellenberg, E. Shera, C. Dejager, Nuclear ground state charge radii from electromagnetic interactions. At. Data Nucl. Data Tables **60**(2), 177–285 (1995). ISSN 0092640X. doi:10.1006/adnd.1995.1007
77. M. Rhoades-Brown, M. Macfarlane, S. Pieper, Techniques for heavy-ion coupled-channels calculations. I. Long-range Coulomb coupling. Phys. Rev. C **21**(6), 2417–2426 (1980). ISSN 0556-2813. doi:10.1103/PhysRevC.21.2417
78. Http://www.nndc.bnl.gov/, 2014. 'nndc.' http://www.nndc.bnl.gov/be2/
79. T. Kibédi, R. Spear, Reduced electric-octupole transition probabilities, B(E3;01+ → 31−) – an update. At. Data Nucl. Data Tables **80**(1), 35–82 (2002). ISSN 0092640X. doi:10.1006/adnd.2001.0871
80. W. Daehnick, J. Childs, Z. Vrcelj, Global optical model potential for elastic deuteron scattering from 12 to 90 MeV. Phys. Rev. C **21**(6), 2253–2274 (1980). ISSN 0556-2813. doi:10.1103/PhysRevC.21.2253
81. A. Korff, P. Haefner, C. Bäumer, A. van den Berg, N. Blasi, B. Davids, D. De Frenne, R. de Leo, D. Frekers, E.-W. Grewe, M. Harakeh, F. Hofmann, M. Hunyadi, E. Jacobs, B. Junk, A. Negret, P. von Neumann-Cosel, L. Popescu, S. Rakers, A. Richter, H. Wörtche, Deuteron elastic and inelastic scattering at intermediate energies from nuclei in the mass range 6<A<116. Phys. Rev. C **70**(6), 067601 (2004). ISSN 0556-2813. doi:10.1103/PhysRevC.70.067601
82. H. An, C. Cai, Global deuteron optical model potential for the energy range up to 183 MeV. Phys. Rev. C **73**(5), 054605 (2006). ISSN 0556-2813. doi:10.1103/PhysRevC.73.054605
83. Y. Han, Y. Shi, Q. Shen, Deuteron global optical model potential for energies up to 200 MeV. Phys. Rev. C **74**(4), 044615 (2006). ISSN 0556-2813. doi:10.1103/PhysRevC.74.044615
84. D.T. Khoa, G. Satchler, Generalized folding model for elastic and inelastic nucleus–nucleus scattering using realistic density dependent nucleon–nucleon interaction. Nucl. Phys. A **668**(1–4), 3–41 (2000). ISSN 03759474. doi:10.1016/S0375-9474(99)00680-6
85. J. Raynal, *Proceedings of the Workshop on Applied Nuclear Theory and Nuclear Model Calculations for Nuclear Technology Application*, Trieste (1988)
86. A.J. Koning, J. Delaroche, Local and global nucleon optical models from 1 keV to 200 MeV. Nucl. Phys. A **713**(3–4), 231–310 (2003). ISSN 03759474. doi:10.1016/S0375-9474(02)01321-0
87. M. Matoba, M. Hyakutake, I. Kumabe, Volume integrals of optical potentials for light composite projectiles. Phys. Rev. C **32**(5), 1773–1775 (1985). ISSN 0556-2813. doi:10.1103/PhysRevC.32.1773
88. L. Arnold, B. Clark, E. Cooper, H. Sherif, D. Hutcheon, P. Kitching, J. Cameron, R. Liljestrand, R. MacDonald, W. McDonald, C. Miller, G. Neilson, W. Olsen, D. Sheppard, G. Stinson, D. McDaniels, J. Tinsley, R. Mercer, L. Swensen, P. Schwandt, C. Stronach, Energy dependence of the p-^{40}Ca optical potential: a Dirac equation perspective. Phys. Rev. C **25**(2), 936–940 (1982). ISSN 0556-2813. doi:10.1103/PhysRevC.25.936
89. D. Youngblood, Y.-W. Lui, H. Clark, Giant resonances in ^{24}Mg. Phys. Rev. C **60**(1), 014304 (1999). ISSN 0556-2813. doi:10.1103/PhysRevC.60.014304

90. H. Clark, Y.-W. Lui, D. Youngblood, Folding model optical potential for ^{90}Zr, ^{144}Sm and ^{208}Pb (1999), http://cyclotron.tamu.edu/1999-2000/sec1/Hlc.pdf
91. J. Bojowald, H. Machner, H. Nann, W. Oelert, M. Rogge, P. Turek, Elastic deuteron scattering and optical model parameters at energies up to 100 MeV. Phys. Rev. C **38**(3), 1153–1163 (1988). ISSN 0556-2813. doi:10.1103/PhysRevC.38.1153
92. A. Betker, C. Gagliardi, D. Semon, R. Tribble, H. Xu, A. Zaruba, Deuteron elastic scattering at 110 and 120 MeV. Phys. Rev. C **48**(4), 2085–2088 (1993). ISSN 0556-2813. doi:10.1103/PhysRevC.48.2085
93. C. Bäumer, R. Bassini, A. van den Berg, D. De Frenne, D. Frekers, M. Hagemann, V. Hannen, M. Harakeh, J. Heyse, M. de Huu, E. Jacobs, M. Mielke, S. Rakers, R. Schmidt, H. Sohlbach, H. Wörtche, Deuteron elastic and inelastic scattering from ^{12}C, ^{24}Mg, and ^{58}Ni at 170 MeV. Phys. Rev. C **63**(3), 037601 (2001). ISSN 0556-2813. doi:10.1103/PhysRevC.63.037601
94. N. Van Sen, J. Arvieux, Y.E. Yanlin, G. Gaillard, Elastic scattering of polarized deuterons from ^{40}Ca and ^{58}Ni at intermediate energies. Phys. Lett. B **156**(June), 185–188 (1985)
95. Y.-W. Lui, D. Youngblood, Y. Tokimoto, H. Clark, B. John, Isoscalar multipole strength in ^{110}Cd and ^{116}Cd. Phys. Rev. C **69**(3), 034611 (2004). ISSN 0556-2813. doi:10.1103/PhysRevC.69.034611
96. M. Itoh, H. Sakaguchi, M. Uchida, T. Ishikawa, T. Kawabata, T. Murakami, H. Takeda, T. Taki, S. Terashima, N. Tsukahara, Y. Yasuda, M. Yosoi, U. Garg, M. Hedden, B. Kharraja, M. Koss, B. Nayak, S. Zhu, H. Fujimura, M. Fujiwara, K. Hara, H. Yoshida, H. Akimune, M. Harakeh, M. Volkerts, The effect of deformation in the isoscalar giant dipole resonance. Nucl. Phys. A **731**, 41–48 (2004). ISSN 03759474. doi:10.1016/j.nuclphysa.2003.11.017
97. S. Brandenburg, W. Borghols, A. Drentje, L. Ekström, M. Harakeh, A. van der Woude, A. Hå kanson, L. Nilsson, N. Olsson, M. Pignanelli, R. De Leo, Decay of the isoscalar giant monopole resonance in ^{208}Pb. Nucl. Phys. A **466**(1), 29–69 (1987). ISSN 03759474. doi:10.1016/0375-9474(87)90344-7
98. U. Garg, The isoscalar giant dipole resonance: a status report. Nucl. Phys. A **731**, 3–14 (2004). ISSN 03759474. doi:10.1016/j.nuclphysa.2003.11.013
99. M. Hunyadi, A. van den Berg, N. Blasi, C. Bäumer, M. Csatlós, L. Csige, B. Davids, U. Garg, J. Gulyás, M. Harakeh, M. de Huu, B. Junk, A. Krasznahorkay, S. Rakers, D. Sohler, H. Wörtche, Direct proton decay of the isoscalar giant dipole resonance. Phys. Lett. B **576**(3–4), 253–259 (2003). ISSN 03702693. doi:10.1016/j.physletb.2003.10.016
100. B. Nayak, U. Garg, M. Koss, T. Li, E. Martis, H. Fujimura, M. Fujiwara, K. Hara, K. Kawase, K. Nakanishi, E. Obayashi, H. Yoshida, M. Itoh, S. Kishi, H. Sakaguchi, H. Takeda, M. Uchida, Y. Yasuda, M. Yosoi, R. Zegers, H. Akimune, M. Harakeh, M. Hunyadi, Direct proton decay of the isoscalar giant dipole resonance in ^{208}Pb. Phys. Lett. B **674**(4–5), 281–285 (2009). ISSN 03702693. doi:10.1016/j.physletb.2009.03.047
101. M. Hunyadi, H. Hashimoto, T. Li, H. Akimune, H. Fujimura, M. Fujiwara, Z. Gácsi, U. Garg, K. Hara, M.N. Harakeh, J. Hoffman, M. Itoh, T. Murakami, K. Nakanishi, B.K. Nayak, S. Okumura, H. Sakaguchi, S. Terashima, M. Uchida, Y. Yasuda, M. Yosoi, Proton decay from the isoscalar giant dipole resonance in ^{58}Ni. Phys. Rev. C **80**(4), 044317 (2009). ISSN 0556-2813. doi:10.1103/PhysRevC.80.044317
102. B. John, Y. Tokimoto, Y.-W. Lui, H. Clark, X. Chen, D. Youngblood, Isoscalar electric multipole strength in ^{12}C. Phys. Rev. C **68**(1), 014305 (2003). ISSN 0556-2813. doi:10.1103/PhysRevC.68.014305
103. G.A. Lalazissis, J. König, P. Ring, New parametrization for the Lagrangian density of relativistic mean field theory. Phys. Rev. C **55**(1), 540–543 (1997). ISSN 0556-2813. doi:10.1103/PhysRevC.55.540

104. B.G. Todd-Rutel, J. Piekarewicz, Neutron-rich nuclei and neutron stars: a new accurately calibrated interaction for the study of neutron-rich matter. Phys. Rev. Lett. **95**(12), 122501 (2005). ISSN 0031-9007. doi:10.1103/PhysRevLett.95.122501
105. J. Piekarewicz, Self-consistent description of nuclear compressional modes. Phys. Rev. C **64**(2), 024307 (2001). ISSN 0556-2813. doi:10.1103/PhysRevC.64.024307
106. U. Garg, T. Li, S. Okumura, H. Akimune, M. Fujiwara, M. Harakeh, H. Hashimoto, M. Itoh, Y. Iwao, T. Kawabata, K. Kawase, Y. Liu, R. Marks, T. Murakami, K. Nakanishi, B. Nayak, P. Madhusudhana Rao, H. Sakaguchi, Y. Terashima, M. Uchida, Y. Yasuda, M. Yosoi, J. Zenihiro, The giant monopole resonance in the Sn isotopes: why is tin so "fluffy"? Nucl. Phys. A **788**(1–4), 36–43 (2007). ISSN 03759474. doi:10.1016/j.nuclphysa.2007.01.046
107. E. Khan, J. Margueron, G. Colò, K. Hagino, H. Sagawa, Effect of pairing correlations on incompressibility and symmetry energy in nuclear matter and finite nuclei. Phys. Rev. C **82**(2), 024322 (2010). ISSN 0556-2813. doi:10.1103/PhysRevC.82.024322
108. M. Centelles, X. Roca-Maza, X. Viñas, M. Warda, Nuclear symmetry energy probed by neutron skin thickness of nuclei. Phys. Rev. Lett. **102**(12), 122502 (2009). ISSN 0031-9007. doi:10.1103/PhysRevLett.102.122502
109. S. Patra, M. Centelles, X. Viñas, M. Del Estal, Surface incompressibility from semiclassical relativistic mean field calculations. Phys. Rev. C **65**(4), 044304 (2002). ISSN 0556-2813. doi:10.1103/PhysRevC.65.044304
110. L.-W. Chen, B.-J. Cai, C. Ko, B.-A. Li, C. Shen, J. Xu, Higher-order effects on the incompressibility of isospin asymmetric nuclear matter. Phys. Rev. C **80**(1), 014322 (2009). ISSN 0556-2813. doi:10.1103/PhysRevC.80.014322
111. D. Patel, U. Garg, M. Fujiwara, H. Akimune, G. Berg, M. Harakeh, M. Itoh, T. Kawabata, K. Kawase, B. Nayak, T. Ohta, H. Ouchi, J. Piekarewicz, M. Uchida, H. Yoshida, M. Yosoi, Giant monopole resonance in even-A Cd isotopes, the asymmetry term in nuclear incompressibility, and the "softness" of Sn and Cd nuclei. Phys. Lett. B **718**(2), 447–450 (2012). ISSN 03702693. doi:10.1016/j.physletb.2012.10.056
112. N. Zeldes, T. Dumitrescu, H. Köhler, Mutual support of magicities and residual effective interactions near ^{208}Pb. Nucl. Phys. A **399**(1), 11–50 (1983). ISSN 03759474. doi:10.1016/0375-9474(83)90592-4
113. D. Lunney, C. Thibault, Recent trends in the determination of nuclear masses. Rev. Mod. Phys. **75**(3), 1021–1082 (2003). ISSN 0034-6861. doi:10.1103/RevModPhys.75.1021
114. M. Uchida, H. Sakaguchi, M. Itoh, M. Yosoi, T. Kawabata, H. Takeda, Y. Yasuda, T. Murakami, T. Ishikawa, T. Taki, N. Tsukahara, S. Terashima, U. Garg, M. Hedden, B. Kharraja, M. Koss, B. Nayak, S. Zhu, M. Fujiwara, H. Fujimura, K. Hara, E. Obayashi, H. Yoshida, H. Akimune, M. Harakeh, M. Volkerts, Isoscalar giant dipole resonance in Pb via inelastic α scattering at 400 MeV and nuclear incompressibility. Phys. Lett. B **557**(1–2), 12–19 (2003). ISSN 03702693. doi:10.1016/S0370-2693(03)00137-0
115. D.H. Youngblood, Y.-W. Lui, H.L. Clark, B. John, Y. Tokimoto, X. Chen, Isoscalar E0–E3 strength in ^{116}Sn, ^{144}Sm, ^{154}Sm, and ^{208}Pb. Phys. Rev. C **69**(3), 034315 (2004). ISSN 0556-2813. doi:10.1103/PhysRevC.69.034315
116. M. Harakeh, B. Van Heyst, K. Van Der Borg, A. Van Der Woude, Isoscalar excitations in the lead region observed in inelastic α-scattering at Eα = 120 MeV. Nucl. Phys. A **327**(2), 373–396 (1979). ISSN 03759474. doi:10.1016/0375-9474(79)90265-3
117. F. Bertrand, G. Satchler, D. Horen, J. Wu, A. Bacher, G. Emery, W. Jones, D. Miller, A. van der Woude, Giant multipole resonances from inelastic scattering of 152-MeV alpha particles. Phys. Rev. C **22**(5), 1832–1847 (1980). ISSN 0556-2813. doi:10.1103/PhysRevC.22.1832
118. M. Sharma, W. Borghols, S. Brandenburg, S. Crona, A. van der Woude, M. Harakeh, Giant monopole resonance in Sn and Sm nuclei and the compressibility of nuclear matter. Phys. Rev. C **38**(6), 2562–2572 (1988). ISSN 0556-2813. doi:10.1103/PhysRevC.38.2562

119. D. Patel, U. Garg, M. Itoh, H. Akimune, G. Berg, M. Fujiwara, M. Harakeh, C. Iwamoto, T. Kawabata, K. Kawase, J. Matta, T. Murakami, A. Okamoto, T. Sako, K. Schlax, F. Takahashi, M. White, M. Yosoi, Excitation of giant monopole resonance in ^{208}Pb and ^{116}Sn using inelastic deuteron scattering. Phys. Lett. B **735**, 387–390 (2014). ISSN 03702693. doi:10.1016/j.physletb.2014.06.073
120. H. Clark, Y.-W. Lui, D. Youngblood, Isoscalar giant dipole resonance in ^{90}Zr, ^{116}Sn, and ^{208}Pb. Phys. Rev. C **63**(3), 031301 (2001). ISSN 0556-2813. doi:10.1103/PhysRevC.63.031301